Dynamic Characterization of Galfenol (Fe$_{81.6}$Ga$_{18.4}$)

Justin J. Scheidler
The Ohio State University, Columbus, Ohio

Vivake M. Asnani
Glenn Research Center, Cleveland, Ohio

Marcelo J. Dapino
The Ohio State University, Columbus, Ohio

NASA STI Program . . . in Profile

Since its founding, NASA has been dedicated to the advancement of aeronautics and space science. The NASA Scientific and Technical Information (STI) Program plays a key part in helping NASA maintain this important role.

The NASA STI Program operates under the auspices of the Agency Chief Information Officer. It collects, organizes, provides for archiving, and disseminates NASA's STI. The NASA STI Program provides access to the NASA Technical Report Server—Registered (NTRS Reg) and NASA Technical Report Server—Public (NTRS) thus providing one of the largest collections of aeronautical and space science STI in the world. Results are published in both non-NASA channels and by NASA in the NASA STI Report Series, which includes the following report types:

- TECHNICAL PUBLICATION. Reports of completed research or a major significant phase of research that present the results of NASA programs and include extensive data or theoretical analysis. Includes compilations of significant scientific and technical data and information deemed to be of continuing reference value. NASA counter-part of peer-reviewed formal professional papers, but has less stringent limitations on manuscript length and extent of graphic presentations.

- TECHNICAL MEMORANDUM. Scientific and technical findings that are preliminary or of specialized interest, e.g., "quick-release" reports, working papers, and bibliographies that contain minimal annotation. Does not contain extensive analysis.

- CONTRACTOR REPORT. Scientific and technical findings by NASA-sponsored contractors and grantees.

- CONFERENCE PUBLICATION. Collected papers from scientific and technical conferences, symposia, seminars, or other meetings sponsored or co-sponsored by NASA.

- SPECIAL PUBLICATION. Scientific, technical, or historical information from NASA programs, projects, and missions, often concerned with subjects having substantial public interest.

- TECHNICAL TRANSLATION. English-language translations of foreign scientific and technical material pertinent to NASA's mission.

For more information about the NASA STI program, see the following:

- Access the NASA STI program home page at http://www.sti.nasa.gov

- E-mail your question to help@sti.nasa.gov

- Fax your question to the NASA STI Information Desk at 757-864-6500

- Telephone the NASA STI Information Desk at 757-864-9658

- Write to:
  NASA STI Program
  Mail Stop 148
  NASA Langley Research Center
  Hampton, VA 23681-2199

Dynamic Characterization of Galfenol (Fe$_{81.6}$Ga$_{18.4}$)

Justin J. Scheidler
The Ohio State University, Columbus, Ohio

Vivake M. Asnani
Glenn Research Center, Cleveland, Ohio

Marcelo J. Dapino
The Ohio State University, Columbus, Ohio

National Aeronautics and
Space Administration

Glenn Research Center
Cleveland, Ohio 44135

June 2016

Acknowledgments

Level of Review: This material has been technically reviewed by a committee of peers.

Available from

Contents

Dynamic Characterization of Galfenol (Fe$_{81.6}$Ga$_{18.4}$)

Justin J. Scheidler[*]
The Ohio State University
Columbus, Ohio 43210

Vivake M. Asnani
National Aeronautics and Space Administration
Glenn Research Center
Cleveland, Ohio 44135

Marcelo J. Dapino
The Ohio State University
Columbus, Ohio 43210

Summary

Galfenol has the potential to transform the smart materials industry by allowing for the development of multifunctional, load-bearing devices. One of the primary technical challenges faced by this development is the very limited experimental data on Galfenol's frequency-dependent response to dynamic stress, which is critically important for the design of such devices. This report details a novel and precise characterization of the constitutive behavior of polycrystalline Galfenol (Fe$_{81.6}$Ga$_{18.4}$) under quasi-static (1 Hz) and dynamic (4 to 1000 Hz) stress loadings. Mechanical loads are applied using a high-frequency load frame. Quasi-static minor and major hysteresis loop measurements of magnetic flux density and strain are presented for constant electromagnet currents (0 to 1.1 A) and constant magnetic fields 0 to 14 kA/m (0 to 180 Oe). The dynamic stress amplitude for minor and major loops is 2.88 and 31.4 MPa (418 and 4550 psi), respectively. Quasi-static material properties closely match published values for similar Galfenol materials. Quasi-static actuation responses are also measured and compared to quasi-static sensing responses; the high degree of reversibility seen in the comparison is consistent with published measurements and modeling results. Dynamic major and minor loops are measured for dynamic stresses up to 31 MPa (4496 psi) and 1 kHz, and the bias condition resulting in maximum, quasi-static sensitivity. Eddy current effects are quantified by considering solid and laminated Galfenol rods. Three key sources of error in the dynamic measurements are accounted for: (1) electromagnetic noise in strain signals due to Galfenol's magnetic response, (2) error in load signals due to the inertial force of fixturing, and (3) phase misalignment between signals due to conditioning electronics. For dynamic characterization, strain error is kept below 1.2 percent of full scale by wiring two collocated gauges in series (noise cancellation) and through leadwire weaving. Inertial force error is kept below 0.41 percent by measuring the dynamic force in the specimen using a nearly collocated piezoelectric load washer. The phase response of all conditioning electronics is explicitly measured and corrected for. In general, as frequency is increased, the sensing response becomes more linear because of an increase in eddy currents. As frequency increases above ~100 Hz, the elbow in the strain-versus-stress response disappears as the active (soft) regime stiffens toward the passive (hard) regime. Under constant-field conditions, the loss factors of the solid rod peak between 200 and 600 Hz, rather than exhibiting a monotonic increase. Compared to the solid rod, the laminated rod exhibits much slower increases in hysteresis with frequency, and its quasi-static behavior extends to higher frequencies. The elastic modulus of the laminated rod decreases between 100 and 300 Hz; this trend is currently unexplained.

1.0   Introduction

Magnetostrictive materials, such as Galfenol (Fe$_{1-x}$Ga$_x$, $0.13 \leq x \leq 0.29$) and Terfenol-D (Tb$_x$Dy$_{1-x}$Fe$_y$, $x \approx 0.3$, $y \approx 2$), can transduce energy between magnetic and mechanical domains. Application of magnetic fields results in mechanical deformation, which is known as magnetostriction. Conversely, the application of mechanical stress is accompanied by changes in the material's magnetization. These effects enable actuation and sensing, respectively. Secondary effects are also exhibited, including an effective reduction in elastic moduli due to stress-dependent magnetoelastic strain. Magnetostrictive transducers offer noncontact operation, high bandwidth (~10 kHz), and active properties that do not degrade with cycling (Refs. 1 and 2).

Galfenol is a particularly useful type of magnetostrictive material, because it has high tensile strength (~500 MPa, or ~72.5 ksi), very low magnetomechanical hysteresis, high magnetic permeability, and fairly constant active properties in the temperature range –20 to 80 °C (–4 to 176 °F) (Ref. 3).

---

[*]Currently with the NASA Glenn Research Center.

Through its unique combination of active properties and mechanical strength, Galfenol has the potential to transform the smart materials industry by allowing for the development of active load-bearing devices such as sensors, energy harvesters, vibration dampers, and variable stiffness components. One of the primary technical challenges needed to be addressed for this to happen is the very limited experimental data on Galfenol's frequency-dependent response to dynamic stress, which is critically important for the design of such devices. Galfenol's magnetic response to small amplitude dynamic stress (up to 2.8 MPa (406 psi), 1 kHz and 6.5 MPa (943 psi), 10 Hz) was reported in References 4 and 5, respectively; however, the phase response of the measurement systems was neglected, which significantly increases the uncertainty in hysteresis measurements. No other measurements have been published.

This report provides a complete record of a precise characterization of Galfenol's ($Fe_{81.6}Ga_{18.4}$) magnetic and mechanical responses to dynamic compressive stresses up to 31 MPa (4496 psi) and 1 kHz. The objective is to measure the one-dimensional (1D), dynamic sensing response of the material and to quantify from the response, the frequency dependence of the material properties governing 1D sensing. This is accomplished by controlling the axial, dynamic stress, and static magnetic field over a specific region of a Galfenol rod and measuring the axial strain and magnetic flux density. Auxiliary variables—drive voltage, drive current, and temperature—are also measured for reference. At each forcing frequency, sensing-based material properties are calculated using a frequency-domain method adapted from an ASTM (ASTM International) standard. Solid and laminated Galfenol rods are considered. To verify the experimental setup with existing data and to evaluate the frequency-independent

the frequency-independent performance, quasi-static actuation and sensing responses are also measured. First, the design of the experiment is discussed in detail. This is presented in the following sections: 2.0 Specimen Design, 3.0 Sensor Selection and Uncertainty Analysis, 4.0 Calibration Methods, 5.0 Experimental Setup and Methods, and 6.0 Data Processing Methods. Afterward, the testing procedures are explained. Finally, the complete data set is provided, along with a discussion of the observed trends.

The symbols used in this report are listed in Appendix A to aid the reader.

2.0 Specimen Design

A cylindrical specimen was selected for testing because it was the standard geometry manufactured by the material supplier, and it allowed for the use of an existing magnetic transducer (magnetic circuit). The magnetic circuit generated uniform magnetic fields only over a central region of the rod, which is referred to as the "gauge region." Thus, state variables were controlled and measurements were taken within the gauge region.

2.1 Recommendations From ASTM Standards

To assist with specimen design, particularly with tolerancing, relevant ASTM standards were reviewed, and specimen specifications were recorded. A full list of the relevant ASTM standards is given in References 6 to 16. Table I summarizes geometric specifications taken from standards for magnetic testing, compression testing, and dynamic testing. Additionally, specimens should be free from residual stresses (Ref. 8). The

TABLE I.—SUMMARY OF GEOMETRIC SPECIFICATIONS FOR SPECIMENS FROM RELEVANT ASTM STANDARDS

Parameter	Specification	ASTM Standard
Length (L)	≥5 in. (13 cm)	A 314/A314M (Ref. 16)
Diameter (D)	≥0.5 in. (1.3 cm)	A 314/A314M (Ref. 16)
L/D ratio	about 8 to 10 (for modulus of elasticity testing)	E9 (Ref. 10)
Diameter tolerance	±0.001 in. (25 μm)	E209 (Ref. 9)
	≤1 percent or 0.002 in. (51 μm), whichever is less	E9 (Ref. 10)
	±0.1 percent	E1875, E1876 (Refs. 13 and 14)
	±0.010 in. (0.25 mm)	A 314/A314M (Ref. 16)
	±0.005 in. (0.13 mm)	D5992 (Ref. 7)
Surface roughness	Ground smooth to ≤100 μin. (2.5 μm), root-mean-square	A 314/A314M (Ref. 16)
	Machined smooth to ≤63 μin. (1.6 μm), average	E9, E209 (Refs. 10 and 9)
Parallelism of ends	≤0.0005 in./in.	E9 (Ref. 10)
	≤0.00025 in. (6.4 μm)	E209 (Ref. 9)
	≤0.1 percent	E1875, E1876 (Refs. 13 and 14)
Flatness of ends	≤0.0005 in./in.	E9 (Ref. 10)
Perpendicularity of ends relative to sides	≤0.05°	E9 (Ref. 10)
	≤0.25°	E209 (Ref. 9)

most stringent of the tolerancing specifications in Table I were supplied to the specimen's manufacturer, ETREMA Products, Inc., who attempted to meet these very tight tolerances. This table is presented to allow the tolerances of the manufactured specimens (given in Sec. 2.4) to be benchmarked against those of an ideal specimen.

To accurately control the magnetic state of the specimen over a gauge region, a magnetic circuit was used to generate magnetic flux and guide it uniformly into the specimen. When standard magnetic circuits are used for magnetic testing, the length and diameter specifications from ASTM A 314/A314M (Ref. 16) help to ensure magnetic uniformity in the specimen. In this experiment, both magnetic and mechanical excitations were needed. Thus, a custom magnetic circuit (Figure 1 and Figure 2) was used. As suggested in ASTM A 314/A314M, this circuit's flux return path was composed of silicon iron laminations 0.46 mm (0.018 in.) thick that were bolted together and operated up to a flux density (~0.6 T, or ~6 kG) for which their magnetic permeability was below its maximum value. To minimize eddy currents in the flux return path, laminations were separated by an electrically insulating Kapton film ~0.025 mm (0.001 in.) thick. The circuit was symmetric and contained two electromagnets, which were nominally identical, to improve the uniformity of the magnetic state in the specimen. This magnetic circuit was successfully used in previous work by the authors (Refs. 18 and 19). The use of this circuit constrained the diameter of the specimen to 6.4 mm (0.25 in.) and its minimum length to 76 mm (3 in.) (to allow for the specimen ends to be mechanically engaged); therefore, the length-to-diameter ratio specification suggested by ASTM E9 (Ref. 10) was adhered to instead of the length and diameter specifications.
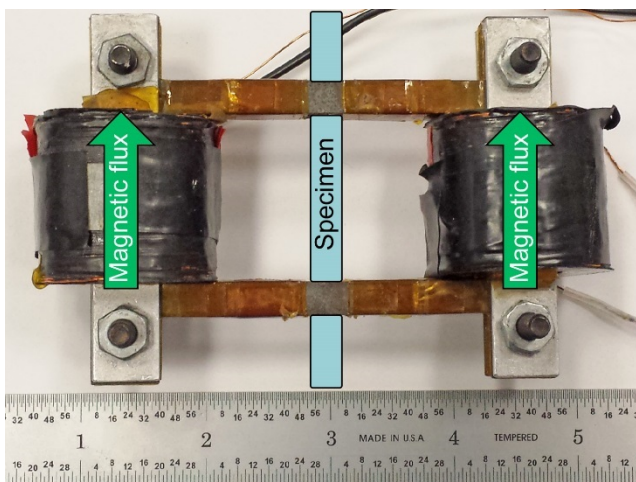
Figure 1.—Magnetic circuit used to generate uniform magnetic state in gauge region of Galfenol specimen, while allowing for independent mechanical excitation.
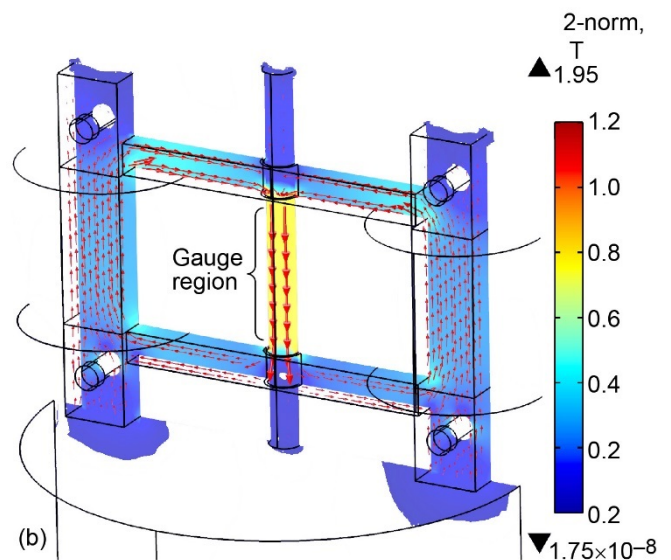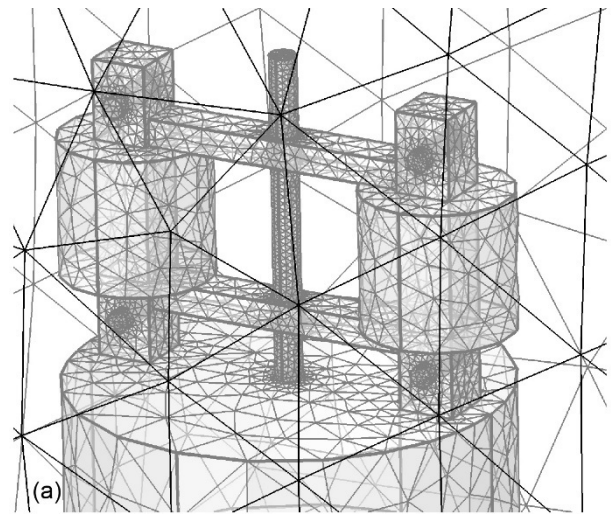
Figure 2.—COMSOL Multiphysics (Ref. 17) simulation of the three-dimensional magnetic response of magnetic circuit. (a) Meshed circuit, magnetic base/platen, and large air volume. (b) Magnetic flux density vector (arrow length proportional to magnitude) and slice plot of its 2-norm (in units of Tesla) in response to 1-A electromagnet current. Relative magnetic permeability of platen and Galfenol are 100, each coil is composed of 300 turns of 26 American wire gage (AWG) wire, and air gap between Galfenol specimen and silicon iron was included. Note uniformity and axial orientation of magnetic flux within gauge region of specimen.

2.2   Buckling

Buckling of specimens subjected to quasi-static, compressive, axial loads occurs when the specimen's first circular natural frequency of transverse bending becomes 0. The critical buckling stress T_{crit} and load P_{crit} at which this occurs is given by ASTM E9 (Ref. 10)

$$T_{crit} = \frac{P_{crit}}{A} = C_{e\text{-}f} \frac{\pi^2 EI}{L^2 A} \qquad (1)$$

where E is Young's modulus, I denotes the area moment of inertia about the centroid of the cross section, L is the specimen's length, A denotes the specimen's cross-sectional area, and $C_{e\text{-}f}$ is the end-fixity coefficient, which takes a value of 3.75 for the reported experiment (compression testing of flat-end specimens between flat, rigid anvils). Comparing Equation (1) with Table I reveals a tradeoff between a short sample (large critical buckling stress) and long sample (L/D ratio ideal for the measurement of elastic moduli). Considering this tradeoff and the constraints imposed by the magnetic circuit, a specimen length of 76 mm (3 in.) was used.

If the loading is dynamic and perfectly compressive, buckling should not occur unless the compressive load exceeds the quasi-static buckling load. However, pure compression cannot be realized, and some amount of transverse excitation will always occur. Consequently, for dynamic compression, the excitation frequency should be well below the first natural frequency of transverse vibration of the specimen. To approximate this natural frequency of the cylindrical specimen, the transverse vibration of beams subjected to axial loads was considered. The nth mode shape or eigenfunction (w_n) is provided by (Ref. 20):

$$w_n(x) = Z_1 \left[\cosh(\gamma_1 x) + Z_2 \sinh(\gamma_1 x) + Z_3 \cos(\gamma_2 x) + Z_4 \sin(\gamma_2 x) \right] \qquad (2)$$

where

$$\gamma_1^2, \gamma_2^2 = \frac{P}{2EI} \pm \left[\left(\frac{P}{2EI} \right)^2 + \frac{\rho A \omega_n^2}{EI} \right]^{1/2} \qquad (3)$$

x is the location along the beam's length, P is the applied axial force, ρ denotes the density, ω_n are the circular natural frequencies of transverse vibration (eigenvalues) of the beam, and Z_i are constants that depend on the boundary conditions. Application of fixed-fixed boundary conditions to Equation (2) gives the frequency equation

$$2\gamma_1 \gamma_2 \left[1 - \cos(\gamma_2 L) \cosh(\gamma_1 L) \right] + \sin(\gamma_2 L) \sinh(\gamma_1 L)(\gamma_1^2 - \gamma_2^2) = 0 \qquad (4)$$

An analytical expression for ω_n from Equations (3) and (4) could not be found. Thus, a numerical solution for ω_1 as a function of P was calculated. For comparison, an assumed relation between ω_1 and P was developed based on the analytical relation for a pinned-pinned beam (Ref. 20),

$$\omega_n = \frac{\pi^2}{L^2} \left(\frac{EI}{\rho A} \right)^{1/2} \left(n^4 - n^2 \frac{P}{P_{crit}} \right)^{1/2} \qquad (5)$$

and the known bounds of the curve: Equation (1) and the first transverse bending natural frequency of a fixed-fixed beam for zero axial stress (Ref. 20),

$$\omega_1 = (\beta L)_1^2 \left(\frac{EI}{\rho A L^4} \right)^{1/2}, \quad (\beta L)_1 = 4.730041 \qquad (6)$$

The assumed relation has the form

$$\omega_1 = \left(Y - J \frac{P}{P_{crit}} \right)^{1/2} \qquad (7)$$

where application of the bounds gives

$$Y = J = (\beta L)_1^4 \left(\frac{EI}{\rho A L^4} \right) \qquad (8)$$

To accurately compare the numerical and assumed relations, an end-fixity coefficient of 4 (perfectly fixed-fixed boundary conditions) was temporarily used to derive the assumed relation. The comparison in Figure 3(a) shows a near perfect agreement; thus, the assumed relation with realistic boundary conditions (end-fixity coefficient of 3.75) could be used to analyze the Galfenol specimen. The assumed relation for the Galfenol specimen is plotted in Figure 3(b) for the minimum and maximum values of Galfenol's Young's modulus. At the maximum applied compressive stress of 60 MPa (8702 psi), the specimen's first transverse bending natural frequency will approximately fall in the range 1950 to 2900 Hz. The maximum excitation frequency in this experiment (1000 Hz) was well outside this range, which suggested that buckling should not occur. Further, Galfenol exhibits low to moderate damping (Ref. 21). Consequently, any magnitude or phase distortion introduced in the results due to bending should be minimal. However, it is acknowledged that resonant frequencies are system-level properties that depend on the effective mass loading during experimentation. A larger mass would result in greater reductions in the resonant frequencies.
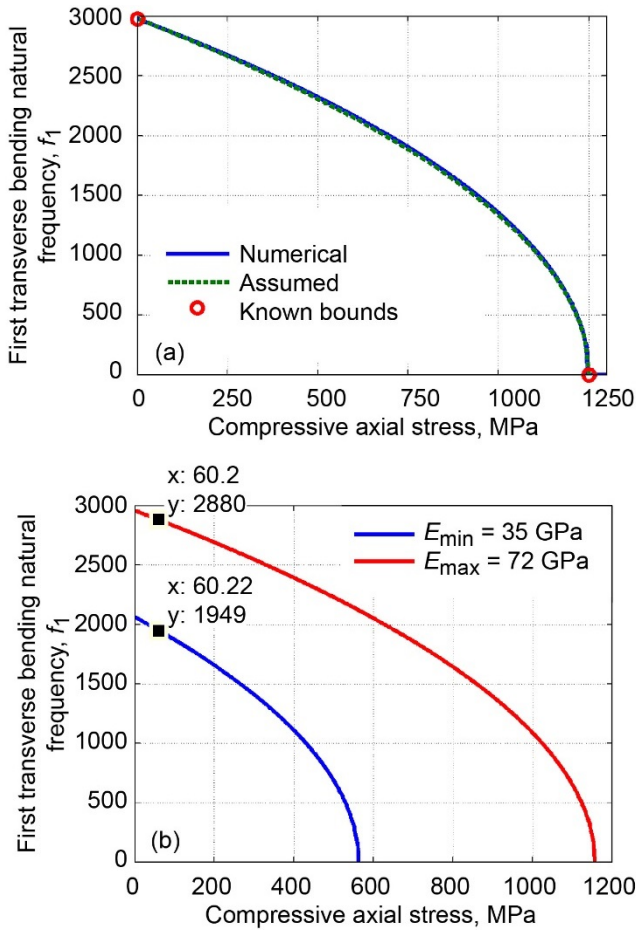
Figure 3.—Relations between first transverse bending natural frequency f_1 ($f_1 = \omega_1/2\pi$, where ω_1 is first circular natural frequency of transverse vibration) and compressive stress for Galfenol specimen. (a) Comparison of numerical and assumed relations, for perfectly fixed-fixed boundary conditions (end-fixity coefficient of 4). (b) Assumed relation, for realistic boundary conditions (end-fixity coefficient of 3.75) and Galfenol's minimum (E_{min}) and maximum (E_{max}) Young's modulus values.

2.3 Lamination

The goal of the material characterization was to measure Galfenol's response to dynamic, axial stresses and constant magnetic fields (applied at the surface). In magnetostrictive rods, dynamic axial stresses produce a time-varying, axial magnetic flux in the material. According to the Faraday-Lenz law, this time-varying magnetic flux induces electric fields that circulate around the rod's axis. Because of the material's finite resistivity, these electric fields drive circulating currents, which generate a time-varying, axial magnetic field that is superposed on the constant applied magnetic field (Figure 4(a)). Consequently, the magnetic field is non-uniform along the radial direction of the rod (Figure 4(b)), which prevents a well-defined and accurate characterization. This effect has been
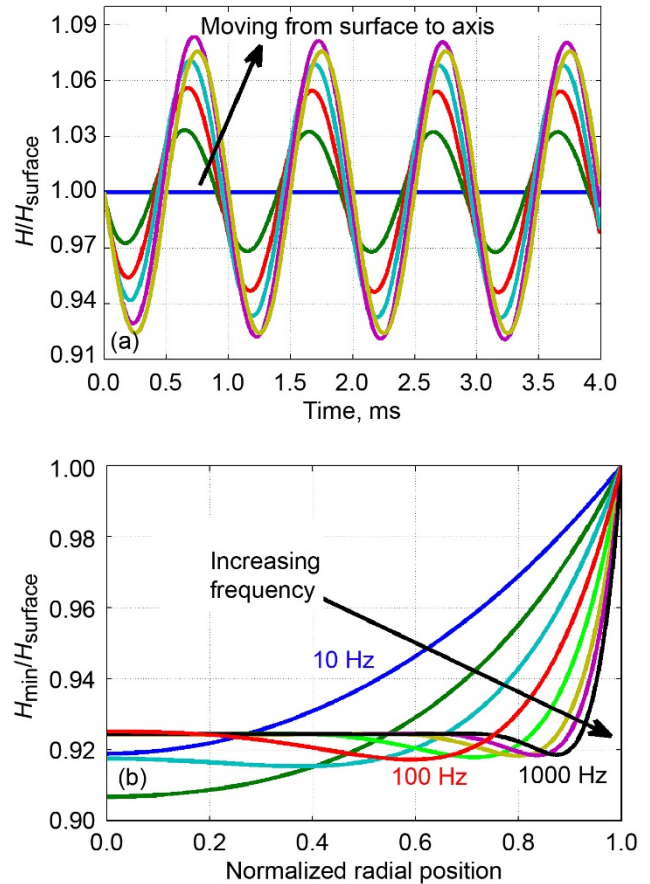

Figure 4.—Mechanically induced magnetic diffusion for Galfenol specimen. (a) Temporal response of magnetic field H normalized by surface magnetic field $H_{surface}$ at different locations along radial direction for 1000-Hz stress. (b) Normalized minimum magnetic field H_{min} as function of radial position (normalized by radius) for different stress frequencies.

termed "mechanically induced magnetic diffusion" by the authors. Simplifying the problem by assuming constant Galfenol properties (valid in the "burst" region) allows for an analytical solution (Ref. 22) for this effect in solid rods (Figure 4). Model parameters are given in Table II. In Figure 4(b), the minimum magnetic field is used to show a time-independent profile of the largest deviation of the internal field from the surface value at each point along the rod's radius.

TABLE II.—MODEL PARAMETERS USED FOR SOLUTION OF THE MECHANICALLY INDUCED MAGNETIC DIFFUSION PROBLEM

|	
Electrical conductivity, S/m	5.96×10^6
Relative magnetic permeability	350
Piezomagnetic coefficient, T/Pa	40×10^{-9}
Radius, mm (in.)	6.35 (0.25)
Bias magnetic field, kA/m (Oe)	6 (75.4)
Stress amplitude, MPa (psi)	5 (725)
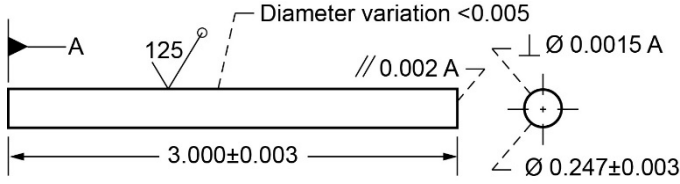
Figure 5.—Dimensions and tolerances of highly textured, <100> oriented, polycrystalline Galfenol ($Fe_{81.6}Ga_{18.4}$) rods purchased from Etrema Products, Inc. All specifications have units of inches, except for surface roughness, which is specified in units of microinches.

The analytical solution shows that the magnitude of the time-varying magnetic field increases toward the rod's axis and that the effect is more significant as the stress frequency increases. The conventional method for mitigating the effects of magnetic-field-induced magnetic diffusion is to laminate the material, whereby the material is cut into thin laminates then bonded back together with an electrically insulating adhesive. This constrains eddy currents to circulate within each laminate—a condition for which the analytical solution is invalid. In determining a laminate thickness, there is a tradeoff between minimizing eddy currents (thin laminates) and practical manufacturing limitations (thicker laminates). Thinner laminates also reduce the volume fraction of Galfenol for a given rod diameter. A laminate thickness of 0.84 mm (0.033 in.) (26 percent of the radius) was chosen to balance this tradeoff, with more weight placed on reducing eddy currents.

2.4 Specimen Geometry

The purchased alloy was <100> oriented, polycrystalline $Fe_{81.6}Ga_{18.4}$. Although the specimen was polycrystalline, the manufacturer's expertise allowed them to produce highly textured polycrystals (misorientation angle of grains was very small), whose performance can approach that of single-crystalline material. Solid and laminated rods were cut from the same bulk rod, which was grown using the free-standing zone melt method at about 25 mm/h (0.98 in./h), a rate used to produce research-grade material. Specimens cut from the same bulk rod can still be expected to have some variation in their properties. The geometry of all specimens is depicted in Figure 5, where the tolerances reflect the capabilities of the material supplier. The most stringent ASTM-recommended tolerance for surface finish, diameter variation, and parallelism could not be met. A tolerance for flatness of the rod's ends was not specified, because the supplier does not measure flatness. The laminated rod had 0.84-mm- (0.033-in.-) thick laminates.

3.0 Sensor Selection and Uncertainty Analysis

When possible, the uncertainty of each calculated quantity U_Q was quantified by the standard formula for the propagation of error given by Reference 23,

$$U_Q = \pm \left[\sum_{g=1}^{N} \left(\frac{\partial Q}{\partial z_g} U_{z_g} \right)^2 \right]^{1/2} \tag{9}$$

where U_{z_g} is the uncertainty in the measured variable z_g and N denotes the number of variables on which the result Q depends. Equation (9) is valid when individual uncertainties U_{z_g} are small. Individual uncertainties were calculated as

$$U_{z_g} = \left(U_{0_g}^2 + U_{C_g}^2 \right)^{1/2} \tag{10}$$

where U_{0_g} is the interpolation error,

$$U_{0_g} = \pm \frac{1}{2} (\text{resolution}) \tag{11}$$

and U_{C_g} is the instrument error, which is a combination of K elemental errors e_{k_g} (e.g., sensitivity and linearity errors):

$$U_{C_g} = \pm \left[\sum_{k=1}^{K} \left(e_{k_g}^2 \right) \right]^{1/2} \tag{12}$$

3.1 Distance and Area

Area was measured to calculate the axial stress in the rod. Table III summarizes the recommended accuracy of distance measurements from ASTM and Japanese Industrial Standard (JIS) standards. As recommended by ASTM E9, distances were measured using micrometers (Ref. 10). The micrometers had 0.025-mm (0.001-in.) gradations and 0.0025-mm (0.0001-in.) accuracy (interpolation and instrument uncertainties of ±0.013 and ±0.0025 mm (±0.0005 and ±0.0001 in.), respectively). For the 6.4-mm- (0.25-in.-) diameter specimen, these resulted in diameter and area uncertainties of 0.013 mm (±5.1×10⁻⁴ in., or 0.2 percent) and ±0.13 mm² (±2.0×10⁻⁴ in², or 0.4 percent), respectively.

TABLE III.—ASTM AND JIS[a] RECOMMENDATIONS FOR DISTANCE MEASUREMENTS

Parameter	Measurement accuracy	Standard
Diameter	0.025 mm (0.001 in.) dimensions >2.5 mm (0.1 in.), use average	ASTM E9, E209, E466 (Refs. 10, 9, 15)
	≤0.1 percent at three locations, use average	ASTM E1875, E1876 (Refs. 13, 14)
	≤0.5 percent at two orthogonal locations, use average	JIS Z 2273 (Ref. 24)
Area	≤1 percent	ASTM E111 (Ref. 8)

[a]Japanese Industrial Standard.

TABLE IV.—ASTM RECOMMENDATIONS FOR FORCE SENSORS

Force	Measurement accuracy	ASTM Standard
Static	±1 percent error, ≤1 percent repeatability	E4 (Ref. 6)
Dynamic	±1 percent error	E467 (Ref. 12)

TABLE V.—UNCERTAINTIES OF THE FORCE SENSORS

Force	Device	Interpolation uncertainty, U_0, N (lbf)	Instrument uncertainty, U_c, N (lbf)	Sensor uncertainty, U_z, N (lbf)
Static	Interface 1010ACK–500–B[a]	≈0	±1.3 (0.29)	±1.3 (0.29)
Dynamic	Kistler 9001A[b]	±0.005 (0.001)	±23 (5.1)	±23 (5.1)

[a]Assuming isothermal conditions and neglecting load eccentricity and creep.
[b]Assuming isothermal conditions and optimal installation.

3.2 Force and Stress

The force applied to the ends of the specimen was measured to calculate the axial stress in the rod according to Equation (14). Applied forces were in the range –1.96 to 0 kN (–441 to 0 lbf), where a negative force indicates compression. For quasi-static and dynamic experiments, small-amplitude (89 N, 20 lbf) and large-amplitude (980 N, 220 lbf) forces were applied to the specimen. Table IV summarizes the recommended accuracy of force measurements from ASTM standards. Quasi-static forces were measured using an Interface 1010ACK–500–B fatigue-rated load cell (2224 N (500 lbf) range) and an MTS Systems Corporation 493.21 signal conditioner. This load cell is very stiff and accurate, and is rated for 10^8 fully reversed loading cycles.

As discussed in Section 5.2, dynamic forces vibrate the specimen and fixtures, resulting in inertial forces that cause error in measurements of the force applied to the specimen. This error was reduced by minimizing the mass of fixturing located between the specimen and force sensor. The large masses of the platen and magnetic circuit prevented the accurate measurement of dynamic forces by the load cell. Inertial force errors below 0.41 percent were possible by using a piezoelectric load washer. The load washer could be located almost directly below the specimen, such that the inertial forces of the platen and magnetic circuit did not influence the measurement. Specifically, dynamic forces (>100 Hz) were measured using a Kistler 9001A piezoelectric load washer (7.5 kN, or 1686 lbf, range) and Kistler 5010 charge amplifier. This frequency cutoff

was selected, because the load washer's phase response is nonlinear below this cutoff (see Sec. 6.2).

The load cell was used for force control of the dynamic load frame. To compensate for inertial force errors during dynamic testing, the force command signal was increased until the load washer readout indicated the desired dynamic force amplitude.

Table V gives the uncertainty for the load cell and load washer. The uncertainties of the MTS conditioner were not specified. However, as detailed in Section 4.2, the entire static force measurement system was calibrated to the accuracy specified in ASTM E4 (≤±1 percent of the reading) (Ref. 6). The uncertainty in the calculation of dynamic force was determined from the load washer's uncertainty (Eq. (9)), the charge amplifier's sensitivity ($Sens_{\text{charge amp}}$ in volts per picocoulomb) and uncertainty (±0.5 percent), and the expression for the dynamic force F_{dynamic},

$$F_{\text{dynamic}} = p\big(q_{\text{load washer}}\big)\big(Sens_{\text{charge amp}}\big) \qquad (13)$$

where $q_{\text{load washer}}$ is the charge generated by the load washer in picocoulombs and p is the range setting in newtons per volts. The uncertainty in the static and dynamic stress measurements was estimated using the force uncertainties, Equation (9), and the equation for axial stress,

$$\sigma = \frac{F}{A} \qquad (14)$$

TABLE VI.—ASTM AND ISO[a] RECOMMENDATIONS FOR TEMPERATURE
SENSORS AND CONSTANT TEMPERATURE TESTING

Parameter	Specification	Standard
Temperature	±1 °C (±1.8 °F)	ISO 4664–1 (Ref. 25)
Allowable temperature variation during constant temperature testing	±5.5 °C (±9.9 °F)	ASTM E1875 (Ref. 13)
	±3 °C (±5.4 °F)	ASTM E209 (Ref. 9)

[a]International Organization for Standardization.

The force and stress uncertainties are plotted as a function of the measured force in Figure 6.

3.3 Temperature

The temperature of the specimen was monitored to prevent excessive temperature variation during repeated testing. If the temperature increase from room temperature exceeded 7 °C (45 °F), tests were paused and the specimen was allowed to return to room temperature. Table VI outlines the recommended uncertainty of temperature measurements and the allowable temperature variation. Temperature was measured using a Type K thermocouple and an Omega DRG–SC–TC signal conditioner, which has an uncertainty of ±2 °C (±3.6 °F). The Omega conditioner also has a very low bandwidth (~4 Hz). However, for the specified purpose, this bandwidth and uncertainty was sufficient, although the uncertainty did not meet the recommendations shown in Table VI.

3.4 Displacement and Strain

A strain (or displacement) sensor was intended to measure (or calculate) the average axial surface strain in the gauge region of the rod. Galfenol's elastic modulus is a function of magnetic field and stress. The magnetic circuit only controlled the magnetic state over a gauge region (Figure 2). Consequently, the elastic modulus varied along the specimen's length; thus, displacement or strain measurements had to be confined to the gauge region. This precluded the use of many sensors, including capacitive displacement probes, laser displacement sensors, and potentiometers. Extensometers and strain gauges were suitable. However, laser extensometers have an insufficient resolution, and extensometers have a lower bandwidth relative to strain gauges and add an eccentric mass to the specimen. Semiconductor and piezoelectric strain gauges have multiple advantages, but could not conform to the small curvature of the specimen. Therefore, metal foil strain gauges were selected. Recommended specifications of strain sensors from ASTM and International Organization for Standardization (ISO) standards are summarized in Table VII.

Selection of a metal foil strain gauge was guided by the discussions in (Ref. 27). Constantan sensing alloy was chosen for its minimal magnetic effects. A long, but narrow gauge pattern was selected to average the strain over multiple material grains, allow for easy alignment, and reduce the magnitude of
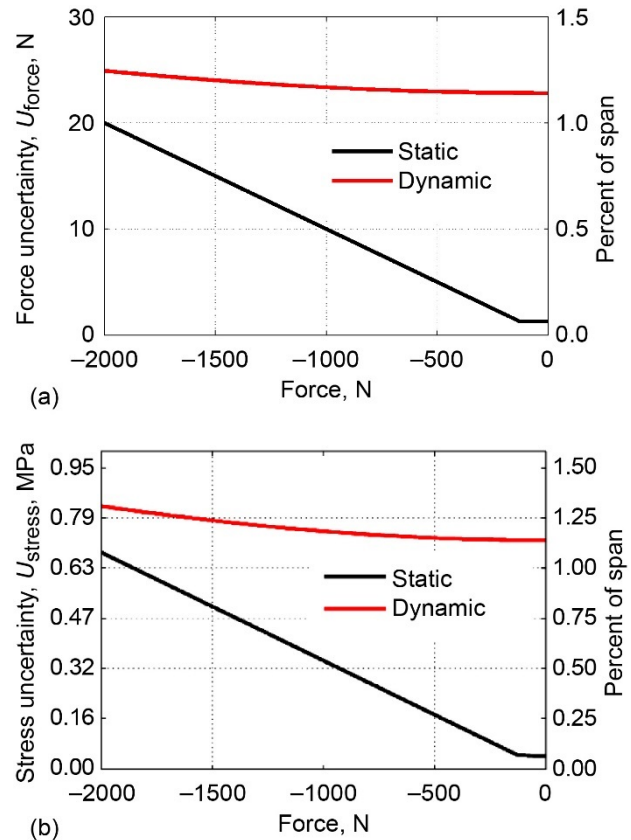

Figure 6.—Uncertainty in force and stress calculations as function of measured force. Force and stress spans (maximum value minus minimum value), 2000 N and 63 MPa, respectively, are the same for static and dynamic measurements. (a) Force uncertainty, U_{force}. (b) Stress uncertainty, U_{stress}.

electromagnetic noise. A self-temperature-compensation number of 6 (i.e., 6 ppm/°F correction) provided compensation for the thermal expansion of Galfenol, which is ~6.4 ppm/°F (Ref. 28). The largest available gauge resistance was selected to reduce leadwire effects and heat generation, which allowed for larger excitation voltages and thus a larger signal-to-noise ratio (Refs. 27 and 29). Considering these factors and availability, the Vishay Micro-Measurements EA–06–250BF–350/L strain gauges were selected. Vishay's magnetic field strain gauge (H06A–AC1–125–700) could not be used because of its 17-week lead time. However, electromagnetic noise was quantified and minimized as detailed in Section 5.4.

TABLE VII.—ASTM AND ISO[a] RECOMMENDATIONS FOR STRAIN SENSORS

Parameter	Measurement accuracy	Standard
Strain	± 1 percent	ISO 4664–1 (Ref. 25)
	± 0.1 percent to ± 1 percent	ASTM E9, E83 (Refs. 10 and 26)
Strain gauge resistance	± 0.1 percent, repeatability ≤ 0.04 percent	ASTM E251 (Ref. 11)
Strain resolution	≤ 0.05 to 0.5 percent	ASTM E9, E83 (Refs. 10 and 26)

[a]International Organization for Standardization.

To minimize the electromagnetic noise, axial strain was measured using two identical strain gauges (resistance $R_G = 350\ \Omega$ and gauge factor $f_G = 2.155$) wired in series and located on opposite sides of the rod. These gauges together formed the active arm of a Wheatstone quarter-bridge circuit. It can be shown that this circuit can be analyzed as a quarter bridge containing a single effective strain gauge having a resistance of $R_{Wh1} = 2R_G$ and gauge factor of f_G. This analogy holds if the strain gauges are identical and experience the same axial strain, but opposite bending strain. The uncorrected strain S' for this circuit was calculated as

$$S' = \left(\frac{4}{f_G}\right)\frac{V_0}{V_{ex}} \qquad (15)$$

where V_{ex} is the excitation voltage and V_0 is the bridge output voltage relative to the zero strain state. The uncorrected strain can be corrected for the quarter bridge nonlinearity and the resistance imbalance δR between the active bridge arm R_{Wh1} and its adjacent arm R_{Wh2} using

$$S'' = \frac{S'\left(2 + \dfrac{\delta R}{R_{Wh2}}\right)^2}{4\left[\left(1 + \dfrac{\delta R}{R_{Wh2}}\right) - \dfrac{f_G S'}{4}\left(2 + \dfrac{\delta R}{R_{Wh2}}\right)\left(1 + \dfrac{\delta R}{R_{Wh2}}\right)\right]} \qquad (16)$$

The effect of leadwire resistance on the bridge nonlinearity can be neglected, because the leadwire resistance was only 0.07 percent of the gauge resistance (Ref. 30). A correction for the strain output due to thermal effects can then be applied as follows (Ref. 31):

$$S''' = \left[S'' - (S_{\Theta/0} + \Delta S_{\Theta/0})\frac{2}{f_G}\right]\frac{1}{1 + \dfrac{\Delta f_G}{100}\Delta\Theta_{room}} \qquad (17)$$

where Δf_G is the variation in gauge factor with temperature (specified as a percentage per 100 °C by the manufacturer), $\Delta\Theta_{room}$ is the difference between the testing temperature and room temperature (75 °F, or 24 °C), $S_{\Theta/0}$ is the thermal output of the gauge relative to the thermal output at the temperature for

TABLE VIII.—UNCERTAINTY OF MEASURED VARIABLES USED TO CALCULATE STRAIN UNCERTAINTY

Variable	Uncertainty
Resistance imbalance, δR	$U_{\delta R} = \pm 0.11\ \Omega$[a]
Adjacent arm resistance, R_{Wh2}	$U_{R_{Wh2}} = \pm 0.08\ \Omega$[a]
Bridge output voltage, ΔV_0	$U_{\Delta V_0} = \pm 1.06\times10^{-5}$ V[b]
Excitation voltage, V_{ex},	$U_{V_{ex}} = \pm 0.0034$ V[b]
Radius of curvature, r	$U_r = \pm 6.5\times10^{-6}$ m[c] ($\pm 2.6\times10^{-4}$ in.)
Gauge factor, f_G	$U_{f_G} = \pm 0.5$ percent[d]
Gauge factor temperature variation, Δf_G	$U_{\Delta f_G} = \pm 0.2$ percent[d]
Temperature, Θ	$U_\Theta = \pm 2$ °C[e] (± 3.6 °F)
Temperature difference, $\Delta\Theta$	$U_{\Delta\Theta} = \pm 2.8$ °C[e] (± 5 °F)
Specimen coefficient of thermal expansion, α_S	$U_{\alpha_S} = \pm 0.4\times10^{-6}$ 1/°C[f] ($\pm 0.22\times10^{-6}$ 1/°F)

[a]From multimeter data sheet (Agilent 34410A) and Equations (10) to (12).
[b]From strain conditioner data sheet (Vishay 2310) and Equations (10) to (12).
[c]From Section 3.1 and Equation (9).
[d]From manufacturer.
[e]From Section 3.3.
[f]From (Ref. 28).

which the strain indicator is zeroed, and $\Delta S_{\Theta/0}$ is a correction to the thermal output due to the surface curvature of the installation location (Ref. 32),

$$\Delta S_{\Theta/0} = \frac{1}{r}\Big[\left(1 + 2v_{ad-bk}\right)\left(h_{ad}\alpha_{ad} + h_{bk}\alpha_{bk}\right)\Delta\Theta_{ref} \\ - 2v_{ad-bk}\alpha_S\left(h_{ad} + h_{bk}\right)\Big]\Delta\Theta_{ref} \qquad (18)$$

where r is the radius of curvature; α_S, α_{ad}, and α_{bk} are the coefficient of thermal expansion of the specimen, adhesive, and backing, respectively; h_{ad} and h_{bk} are the thickness of the adhesive and backing, respectively; v_{ad-bk} is the average Poisson's ratio of the adhesive and backing; and $\Delta\Theta_{ref}$ is the difference between the testing temperature and the temperature at which the strain indicator is zeroed. The uncertainty of the measured variables is summarized in Table VIII. The uncertainty in the corrected strains S'' and S''' was calculated using Equation (9) and is shown in Figure 7 as a function of the
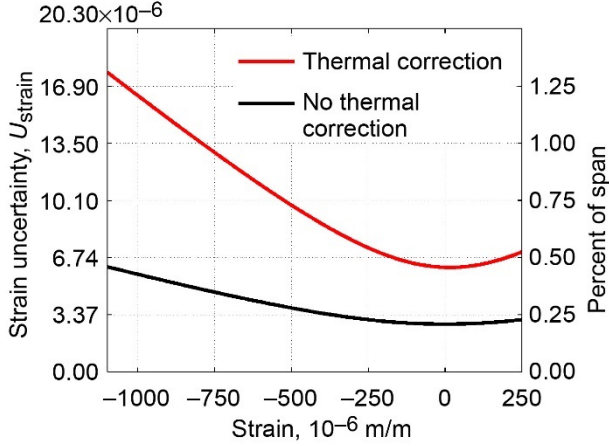
Figure 7.—Uncertainty in strain calculation.
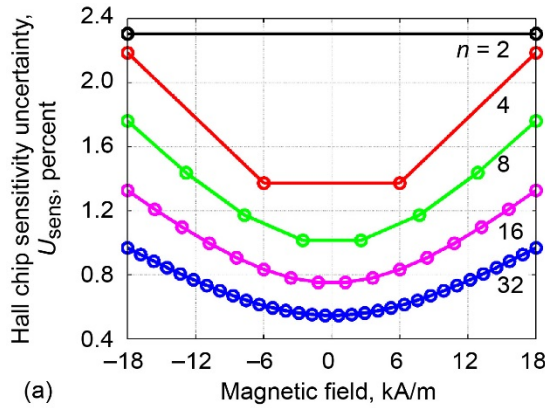
(a)
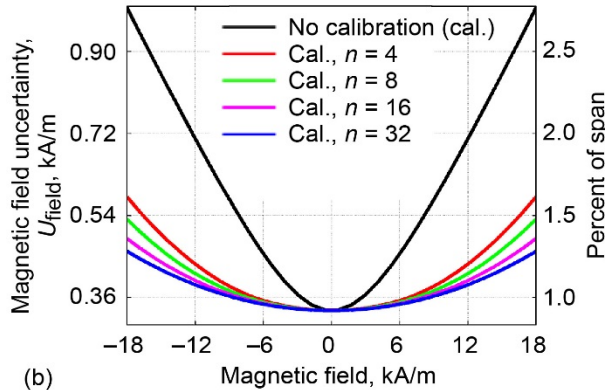
(b)

Figure 8.—Magnetic field uncertainty. (a) Uncertainty in Hall chip's sensitivity U_{sens} with n-point calibrations (see App. B for calculation of sensitivity uncertainty). (b) Uncertainty in calculated magnetic field U_{field} after n-point calibrations of sensitivity.

strain level. The required partial derivatives were determined using the commercial symbolic software Maplesoft (Ref. 33).

During repeated testing, temperature increases above the 25 °C (77 °F) ambient were typically 3 to 4 °C (5 to 7 °F), and

no more than 7 °C (13 °F). Using Equations (17) and (18) and specifications for the strain gauge, these 4 and 7 °C changes caused a thermal strain output of 7.31×10^{-6} and 10.4×10^{-6} m/m (0.54 and 0.77 percent of the span), respectively. The thermal strain can be corrected for, but at the expense of an appreciable increase in uncertainty. Since the strain uncertainty is exacerbated in the calculation of elastic properties, the thermal strain was not corrected for in the reported data.

3.5 Magnetic Field

A magnetic field sensor was needed to measure the axial, surface magnetic field in the gauge region of the rod. The applied magnetic field was in the range –18 to 18 kA/m (–226 to 226 Oe). The recommended accuracy of magnetic field sensors is ±1 percent (Ref. 16). Magnetic fields can be measured with H coils, Flip H coils, Rogowski–Chattock coils, giant magnetoresistive (GMR) sensors, and Hall effect sensors. These coils can only estimate the field at the surface of the specimen based on multiple measurements away from the surface. GMR sensors have an insufficient range (≤8 kA/m, or 101 Oe) and about 5 percent uncertainty. Hall probes provide the best accuracy, but must be located using a fixture and have a sensing region about 1.5 to 4 mm (0.059 to 0.160 in.) from their tip. Hall chips are less accurate than Hall probes, but can be directly mounted to the specimen's surface, and have a sensing region only 0.3 to 1.5 mm (0.012 to 0.059 in.) from their surface. Consequently, an Allegro A1321LUA Hall chip was selected, which could measure ±35 kA/m (±440 Oe) over the temperature range –40 to 150 °C (–40 to 302 °F).

The selected Hall chip has an interpolation uncertainty of 0.0208 V and an instrument uncertainty of

$$U_{C_{Hall}} = \pm 9.425 \left(10^{-4}\right) H \quad \text{V} \tag{19}$$

where the magnetic field (H, kA/m) assumes isothermal conditions and a constant supply voltage. The uncertainty in the magnetic field was calculated using these uncertainties, Equations (9) and (10), the Hall chip's sensitivity ($Sens_{Hall}$, V-m/kA) and uncertainty (±5 percent), and the expression for the magnetic field,

$$H = \frac{V_{Hall}}{Sens_{Hall}} \tag{20}$$

The primary source of uncertainty in the calculated field was the uncertainty in the sensitivity of the Hall chip (see App. B). Through calibration (see Sec. 4.6), the uncertainty in the sensitivity could be reduced below ±1 percent (Figure 8(a)). The magnetic field uncertainty with and without an n-point calibration is shown in Figure 8(b).
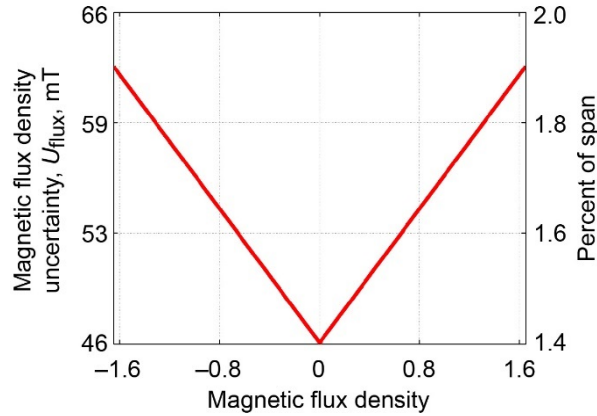
Figure 9.—Uncertainty in magnetic flux density, U_{flux}.
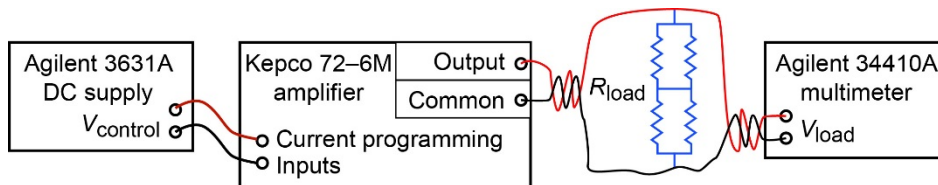
Figure 10.—Experimental setup for calibration of linear power amplifier, where $V_{control}$ is static control voltage, R_{load} is load resistance, and V_{load} is voltage across resistive load.

3.6   Magnetic Flux Density

The intent of this sensor was to measure the average magnetic flux density within the gauge region of the rod. The range of magnetic flux density was –1.65 to 1.65 T (–16.5 to 16.5 kG). For magnetic flux density measurements, it is recommended that (1) sensors have ≤1 percent of span accuracy, (2) sensing (pickup) coil voltage integrators have drift adjust circuitry with drift 1 µWb·turns/min (≤100 Mx·turns/min), and (3) the cross-sectional area enclosed by the pickup coil and its number of turns be known to ≤0.5 percent accuracy (Ref. 16). As detailed in Section 3.1, the uncertainty in the area was 0.4 percent.

Integration of the pickup coil voltage is the preferred method of measuring magnetic flux (over ballistic galvanometers and moving coil fluxmeters) because of the integrator's superior accuracy, stability, and ease of operation (Ref. 16). Consequently, a Lake Shore Model 480 integrating fluxmeter was used with a custom pickup coil. The integrator drift of this fluxmeter is 1 µWb·turns/min (≤100 Mx·turns/min), and its accuracy is ±1 percent of the reading +0.33 percent of the range). Using a calibrated pickup coil (see Sec. 4.7), the uncertainty in the magnetic flux density was measured and is shown in Figure 9. Due to the sensitivity of the pickup coil and the magnitude of the signal, the signal was only about 15 percent of the optimal fluxmeter range; thus, the range-dependent uncertainty was about 1.4 percent of the signal's span.

4.0   Calibration Methods

This section describes the methods and experimental setups used to calibrate each of the sensors and the linear power amplifier used to drive the excitation coils.

4.1   Linear Power Amplifier

A power amplifier was used to drive the excitation coils of the magnetic circuit and produce a magnetic field. For this experiment, a Kepco BOP 72–6M linear amplifier was selected based on its availability. The amplifier was operated in current control mode, so that the excitation coils produced magnetic fields proportional to the amplifier's input signal, where the proportionality factor is a function of the stress- and field-dependent magnetic permeability of the Galfenol rod.

The experimental setup for the calibration of the Kepco amplifier is shown in Figure 10. Static control voltages ($V_{control}$) were used to generate static currents in the load (R_{load}). The current output was calculated by measuring the voltage (V_{load}) across a purely resistive load using an Agilent 34410A precision multimeter, which was calibrated by the NASA Glenn Research Center Metrology Services Calibration Laboratory within the previous year. The load resistance was measured at room temperature by the four-wire method using the Agilent 34410A multimeter. The load was formed by four high-power resistors placed on a thick aluminum plate to minimize

temperature changes, which cause resistance changes. The current and voltage monitors were calibrated using a linear, least-squares regression as shown in Figure 11.

4.2 Load Cell

The load cell, its conditioning electronics, and its data acquisition channel were calibrated according to ASTM E4 (Ref. 6) by Absolute Calibration & Consulting Services, LLC, within the previous year.

4.3 Load Washer

The Kistler load washer and charge amplifier were calibrated together using the setup shown in Figure 12. Since the load washer cannot measure static forces, calibration was conducted quasi-statically at 10 Hz. To verify that 10 Hz was within the passband of the load washer system, the calibration was repeated for a 40-Hz force; results were within 0.2 percent of the 10-Hz calibration. The calibration factor was determined by comparing the magnitude of the primary harmonic (located at 10 Hz) of the load washer and load cell signals (Figure 13). The signals were measured at the same time with the same sampling rate and duration.

This calibration assumed that (1) the inertial force error in the load cell measurement was negligible at the calibration frequency of 10 Hz and (2) the resulting load washer calibration factors were constant throughout the operating frequency range (up to 1 kHz). Using Equation (24), the stiffness of the load cell (1 GN/m, or 6×10^6 lbf/in.), and the mass of the steel platen, the inertial force error at 40 Hz was 0.0067 percent. The natural frequency $\omega_{1,u}$ of the unloaded load washer is 65 kHz (mass $m_u = 0.003$ kg, or 0.007 lb). Natural frequencies decrease because of added mass; the natural frequency of the loaded load washer was approximated using

$$\omega_{1,l} = \omega_{1,u} \sqrt{\frac{m_u}{m_l}} \qquad (21)$$

where $m_l > m_u$. Using a conservative estimate for the effective mass during calibration, $m_l = 2$ kg (4 lb), the natural frequency reduced to 2.5 kHz, which was well above the frequency range of interest. This suggested that the calibration factor measured at 10 Hz should be valid up to 1 kHz.
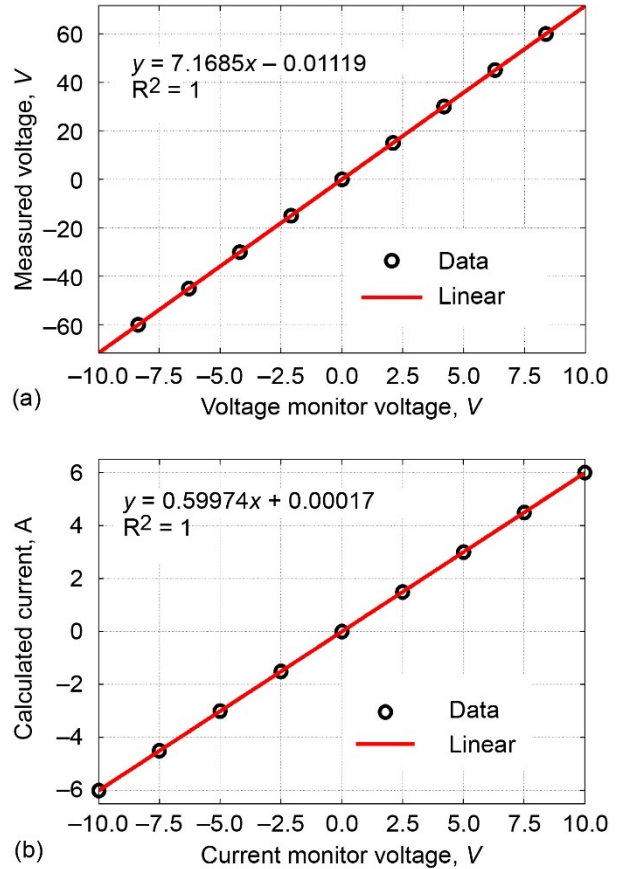

Figure 11.—Calibration of linear power amplifier using linear least-squares regression. (a) Voltage monitor. (b) Current monitor.
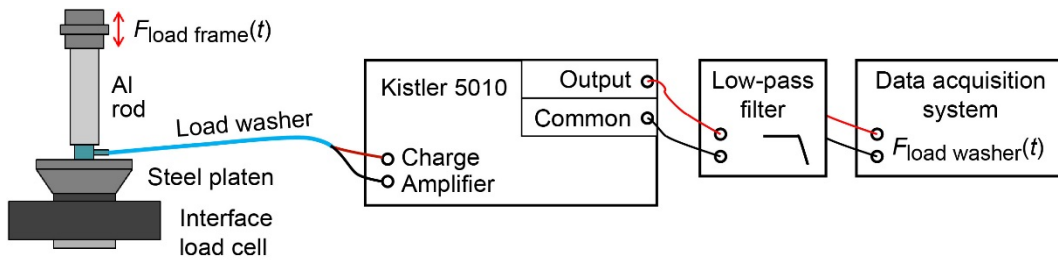

Figure 12.—Experimental setup for calibration of Kistler load washer and charge amplifier (not to scale), where $F_{\text{load frame}}$ is a dynamic force generated by load frame, and $F_{\text{load washer}}$ is force measured by load washer.
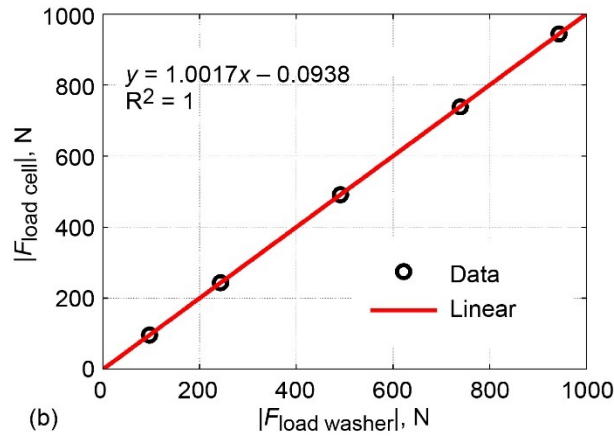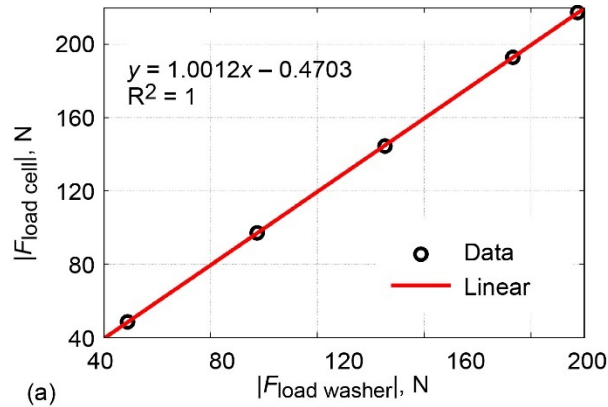
Figure 13.—Calibration of Kistler load washer and charge amplifier for 10-Hz force using linear least-squares regression. $F_{\text{load cell}}$ is force applied to specimen measured by load cell; $F_{\text{load washer}}$ is force applied to specimen measured by load washer. Each data point is average of results from six time captures. (a) 0 to 500 N range (250 N offset, 3.72 pC/N load washer sensitivity). (b) 0 to 2000 N range (1000 N offset, 3.87 pC/N load washer sensitivity).
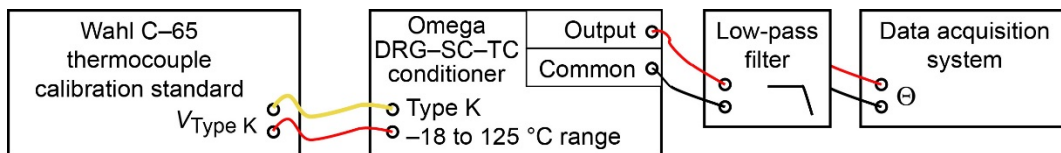
Figure 14.—Experimental setup for thermocouple calibration, where $V_{\text{Type K}}$ is simulated voltage of Type K thermocouple and Θ is measured temperature.

4.4   Thermocouple

The thermocouple signal conditioner was calibrated from 0 to 100 °C (32 to 212 °F) using a Wahl C–65 thermocouple calibration standard, which can output the precise voltage that would be generated by a Type K thermocouple at a specified temperature. During calibration, this voltage ($V_{\text{Type K}}$) was the source for the thermocouple measurement system (Figure 14). The calibration is shown in Figure 15. The calibration was validated by measuring the temperature of boiling water and ice water baths using the Wahl calibration standard and the thermocouple measurement system (Table IX).
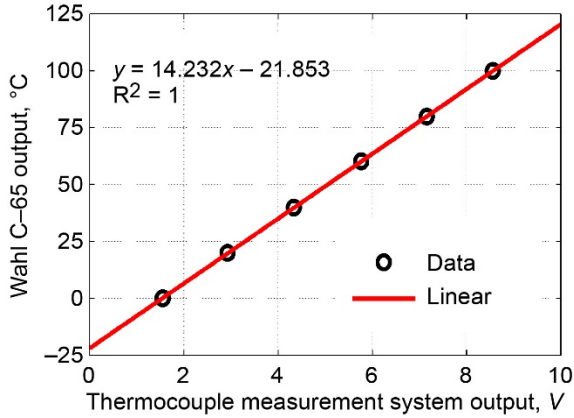
Figure 15.—Calibration of thermocouple using linear least-squares regression.

TABLE IX.—TEMPERATURE MEASUREMENT OF BOILING WATER AND ICE WATER BATHS AFTER CALIBRATION

[Tabulated values are averages of measurements obtained on 2 days.]

	Wahl calibration standard, °C (°F)	Thermocouple measurement system, °C (°F)
Ice water bath	0.2 (32.4)	0.7 (33.3)
Boiling water bath	99.7 (211.5)	99.8 (211.6)

4.5 Strain Gauge

The strain measurement system was shunt calibrated using the experimental setup depicted in Figure 16, where the pair of strain gauges is represented by a single, effective gauge of double the resistance ($2R_G$, see Sec. 3.4). The axial strain $S_{3,\text{sim}}$ simulated by shunting the effective gauge with a shunt resistor R_C at its terminals was found by calculating the change in resistance of the shunted arm of the Wheatstone bridge and using the definition of the gauge factor:

$$S_{3,\text{sim}} = \frac{-2R_G}{f_G(2R_G + R_C)} \tag{22}$$

For a Wheatstone quarter bridge, Equation (22) is exact for any strain level (Ref. 30). For the circuit in Figure 16, the simulated strain was -1952.5×10^{-6} m/m. The shunt calibration is given in Figure 17. This two-point calibration accurately scaled the strain measurement system. Instrument verification using a strain calibrator was not performed. The strain gauges on the laminated rod were found to have a calibration factor of -214.47×10^{-6} (m/m)/V.

$R_{\text{Wh3}} = R_{\text{Wh4}} = 350\ \Omega$, $R_{\text{Wh2}} = 2R_G = 700\ \Omega$
$R_C = 165{,}666\ \Omega$
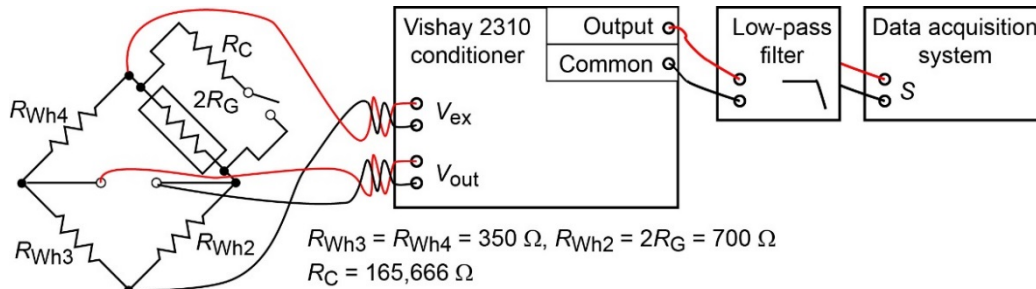
Figure 16.—Experimental setup for strain calibration, where R_C is shunt resistor; R_G is resistance of strain gauge; R_{Wh2}, R_{Wh3}, and R_{Wh4} are bridge completion resistors; V_{ex} is excitation voltage; V_{out} is Wheatstone quarter-bridge circuit output; and S is measured strain.


$y = -221.88x$
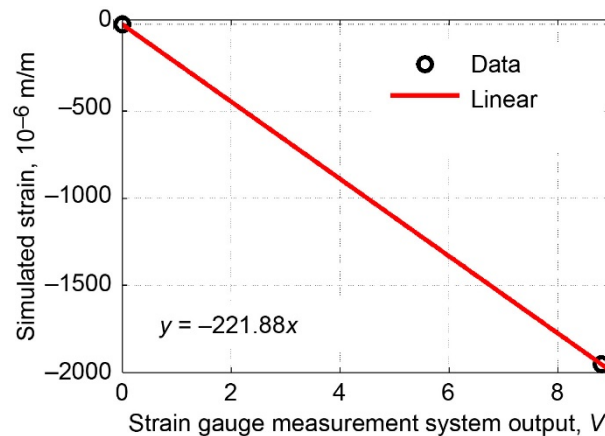
Figure 17.—Calibration of strain measurement system.

4.6 Hall Effect Sensor

The Hall effect sensor was calibrated by relating the Hall chip's output voltage (V_{DC}) to the magnetic field (H_{ref}) measured by a F.W. Bell 4048 gaussmeter and F.W. Bell 1435 Hall probe, which were calibrated by the manufacturer. The sensors were placed in the center of a uniform magnetic field that was generated by a Harvey-Wells Corporation electromagnet (Figure 18). The electromagnet's poles have a diameter of 30 cm (12 in.), about 2 orders of magnitude larger than each sensor's active area; thus, fringing of the magnetic field was negligible. Each sensor was independently rotated in the field until a maximum output was reached. Maximum outputs were recorded for 30 different static magnetic fields. The calibration results are shown in Figure 19.
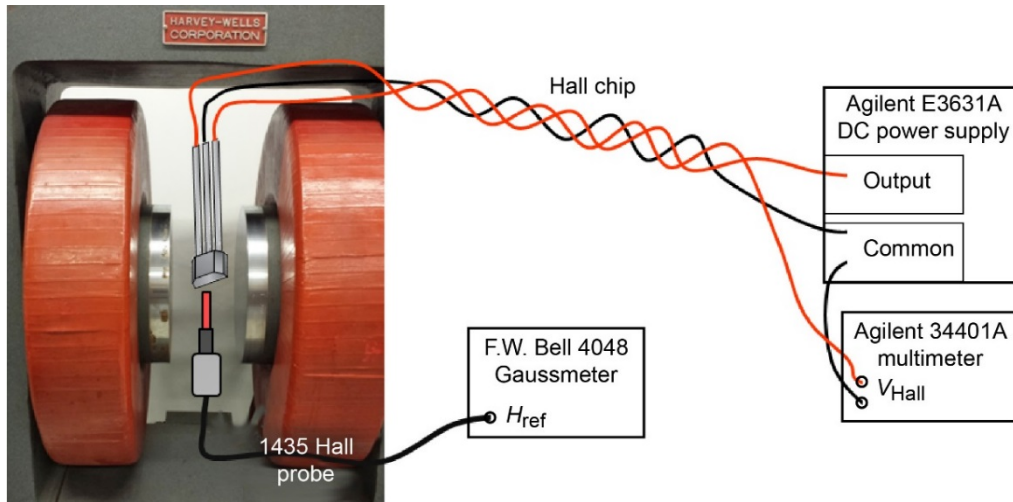

Figure 18.—Experimental setup for Hall effect sensor calibration (sensors not to scale). Hall chip supply voltage is 5.000 V, where H_{ref} is measured magnetic field and V_{Hall} is output voltage.
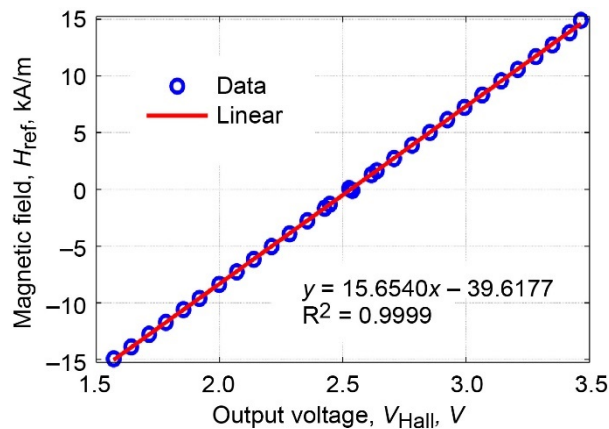

Figure 19.—The 30-point calibration of Hall effect sensor using linear least-squares regression.
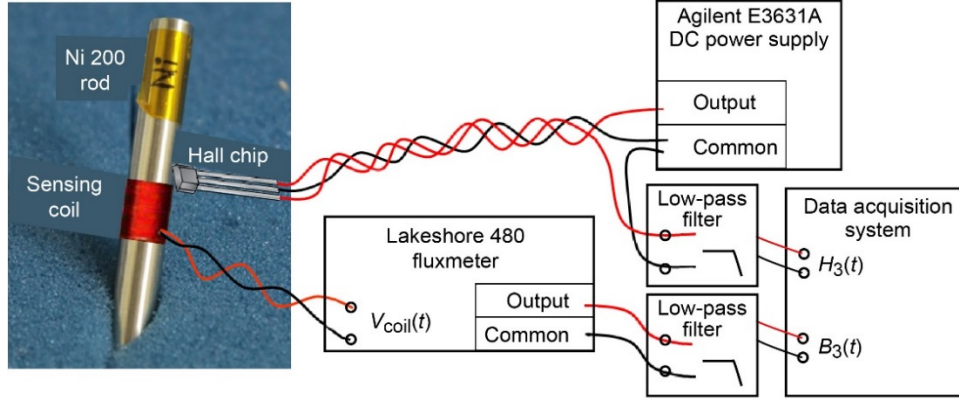
Figure 20.—Experimental setup for calibration of magnetic flux density sensing coil and fluxmeter, where V_{coil} is voltage induced in sensing coil, H_3 is axial magnetic field, and B_3 is axial magnetic flux density. Magnetic circuit shown in Figure 1 and Figure 2 was used to magnetize Ni 200 rod.

4.7   Magnetic Flux Density Sensing Coil

Magnetic flux density sensing coils can be calibrated using a reference magnet or known magnetic field (e.g., a field produced by a calibrated Helmholtz coil). In the absence of these instruments, calibration can be performed by measuring the magnetic response of a specimen for which an accurate measurement is available. In this experiment, calibration was conducted by measuring the magnetic response of a commercially pure nickel (Ni 200) rod having the same dimensions as the Galfenol specimen (Figure 20). The previously calibrated Hall chip was used to measure the applied magnetic field. The measured response was then compared with accurate measurements published in Reference 34, as shown in Figure 21. The calibration factor was determined as the factor that provided the closest fit (in a least-squares sense) of the measured response to the reference response.

In the laminated rod, the presence of adhesive layers reduces the cross-sectional area of Galfenol and thus the total flux linked by the sensing coil, which decreases the induced voltage in the coil. Consequently, if the calibration factor for the solid rod, c_{solid}^B, was used with the laminated rod, magnetic flux density measurements would be artificially low. A corrected calibration factor, c_{lam}^B, was calculated as

$$c_{lam}^B = c_{solid}^B A_{solid}^{FeGa} \left(A_{lam}^{FeGa} \right)^{-1} \qquad (23)$$

where A_{solid}^{FeGa} and A_{lam}^{FeGa} are the cross-sectional areas of Galfenol in the solid and laminated rods, respectively. The thickness of the adhesive layers was given by the manufacturer as 0.046 to 0.051 mm (0.0018 to 0.002 in.). Using an adhesive thickness of 0.048 mm (0.0019 in.), the lamination thickness of 0.84 mm (0.033 in.), and the rod's diameter of 6.27 mm (0.247 in.), the corrected calibration factor for the laminated rod was calculated as 4.936 T/V (49.36 kG/V).
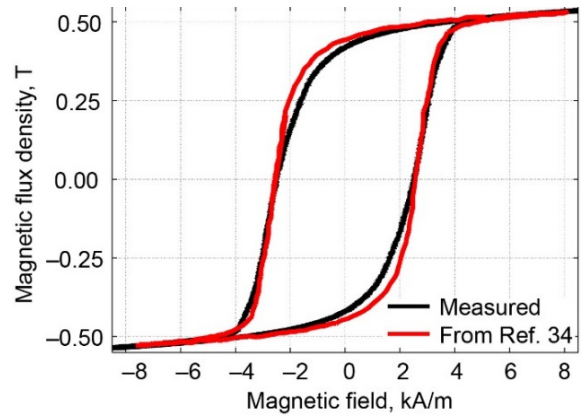
Figure 21.—Calibration of magnetic flux density measurement system, 4.673 T/V calibration factor (30-mV·s fluxmeter range).

5.0   Experimental Setup and Methods

This section details the experimental setup, including the physical setup and a wiring schematic, as well as the experimental techniques that were used to ensure the integrity of the data, including inertial force error reduction, strain gauge noise reduction, magnetic field control, and zeroing of the sensors.

5.1   Physical Setup

An MTS 831.50 dynamic load frame was used to excite the Galfenol specimen with quasi-static and dynamic axial forces up to –2000 N (–450 lbf) and 1 kHz (Figure 22). Because of the high stiffness of the specimen, the load frame was operated in force control mode, instead of displacement control mode; this was realized using an MTS 793 FlexTest GT controller. A closer look at the test setups used for quasi-static and dynamic chip, sensing coil, and strain gauges can be seen installed on the Galfenol rod. Surrounding the rod is the electromagnetic circuit used to generate the magnetic field.

Figure 23(a) focuses on the quasi-static test setup. The load cell, shown at the bottom of the picture, is used to measure the force in the rod and to provide feedback to the controller. Above the load cell is an aluminum platen, which supported the Galfenol rod and the electromagnetic circuit that surrounded the rod. There is also a thin plate sitting on the platen, which has a through hole for centering the rod. Above the setup is the load frame piston with a steel platen that was used to engage the sample.

As discussed in the following section, the mass in between the load cell and the sample (i.e., the platen, alignment plate, and the electromagnetic circuit) generated significant inertial forces that limited the accuracy of the load cell measurement at high frequency. As a result, the test setup was modified for dynamic testing to include an auxiliary force sensor. The physical setup is shown in Figure 23(b). Here, a load washer was placed on top of the platen. A circular scribe mark on the platen was used to visually center the load washer. Then a small steel part, shaped like a puck, was used to connect the sample to the load washer. The puck had a pin on the bottom side for alignment with the load washer, and a circular scribe mark on the top for alignment with the sample.

Figure 22.—MTS 831.50 load frame with experiment installed.
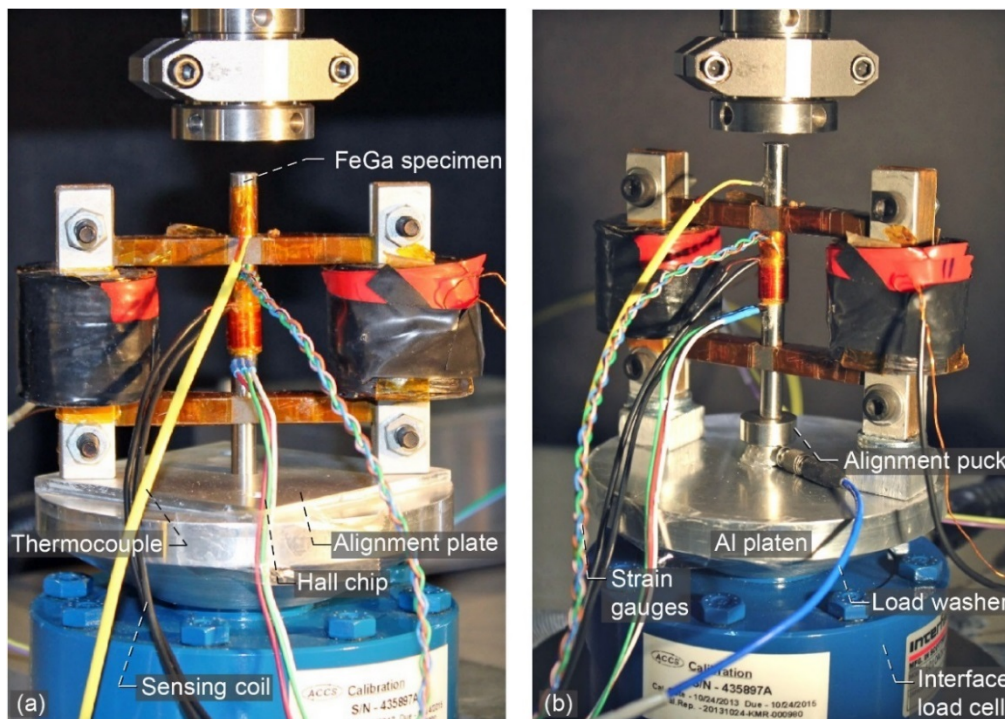
Figure 23.—Galfenol characterization physical setups. (a) Quasi-static. (b) Dynamic.

5.2 Inertial Force Error Reduction

Any moving mass in between the force transducer and sample will generate inertial force that corrupts the measurement. In the testing standard (Ref. 12) it is recommended that the inertial force error be ≤0.5 percent of the loading span. A lumped-parameters model, as shown in Figure 24, was used to estimate the error for the test setups used in this experiment. The fixtures are modeled as masses $m_{2,3}$, and the sample and force transducers are modeled as springs $k_{1,2,3}$, which experience axial forces $F_{1,2,3}$, respectively. In the quasi-static test setup, force is measured with the load cell, whereas in the dynamic setup, force is measured with the load washer.

The inertial force error is defined as the difference between the transducer force and the sample force, normalized by the loading span (the peak-to-peak dynamic force) of the sample force. Equations for the inertial force error associated with the quasi-static and dynamic cases are derived in Appendix C and can be expressed, respectively, as

$$\left|e_q\right| = \left|\frac{F_3 - F_2}{2|F_2|}\right| = \frac{m_3\omega^2}{2\left|k_3 - m_3\omega^2\right|} \tag{24}$$

and

$$\left|e_d\right| = \left|\frac{F_2 - F_1}{2|F_1|}\right| = \frac{1}{2}\left(1 + \left|\frac{k_2\left(k_3 - m_3\omega^2\right)}{m_2\omega^2\left(m_3\omega^2 - \left(k_2 + k_3\right)\right)}\right|\right)^{-1} \tag{25}$$

where ω is the circular frequency of the excitation force. In both cases, the error magnitude increases with the mass in between the sample and force transducer. In Figure 25 the error for each case is plotted versus frequency along with the error tolerance specified in the ASTM standard. Accordingly, the forcing frequency for the quasi-static case is limited to 213 Hz, whereas for the dynamic case the forcing frequency may be up to 1077 Hz before exceeding the error threshold. As noted in Section 3.2, forces up to 100 Hz were measured using the load cell, whereas forces above this cutoff were measured using the piezoelectric load washer. At 100 Hz, the error magnitude for the quasi-static case is 0.11 percent of the loading span. At 1000 Hz, the error magnitude for the dynamic case is 0.41 percent of the loading span.

5.3 Wiring

Figure 26 is a schematic representing the wiring for all of the measurement channels. This includes the interconnection between the sensors, signal conditioning, and data acquisition electronics, as well as grounding information. Noise was minimized by eliminating ground loops, through the use of shielded wire, and by separating the power and signal wires.
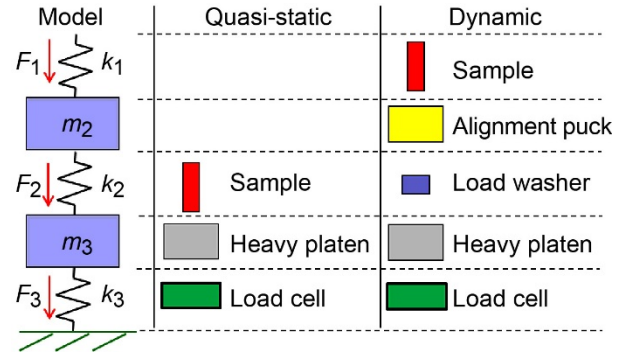
Figure 24.—Load path and mechanical model for inertial force error estimation in quasi-static and dynamic test setups, where $m_{2,3}$ are fixtures modeled as masses, $k_{1,2,3}$ are sample and force transducers modeled as springs, and $F_{1,2,3}$ are the forces they experience.

(a)

(b)
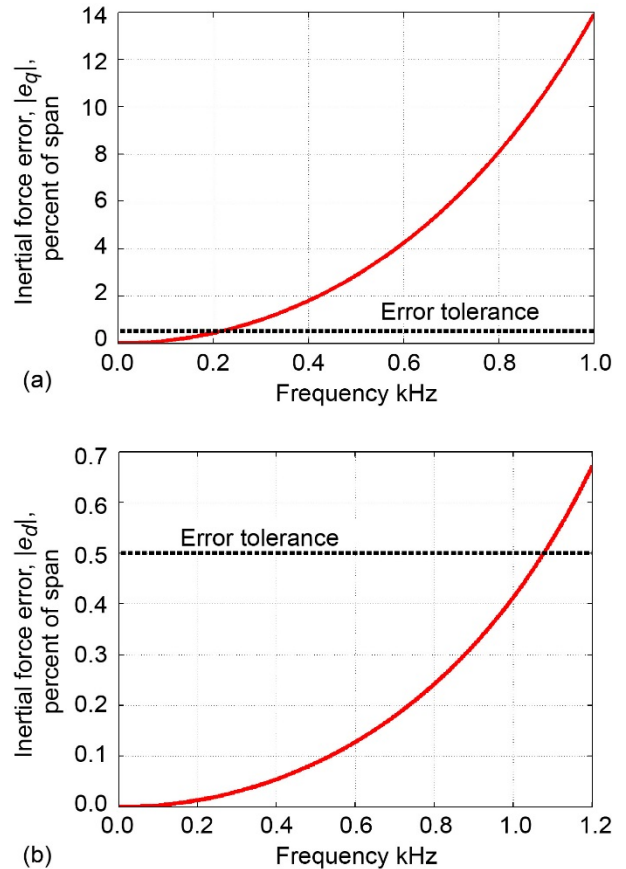
Figure 25.—Measurement error in the force applied to the specimen due to the inertial force of fixturing, determined by lumped-parameters model (see Figure 24) where the load cell and load washer are modeled as springs k and the puck and platen are modeled as masses m; $k_3 = 175\times10^6$ N/m and $m_3 = 0.965$ kg. (a) Quasi-static case. (b) Dynamic case; $k_2 = 1\times10^9$ N/m and $m_2 = 0.025$ kg.

The following NI PXI system channels will be aquired:

Card 1
Ch 0: Load (Interface 1010 load cell)
Ch 1: Piston displacement (MTS LVDT 331.05)
Ch 3: Dynamic force (Kistler 9001A load washer)
Ch 4: Strain (Micro-Measurements EA-06-250BF-350 (x2) via Vishay 2310)
Ch 5: Amplifier voltage (Kepko 72-6M monitor)
Ch 6: Amplifier current (Kepko 72-6M monitor)

Card 2
Ch 0: Temperature (NASA thermocouple via Omega system)
Ch 5: Magnetic field (Allegro A1321-LUA Hall effect sensor)
Ch 6: Flux density (Custom sensing coil via Lakeshore 480 fluxmeter)

dSPACE
(Constant field)

Agilent scope/ generator
(Constant current)

Out   CG
Coaxial

control

Kepco 72-6M

Monitors
V   I

Magnetic circuit

Magnetic field sensor
Allegro A1321-LUA

Ext + (red)
Out + (Grn)
Out – (wht)
Ext – (blk)
2 shielded twisted pair

MTS system connections

Interface 1010
500 lbf
Small load cell

331.05
LVDT

493.40 Accel transition card

Front panel: 493.40 I/O carrier

Signal cond. 493.21B
Signal cond. 493.21B
Signal cond. 493.21B

Signals filtered by a 20kHz 5-pole Butterworth

MTS GT controller

Service port Front slot 3
LAN1 Front slot 1

RJ45

Cat5

Junction

RJ45 connector	
Pin	Description
1	Load
2	GND
3	LVDT
4	GND
5	Accel
6	GND

CG

CG
Load washer
Kistler 9001A

Coaxial

Kistler 5010B 10kHz filter

(-10 to 10V)   CG

Vishay 2310

(-10 to 10V)

(-10 to 10V)

Thermocouple Yellow+, red-

Agilent 3631A DC Power supply   CG

2 shielded twisted pair (no drain)

Thermocouple ports
1 2 3 4

2-conductor wire w/ shield

Omega DRG-SC-TC Signal conditioners

Signal ground block

16Ω ground strap

(0 to 10V)

Coil

30 AWG magnet wire

Fluxmeter
CG

(0.4 to 4.8V))

(+-3V)

Coaxial   Coaxial

BNC 1 2 3 4 5 6 7 8   BNC 1 2 3 4 5 6 7 8

Marchand Filter #1
-10kHz, 8-pole Butterworth
-100k Ohm inputs

1 2 3 4 5 6 7 8
0 1 2 3 4 5 6 7

NI-2705 terminal block #1

Marchand Filter #2
-10kHz, 8-pole Butterworth
-1M Ohm inputs

1 2 3 4 5 6 7 8
0 1 2 3 4 5 6 7

NI-2705 terminal block #2

NI-6123 ADC card #1
-Differential inputs
-Simultaneous sampling
-16 bit, use 40kHz

NI-6123 ADC card #2
-Differential inputs
-Simultaneous sampling
-16 bit, use 40kHz

LAN1

NI PXI-8119 controller

-Windows 7 64 bit
-i7 2.3 GHz processor
-250 GB drive for continuous use
-8GB ram

National Instruments PXI system

Key
— — Input and output are ground isolated
CG = Common ground
Chassis ground
Verify that signal is not grounded at this point
Verify that sensor housing is grounded
Ground within instrument or via external cable

Figure 26.—Wiring for all measurement channels in Galfenol specimen testing.

5.4   Strain Gauge Noise Reduction

As detailed in Section 2.3, a time-varying magnetic flux through a surface (e.g., the cross section of the Galfenol rod) induces a circulating electric field along the boundary of the surface. This electric field creates noise voltages in the grid of the strain gauges that were attached to the rod's surface. Since the gauges used in this experiment were oriented to measure axial strain in the rod, the noise voltage was only generated in the narrow, horizontal links of the grid; thus, long and narrow strain gauge grids were ideal for minimizing electromagnetic noise. The electromagnetic noise can be directly measured at the strain gauge terminals after setting the bridge excitation to 0 V.

To investigate the effect of electromagnetic noise V_{noise} on a quarter-bridge strain measurement, the circuit shown in Figure 27 was analyzed in Appendix D. The normalized strain error due to the electromagnetic noise is

$$e_S = \frac{S - S_{true}}{S_{span}} = \frac{V_r\left(f_G S_{true} + 2\right)}{f_G S_{span}\left(1 - V_r\right)} \tag{26}$$

where S is the measured strain, S_{true} is the true strain, S_{span} is the strain span (1350×10^{-6} m/m for this experiment), f_G is the gauge factor, and V_r is the normalized noise voltage,

$$V_r = \frac{V_{noise}}{V_{ex}} \tag{27}$$

with V_{ex} being the excitation voltage.

The strain error is plotted in Figure 28. Clearly, the strain error is a very weak function of the true strain magnitude; however, the error increases significantly as a function of the normalized noise voltage. For a typical bridge excitation of 10 V, an electromagnetic noise voltage of 10 mV results in a strain error of about 100 percent. Figure 29 shows a direct measurement of the electromagnetic noise voltage during a 3-MPa (435-psi) amplitude, 1-kHz excitation of a Galfenol rod in a similar experiment, where no noise reduction techniques were utilized. The measured noise voltages correspond to strain errors of 200 percent or larger. Thus, noise reduction techniques were required for accurate strain measurement, especially for high-frequency, large-amplitude forces.
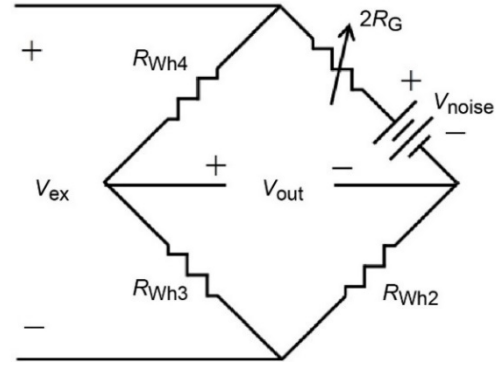

Figure 27.—Wheatstone quarter-bridge strain measurement circuit considering electromagnetic noise V_{noise} (leadwire resistance neglected). Here, R_G is resistance of strain gauge; R_{Wh2}, R_{Wh3}, and R_{Wh4} are bridge completion resistors; V_{ex} is excitation voltage; and V_{out} is total Wheatstone quarter-bridge circuit output.
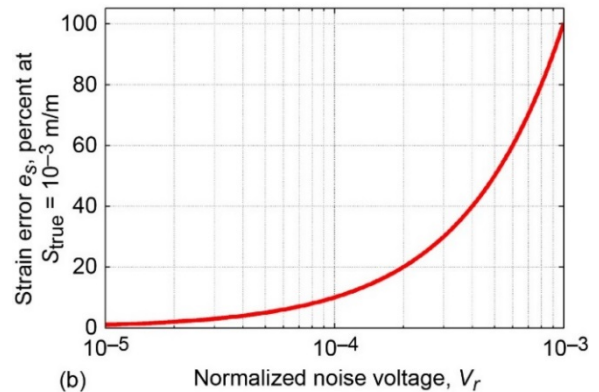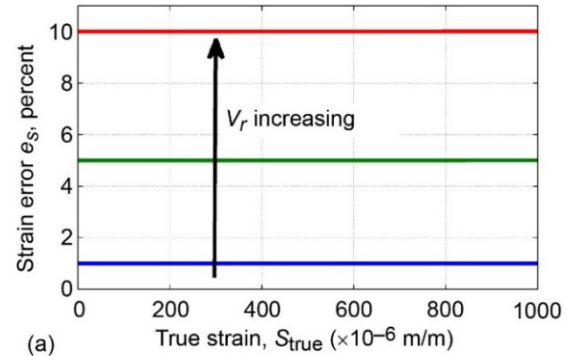
Figure 28.—Error in strain measurement due to electromagnetic noise for gauge factor f_G = 2.155. (a) Effect of true strain magnitude. (b) Effect of normalized noise voltage.
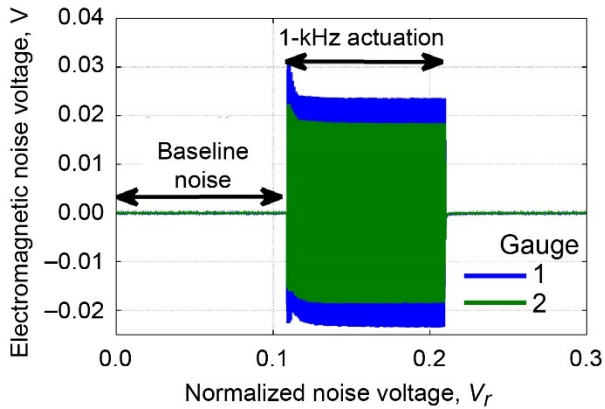
Figure 29.—Electromagnetic noise voltage induced in two strain gauges and their leadwires in response to 3-MPa-amplitude, 1-kHz axial stress applied to $Fe_{81.6}Ga_{18.4}$ rod.


Figure 30.—Weaving pattern for strain gauge leadwires to reduce electromagnetic noise induced in wires (from Ref. 24). At terminals, wire 1 is connected with 2 and wire 3 with 4. (a) Construction. (b) Finished cable.

Electromagnetic noise was reduced by (1) weaving leadwires in the pattern shown in Figure 30, (2) routing leadwires as far away from the noise sources as possible and in a direction orthogonal to the rod's circumference and the perimeter of the laminates' cross section, and (3) wiring the two gauges in series such that the noise induced in one cancels that induced in the other (Figure 31). Typically, strain is measured separately by two gauges located on opposite sides of the rod, and the average strain is reported (Ref. 35); this allows for the identification of bending-induced differences in the strains and, if necessary, the correction of the specimen's mount. Wiring two identical strain gauges in series (as shown in Figure 31) to form a Wheatstone quarter bridge causes the individually measured strains to be averaged, but it does not allow for an assessment of the specimen's mount. Although the ends of the specimen were ground to a tight tolerance (see Sec. 2.4) and the load frame is very stiff and well aligned, achieving even contact pressure between the platens and specimen necessitates the use of a spherical platen, especially when the specimen is stiff (Ref. 10). However, a lightweight spherical platen was not available. Thus, bending of the specimen is a point of uncertainty in this experiment.

To quantify the performance of the noise reduction techniques, the electromagnetic noise in the strain measurement was measured in situ by dynamically exciting the Galfenol specimen while measuring the strain with the strain bridge excitation voltage set to zero. The noise was measured for a constant current of 0.3 A applied to the electromagnets and an applied force of

$$F = 681 + 586 \sin(2\pi f t) \text{ N} \qquad (28)$$

At quasi-static frequencies, this loading caused the largest and steepest change in flux density (see Sec. 8.2.1). Thus, this loading provided the worst-case scenario for electromagnetic
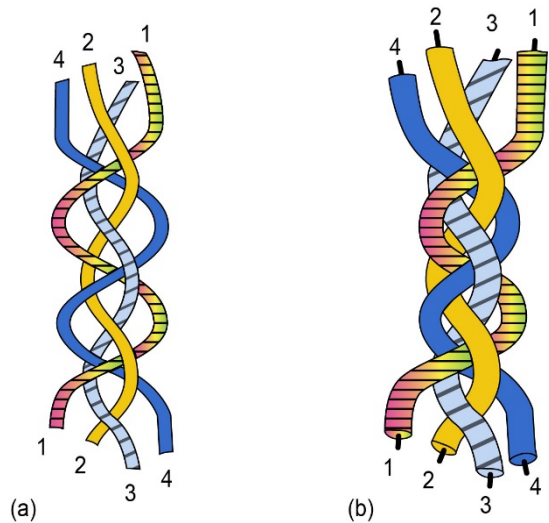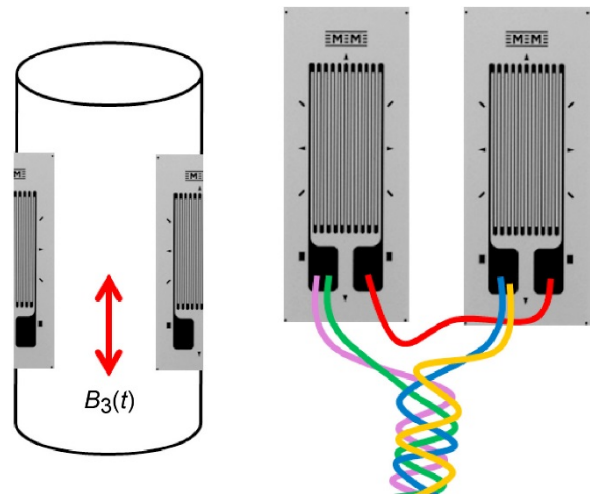

Figure 31.—Wiring of strain gauge pair to simultaneously cancel bending strains and electromagnetic noise. Gauges are bonded to opposite sides of test specimen, but are in otherwise identical locations and orientations. $B_3(t)$ is axial magnetic flux density.

noise throughout the forcing frequency range. The resulting electromagnetic noise for the solid Galfenol specimen over a range of forcing frequencies is shown in Figure 32(a). The noise-reduction techniques were very effective, as the electromagnetic noise peaks at about 10×10^{-6}, or 0.74 percent of the strain span. As seen in Figure 32(b), the amplitude of the magnetic flux density response decreased significantly with frequency, which was due to eddy currents in the solid Galfenol rod. This behavior helped to reduce the electromagnetic noise, because the induced voltage is directly related to the time
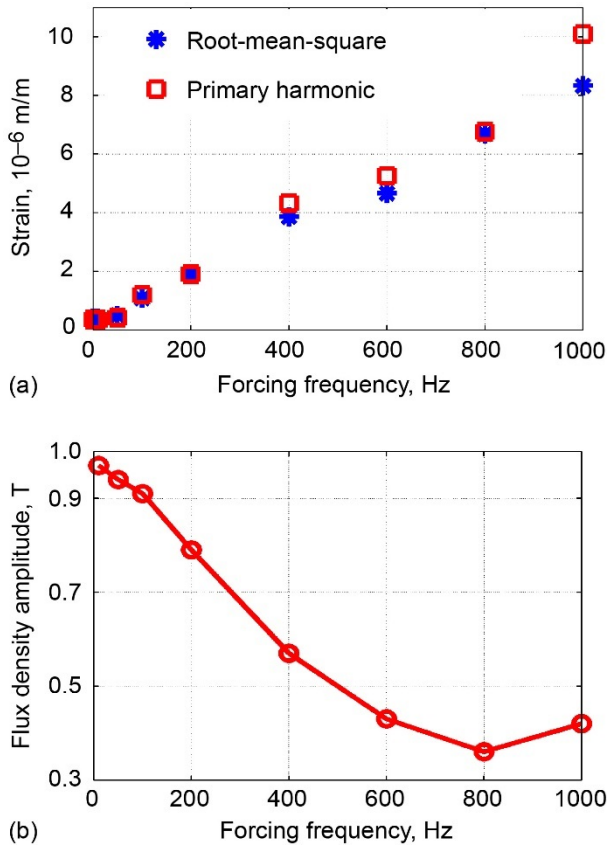
Figure 32.—Electromagnetic noise under application of noise reduction techniques. (a) Measured strain noise of solid Galfenol rod for worst-case loading under constant current to electromagnets (noise is quantified in terms of its root-mean-square and amplitude of its primary harmonic). (b) Amplitude of magnetic flux density response at each frequency.

derivative of the flux density. For the laminated Galfenol rod, the decay of the flux density amplitude was less severe, which likely led to slightly larger electromagnetic noise.

5.5 Magnetic Field Control

When the current in the electromagnet is held constant while the magnetostrictive sample is stressed, the magnetic field in the sample changes because of its stress-dependent magnetic permeability (Ref. 36). In Galfenol, this effect is significant, because its magnetic permeability is a strongly nonlinear function of stress; Galfenol's magnetic permeability can vary by almost 3 orders of magnitude (Ref. 19). The variation in magnetic field with the applied stress confounds the measured results, and so a feedback control system was used to adjust the current to achieve a more constant field. Magnetic field control was implemented in addition to constant current control, rather than as a replacement for it, because constant current control could be realized over a greater bandwidth.

The control system is schematically illustrated in Figure 33 for the case of a proportional-integral-derivative- (PID-) type control law. A dSPACE DS1103 board was used to implement real-time control. Feedback was provided by the Hall sensor, and the controller's output drove the amplifier's current control input. The PID gains were tuned for disturbance rejection by attempting to hold the field constant while dynamically loading the specimen. Initially, the D gain was set to zero because of the relatively noisy magnetic field signal. To reduce the noise, an analog low-pass filter was inserted in the feedback loop. This allowed for the derivative term to be used, but that provided a negligible improvement in the control performance. Therefore, the D term was set to zero (effectively PI control) and the filter was removed to reduce the time delay of the control system. For
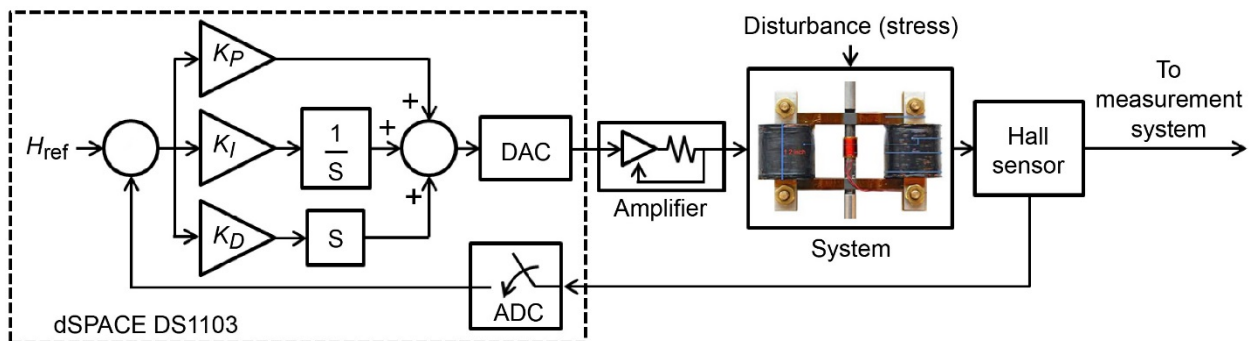

Figure 33.—Magnetic field control system, which is independent of measurement system and thus only includes signal conditioning depicted here. H_{ref} is reference magnetic field; K_P, K_I, and K_D are proportional, integral, and derivative control gains, respectively; DAC is digital-to-analog converter; and ADC is analog-to-digital converter.

dynamic sensing experiments, one set of gains (P = 2, I = 100) was used for frequencies ≤600 Hz and another set (P = 0.5, I = 100) for frequencies >600 Hz in order to provide adequate control over the range of forcing frequencies. To improve control performance, the sampling rate of the dSPACE system was maximized. The maximum rate was 150 kHz. The control system performed well up to 100 Hz, but the performance considerably degraded above 200 Hz.

Sliding-mode and lookup-table methods of control were briefly evaluated as alternatives to PID. It was found that the sliding-mode control performed comparably; however, sliding-mode control required larger voltages than for PID control. As frequency was increased, the required switching voltages exceeded the capabilities of the amplifier. To implement lookup-table control, the relationship between current, stress, and magnetic field was measured. For each operating frequency, the data were catalogued in a table through a series of measurements with constant applied current and varying stress. The appropriate control output was then based on referencing the table to find the required output current to achieve a constant field for the given operating frequency and the measured stress level. This control method was not successfully implemented because it required too many measurements to produce a lookup table of sufficient resolution. In addition, the control processor could not access the table values fast enough to implement this method in real time at high frequency. Given the limitations of sliding-mode and lookup-table control, PI control was used for all characterization tests where constant field was desired.

5.6   Sensor Reset

The zero offset of each of the magnetic field, temperature, voltage, and current sensors was quantified during sensor calibration. However, the output of magnetic flux density and strain sensors had to be periodically reset during testing because of thermally induced drift. The reference state at which these sensors were zeroed was well defined and consistent throughout testing, as detailed below.

Drift in the magnetic flux density measurement was minimized through manual and automatic adjustment of the fluxmeter's drift correction circuitry. Additionally, the fluxmeter integrator was manually reset about every minute to avoid appreciable drift error. Typically, the integrator is reset when the magnetostrictive material is in a zero flux state. In this work, a faster, alternative method was used because of the extensive testing matrix. First, the fluxmeter was reset using the conventional method. Then, the quasi-static sensing response of

the Galfenol rod was measured for a single constant current (or magnetic field) level. Next, a point in the saturated region of the response was selected, and the corresponding flux density, stress, and current (or field) were recorded. Finally, when a reset was needed, the stress and current (or field) were held constant at the recorded values while the integrator was reset. The fluxmeter then output the flux density relative to the recorded value. Since the recorded point was in the saturation region and Galfenol exhibits a high degree of kinematic reversibility (see Sec. 8.3), the loading history used to reach the recorded stress and current (or field) had a negligible influence. For the solid Galfenol rod, the integrator was reset at –50±1 N (–11±0.22 lbf) and either 1 A or 15 kA/m, for which the flux density was either 1.599 T (15.99 kG) or 1.601 T (16.01 kG), respectively. For the laminated rod, the integrator was reset at –50±1 N (–11±0.22 lbf) and 1 A, for which the flux density was 1.474 T (14.74 kG). The true flux density was calculated in postprocessing by adding the recorded value to the measured flux.

To minimize the drift in the strain signal while maintaining an appropriate signal-to-noise ratio, a Wheatstone bridge excitation of 7 V was used. This excitation was only about 40 percent of the estimated maximum excitation voltage, which was calculated according to Reference 37. First, a saturating magnetic field was established, then the field was reduced to zero. The strain signal was then zeroed at zero applied current (or magnetic field) after disengaging the load frame piston from the specimen. Because of hysteresis, the strain in Galfenol at this state was not zero, but rather 0.6×10^{-6} m/m (determined from actuation measurements). Thus, all strain signals were reduced by this value in postprocessing.

6.0   Data Processing Methods

This section details the methods used to postprocess the measured signals and calculate the material properties of the Galfenol specimens.

6.1   Amplitude Calibration

Figure 34 shows the "signal flow diagram," which represents how each sensor signal was scaled during acquisition. The green section of the diagram shows how the signals were modified by the sensors and electronics, and the blue section shows the calibration factors applied to restore the physical meaning of the signals. Phase correction of the signals was handled in postprocessing, as explained in the following section.
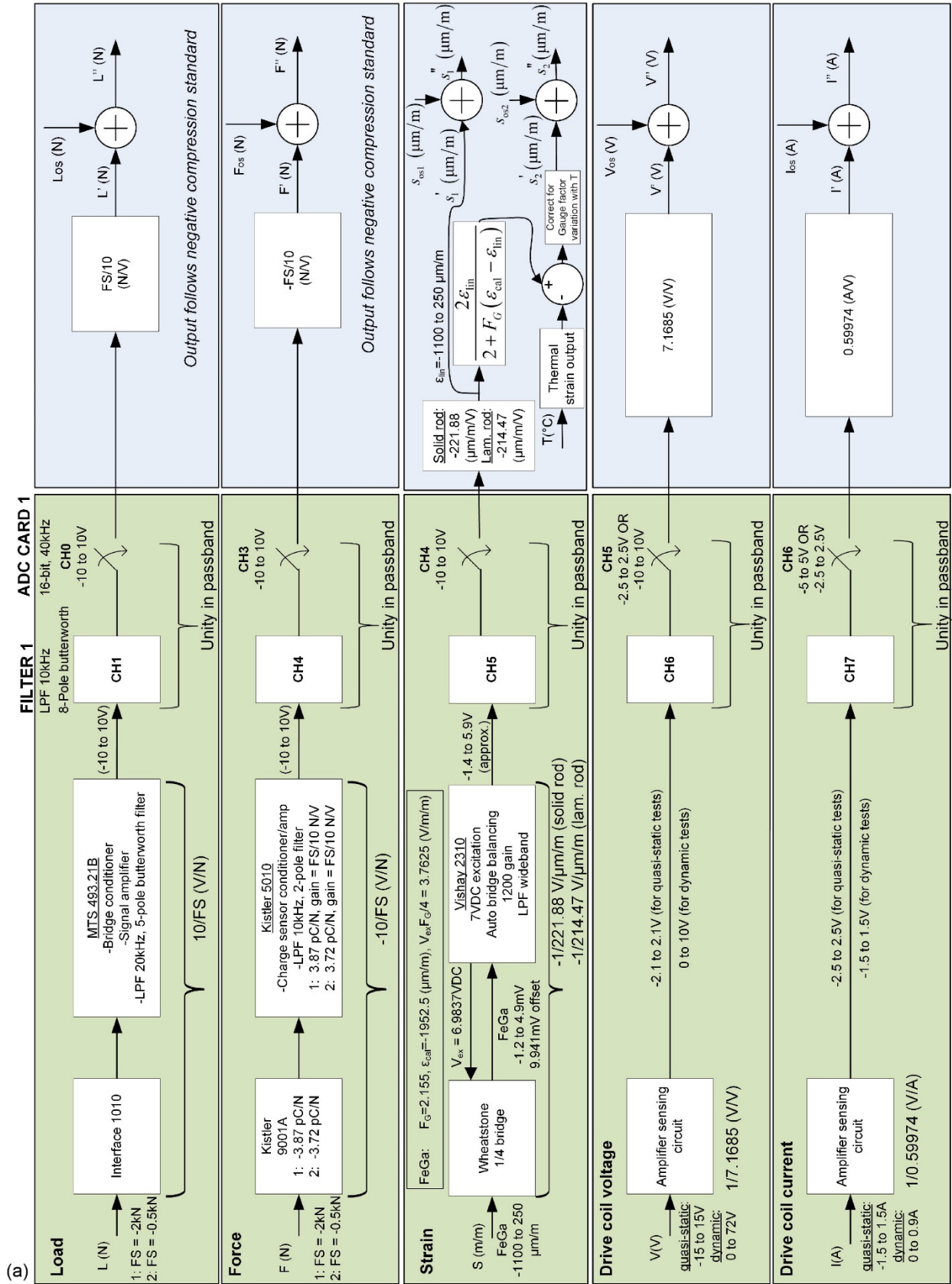
Figure 34.—Signal flow diagram. (a) Mechanical and electrical quantities.
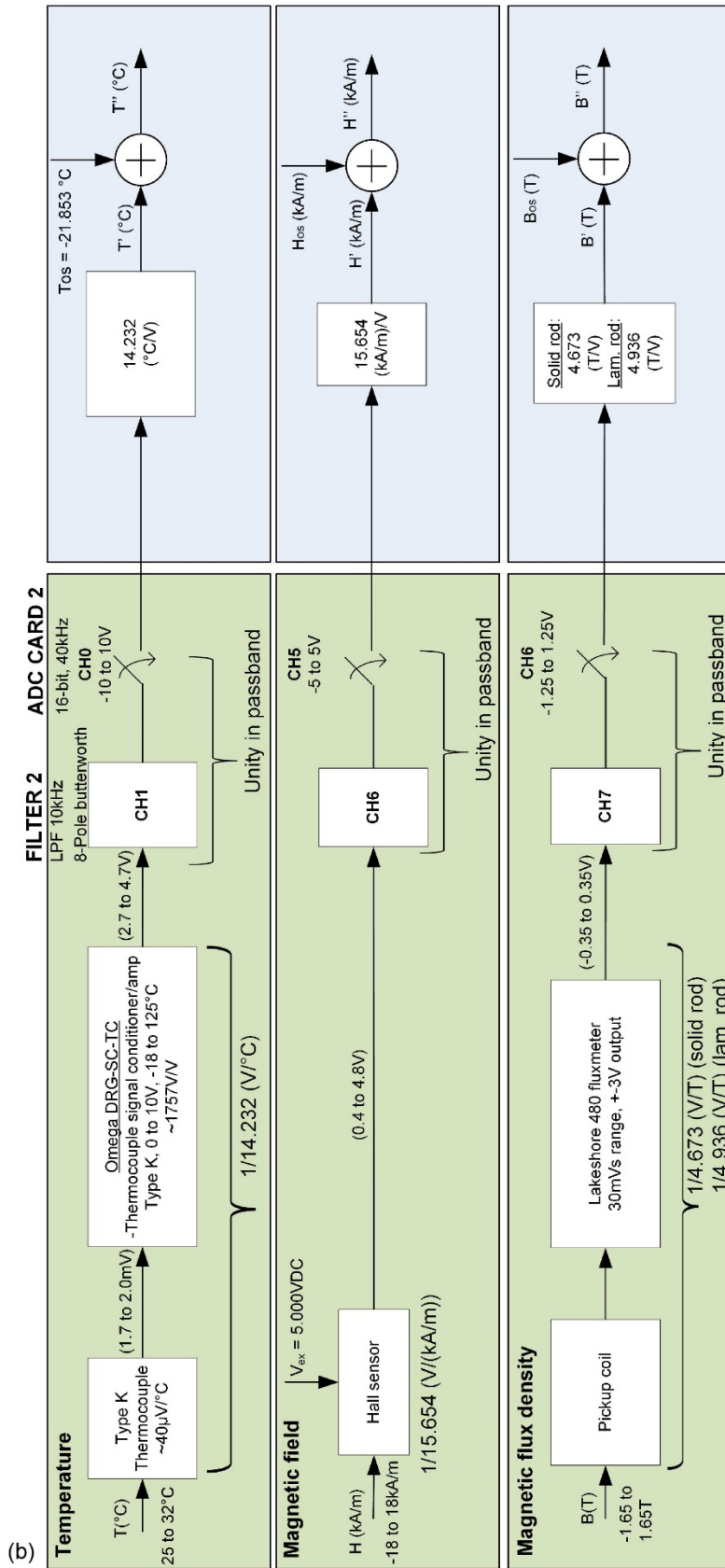
Figure 34.—Concluded. (b) Thermal and magnetic quantities.

6.2   Phase Calibration

Each signal conditioner and corresponding anti-aliasing filter created a different phase shift, resulting in misalignment of the measured sensor signals. This misalignment created error in the size of the material characterization hysteresis loops. Typically, force and displacement signals are aligned by testing a sample that has near-zero energy loss (e.g., Ref. 7). This technique could not be applied for this system, as the mechanical and magnetic sensor signals needed to be mutually aligned. Instead, a new technique was used.

As shown in Figure 35 and explained below, the sensors were removed and the sensor signals were simulated by manipulating a voltage signal produced by a function generator:

- Strain sensor: This sensor uses a strain bridge circuit, which produces a millivolt-level signal proportional to the applied strain. This was simulated using a voltage divider to attenuate the function generator signal while presenting the bridge resistance to the signal conditioner.
- Load cell: This sensor also uses a strain bridge circuit, producing a millivolt-level signal proportional to the applied force. The same voltage divider circuit used for the strain sensor was used.
- Load washer: This sensor uses a piezoelectric crystal that generates charge in proportion to the applied stress. A capacitor was therefore placed in series with the function generator, so that the voltage signal was converted into a charge signal. Considering that charge = capacitance × voltage, the capacitance was scaled to create a charge level similar to the sensor.

- Magnetic field sensor: This sensor produces a voltage proportional to the applied field. The function generator was used directly to represent this signal.
- Pickup coil: This sensor produces a voltage proportional to $-dB/dt$, where B is the magnetic flux density. This implies a phase shift of $-\pi/2$ between the flux density and voltage signals. This phase shift was not simulated. However, the fluxmeter is an integrator, and therefore introduced an additional $-\pi/2$ phase shift. Consequently, the total phase shift was implemented in postprocessing by multiplying the flux density signal by -1. Here, a voltage divider circuit was used to adjust the voltage level and match the resistance of the pickup coil. Additionally, an isolation amplifier was placed in between the function generator output and the voltage divider, because the fluxmeter requires a floating input to operate correctly.

The phase delay of each channel was measured with respect to the magnetic field sensor channel at multiple frequencies. During a test, the function generator signal was simultaneously sent to the magnetic field sensor channel and the channel under test. The output data were then acquired and saved.

Assuming that the electronics behave linearly, each measurement channel in Figure 35 can be represented as a block diagram, where each piece of equipment is described by a transfer function $G_g(s)$. To illustrate how the phase response of each channel was calculated, the magnetic flux density channel is considered (Figure 36).
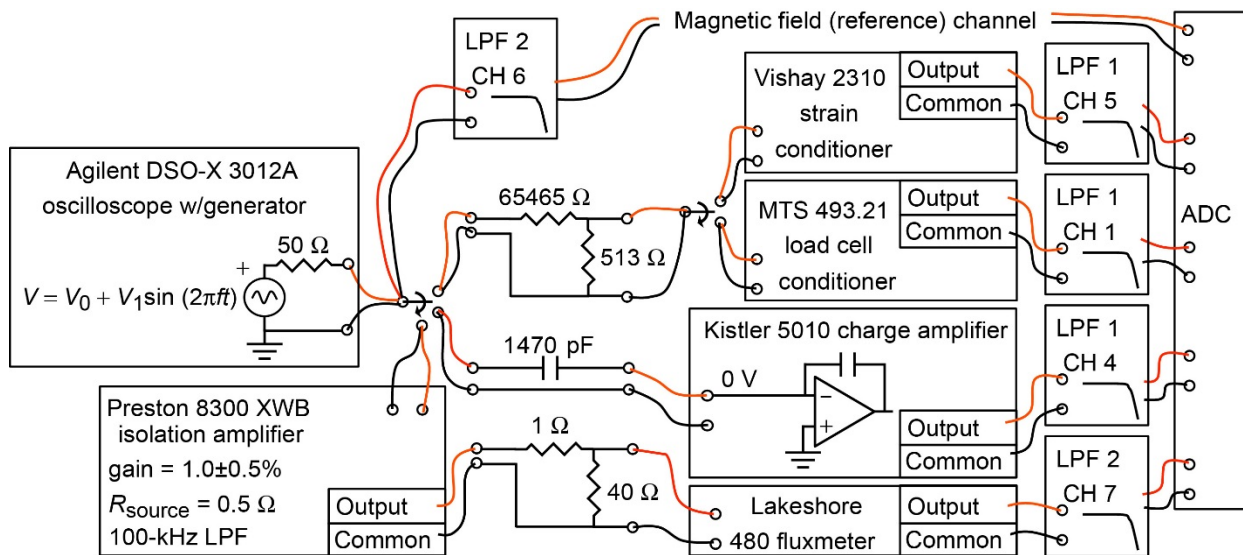

Figure 35.—Experimental setup for measuring phase response of conditioning electronics at frequency f for strain, load cell, load washer, and flux density signals. Here, V is voltage produced by generator, V_0 is voltage offset, V_1 is voltage amplitude, t is time, R_{source} is amplifier's source impedance, LPF is low-pass filter, CH is channel, and ADC is analog-to-digital converter.

For harmonic generator signals, the measured signal in Figure 36 as a function of the base imaginary number j and the circular frequency ω of the generated voltage is

$$B(j\omega) = K G_4(j\omega) G_3(j\omega) G_2(j\omega) G_1(j\omega) V(j\omega) \qquad (29)$$

where $V(j\omega)$ is the generated signal. By expressing each transfer function in terms of its magnitude $M_g(\omega)$ and phase $\phi_g(\omega)$, Equation (29) becomes

$$B(j\omega) = M(\omega) \exp\left[j\phi(\omega) \right] V(j\omega) \qquad (30)$$

where $M(\omega)$ and $\phi(\omega)$ are the magnitude and phase response, respectively, of the measurement channel in Figure 36:

$$M(\omega) = K M_4(\omega) M_3(\omega) M_2(\omega) M_1(\omega) \qquad (31)$$

and

$$\phi(\omega) = \phi_4(\omega) + \phi_3(\omega) + \phi_2(\omega) + \phi_1(\omega) \qquad (32)$$

From Equation (32), it is clear that the phase response of each measurement channel is simply a summation of the phase responses of the conditioning electronics. Further, the phase response of the magnetic flux density channel relative to that of the magnetic field channel, $\phi^{B/H}(\omega)$, can be calculated by subtracting the phase responses of the isolation amplifier and magnetic field channel; that is,

$$\phi^{B/H}(\omega) = \phi^B(\omega) - \phi^H(\omega) = \phi(\omega) - \phi_1(\omega) - \phi^H(\omega) \qquad (33)$$

By applying the time shift property of Fourier transforms to Equation (30) followed by an inverse Fourier transform, the measured signal can be written in the time domain as

$$\begin{aligned} B(t) &= M(\omega) V\left(t + \frac{\phi(\omega)}{\omega} \right) u\left(t + \frac{\phi(\omega)}{\omega} \right) \\ &= M(\omega) V(t - t_d) u(t - t_d) \end{aligned} \qquad (34)$$

where $u(t)$ is the step function and $t_d = \phi(\omega)/\omega$ is the time delay imposed by the measurement system. If the flux density signal is phase referenced to the field signal, the time delay becomes the time delay of the flux density channel relative to the time delay of the field channel,

$$t_d \rightarrow -\frac{\phi^{B/H}(\omega)}{\omega} = -\frac{\phi^B(\omega) - \phi^H(\omega)}{\omega} = t_d{}^B - t_d{}^H = t_d{}^{B/H} \qquad (35)$$

Points on the phase response $\phi^{B/H}(\omega)$ were measured by first generating a single-tone sinusoid and extracting the phase of the measurement and field signals at the frequency of the sinusoid from discrete Fourier transforms (DFTs) of the two signals. Then the phase response of the isolation amplifier (measured independently) and field channel were subtracted according to Equation (33). Finally, the relative time delay was calculated as the slope of a linear, least-squares regression of $\phi^{B/H}(\omega)$. The relative phase response and time delay of the other channels were measured in an analogous manner. This method assumes that the phase response of the analog-to-digital (A/D) converter is equal for all channels.

Figure 37 presents the measured phase response of each measurement channel (conditioner and corresponding low-pass filter) relative to the magnetic field channel. Table X summarizes the linear, least-squares regression of each response. The dynamic force channel has a $-\pi$ offset, because the charge amplifier contains an inverting op-amp. The flux density channel has a $-\pi/2$ offset as discussed above. For frequencies below ~100 Hz, the phase response of the charge amplifier becomes nonlinear due to discharge circuitry, which creates a high-pass filter effect. Consequently, only higher frequencies were used for linear regression.

6.3 Filtering

Filtering was performed during postprocessing to reduce noise. Filtering was implemented using MATLAB's *filtfilt* function combined with a digital Butterworth low-pass filter having a passband ripple of 0.0043 dB (0.1 percent after forwards and reverse filtering). This filtering introduced zero phase distortion. Selection of the passband cutoff frequency was guided by DFTs of the response variables (strain and magnetic flux density). The forcing frequency and the level of nonlinearity in the response were different for each group of measurements; thus, a different cutoff frequency was used for each group, as discussed below.

Generator signal — Isolation amplifier — Circuit — Fluxmeter — LPF — ADC — Measured signal

$$V(s) \rightarrow \boxed{G_1(s)} \rightarrow \triangleright K \triangleright \rightarrow \boxed{G_2(s)} \rightarrow \boxed{G_3(s)} \rightarrow \boxed{G_4(s)} \rightarrow B(s)$$
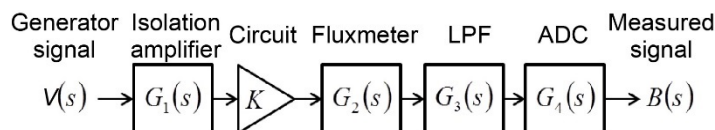
Figure 36.—Magnetic flux density channel during phase response measurement, where $V(s)$ is generated voltage, $G(s)$ is transfer function, K is gain of voltage scaling circuitry, and B is magnetic flux density. LPF is low-pass filter and ADC is analog-to-digital converter.

TABLE X.—LINEAR, LEAST-SQUARES REGRESSION OF PHASE RESPONSES OF
CONDITIONING ELECTRONICS: PHASE OFFSETS AND RELATIVE TIME DELAYS

| Phase response	Linear fit: $y = -ax + b$		Linear fit correlation, R^2
	Phase offset, b, rad	Relative time delay, a, s	
Dynamic force	−3.146	6.694×10⁻⁶	0.9993
Flux density	−1.571	−5.950×10⁻⁶	0.9990
Static force	−8.141×10⁻⁴	6.026×10⁻⁵	1.0000
Strain	−4.159×10⁻⁵	9.965×10⁻⁶	1.0000
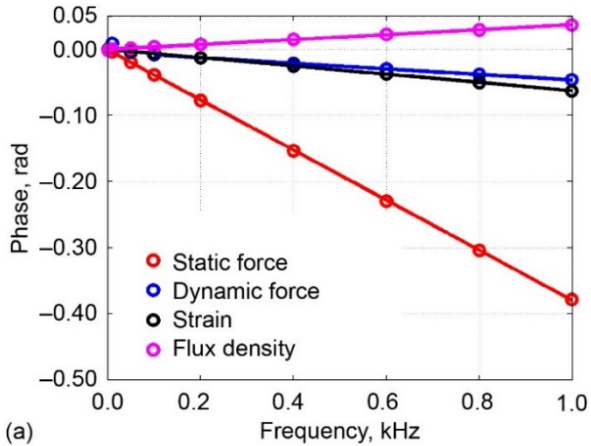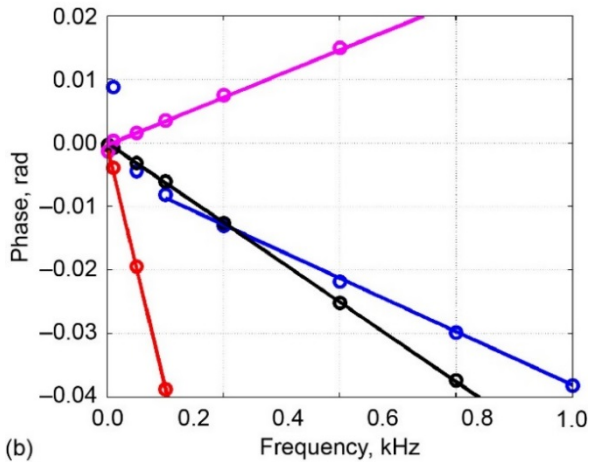
Figure 37.—Phase response of strain, static force, dynamic force, and magnetic flux density measurement channels relative to magnetic field channel (phase offset in dynamic force and flux density channels was removed for visualization purposes).


Figure 38.—Filtering of actuation responses. (a) Discrete Fourier transform of unfiltered actuation response of solid Galfenol rod for mean bias stress of −10.23 MPa. (b) Comparison of filtered and unfiltered magnetostriction responses at −10.23 MPa.

A DFT of the magnetic flux density and strain actuation responses is shown in Figure 38(a) for a representative bias stress (–10.23 MPa, or –1484 psi). The fundamental frequency is 0.1 Hz. For the measured actuation responses, a 10-Hz cutoff was chosen to preserve the appreciable harmonics and attenuate 60-Hz noise, which was present, but small in magnitude. The actuation strain responses exhibit more nonlinearity than the actuation flux density responses. Thus, to illustrate the effect of the filter, the filtered and unfiltered actuation strain (magnetostriction) responses are compared in Figure 38(b); the filtered magnetostriction response for the representative case retains the full nonlinearity of the unfiltered response.

Figure 39(a) presents a DFT of the quasi-static (1-Hz), major-hysteresis-loop sensing response measured at a constant current of 0.60 A. For quasi-static constant current responses, a 25-Hz low-pass cutoff frequency was selected, because it attenuated noise while preserving the integrity of the signals, as evidenced
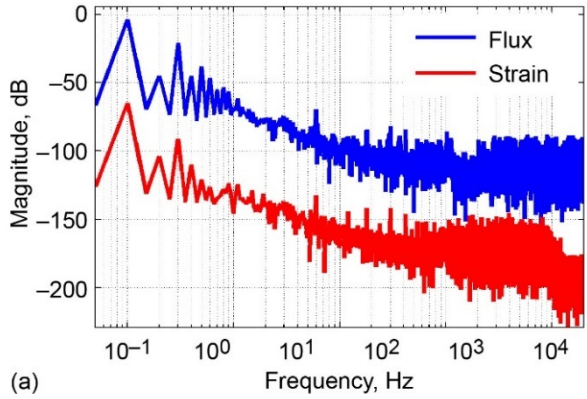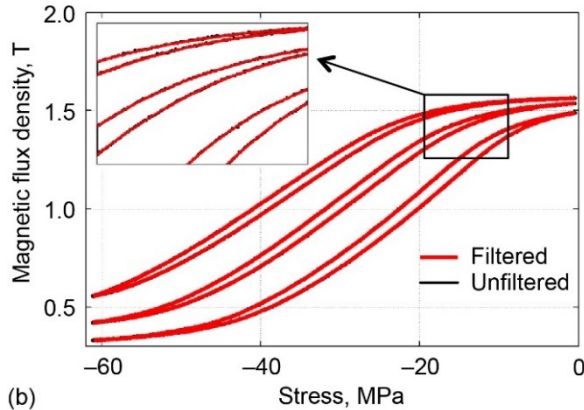
Figure 39.—Filtering of sensing responses measured under constant current. (a) Discrete Fourier transform of unfiltered sensing response of solid Galfenol rod for mean bias current of 0.60 A. (b) Comparison of filtered and unfiltered flux density responses at 0.50, 0.60, and 0.70 A.

Figure 40.—Filtering of sensing responses measured under constant magnetic field. (a) Discrete Fourier transform of unfiltered sensing response of solid Galfenol rod for mean bias field of 3.88 kA/m. (b) Comparison of filtered and unfiltered flux density responses at 2.41 and 3.88 kA/m.

by the comparison of filtered and unfiltered flux density responses in Figure 39(b). Flux density responses are shown rather than strain responses, because for sensing, the flux density responses are more nonlinear.

Since the quasi-static (1-Hz) sensing response for constant magnetic field is steeper and more nonlinear than for constant current, a larger number of harmonics are appreciable for constant-field responses. Thus, a higher low-pass cutoff frequency was required. A 40-Hz cutoff was found to be sufficient, as illustrated by the DFT and comparison of filtered and unfiltered flux density responses in Figure 40.

For dynamic sensing measurements, the forcing frequency was varied between 4 and 1000 Hz. In general, as frequency is increased, the sensing response becomes more linear due to an increase in eddy currents, which tend to suppress the active behavior of the material. DFTs of the dynamic major-loop responses indicate that low-pass filtering must preserve about 20 harmonics for forcing frequencies up to ~100 Hz, but only

5 to 10 harmonics for frequencies above that. Considering this result and the fact that a 10-kHz analog low-pass filter had already been used (see Figure 34), only measurements for forcing frequencies up to 50 Hz were digitally filtered (using a cutoff at the twentieth harmonic). Despite this, the signal-to-noise ratio of the unfiltered, high-frequency signals is sufficient, and the majority of the perceived variation in the responses is due to small variations in the force and current (or field) resulting from imperfect control of these variables.

6.4 Calculation of Material Properties

The constitutive behavior of magnetostrictive materials can be represented by the piezomagnetic equations

$$\vec{B} = \left[\mu^T\right]\vec{H} + \left[d^{*H}\right]\vec{T} \qquad (36)$$

$$\vec{S} = \left[d^T\right]\vec{H} + \left[s^H\right]\vec{T} \qquad (37)$$

where $\bar{B}, \bar{H}, \bar{S},$ and $\bar{T}$ are the magnetic flux density, magnetic field, strain, and stress vectors, respectively; $\left[d^{*H}\right]$ and $\left[d^{T}\right]$ are piezomagnetic coefficient matrices; $\left[s^{H}\right]$ is the compliance matrix; $\left[\mu^{T}\right]$ is the magnetic permeability matrix; and the superscripts H and T denote measurement at constant magnetic field and constant stress, respectively. In this work, excitation was applied axially (typically denoted as the 3 direction), and outputs were measured along the axial direction. For these conditions, Equations (36) and (37) become

$$B_3 = \mu_{33}^T H_3 + d^{*H}_{33} T_3 \qquad (38)$$

$$S_3 = d_{33}^T H_3 + s_{33}^H T_3 \qquad (39)$$

The quasi-static material properties are derived from the slope of B_3-versus-H_3 and S_3-versus-H_3 curves measured at constant stress, as well as the slope of B_3-versus-T_3 and S_3-versus-T_3 curves measured at constant field. To mitigate the noise amplification from numerical differentiation, small sections of each curve were fit by polynomials, which were analytically differentiated to calculate the slope at the center of each section (Refs. 18, 35, 38, and 39). Fourth-order polynomials were used in this work. A 75 percent overlap of adjacent sections was used to ensure smooth material property curves. The Young's modulus E^H was calculated as the inverse of the compliance s_{33}^H (the 33 component of the matrix $[s]^H$) (Ref. 39). Since constitutive responses were also measured at constant current to the electromagnets, the piezomagnetic coefficient and Young's modulus were also calculated at constant current: d^{*I}_{33} and E^I, respectively.

Under dynamic excitation, material properties are complex-valued quantities because of frequency-dependent hysteresis. Therefore, a frequency-domain method adapted from the standard ASTM D5992 (Ref. 7) was used to calculate the dynamic material properties. First, the measured strain and stress signals (S and T, respectively) were transformed to the frequency domain ($\tilde{S}$ and $\tilde{T}$, respectively) using DFTs. The complex, fundamental component (denoted by (1)) of each transformed signal, $\tilde{S}(1)$ and $\tilde{T}(1)$, was then extracted. Afterward, these fundamentals, which are linear, harmonic waveforms, were represented as phasors that differed in only magnitude and phase. The dynamic Young's modulus was then calculated using a vector relationship,

$$\tilde{E} = \tilde{T}(1)/\tilde{S}(1) \qquad (40)$$

The elastic component E of the dynamic modulus and the loss factor η_E were determined using the phase angle by which the stress leads the strain, $\delta_{T/S}$:

$$E = \mathrm{Re}(\tilde{E}) = \tilde{E}\cos(\delta_{T/S}) \qquad (41)$$

and

$$\eta_E = \mathrm{Im}(\tilde{E})/\mathrm{Re}(\tilde{E}) = \tan(\delta_{T/S}) \qquad (42)$$

The phase angle $\delta_{T/S}$ is simply the phase difference between the stress phasor and the strain phasor. Equations (40) to (42) are analogous to those presented in Reference 7 for the calculation of the elastic component and loss factor of the dynamic stiffness. The calculation procedure is illustrated in Figure 41. In an analogous manner, the lossless component d^{*}_{33} of the dynamic piezomagnetic coefficient $\tilde{d}^{*}_{33}$ and the associated loss factor η_{d^*} were determined using the phase angle by which the stress leads the magnetic flux density $\delta_{T/B}$,

$$d^{*}_{33} = \tilde{d}^{*}_{33}\cos(\delta_{T/B}) \qquad (43)$$

and

$$\eta_{d^*} = \tan(\delta_{T/B}) \qquad (44)$$

where

$$\tilde{d}^{*}_{33} = \tilde{B}(1)/\tilde{T}(1) \qquad (45)$$

Although this method neglects the harmonics of each signal, the areas of the hysteresis loops formed by the fundamentals and by the raw signals are equal (Ref. 7). Thus, the hysteresis loss per cycle in the B_3-versus-T_3 and S_3-versus-T_3 responses—W_{B-T} and W_{S-T}, respectively—can be accurately calculated as

$$W_{B-T} = \pi\tilde{T}\tilde{B}\sin(\delta_{T/B}) \qquad (46)$$

and

$$W_{S-T} = \pi\tilde{T}\tilde{S}\sin(\delta_{T/S}) \qquad (47)$$

In the present work, loss is only reported using the metrics of Equations (42) and (44).
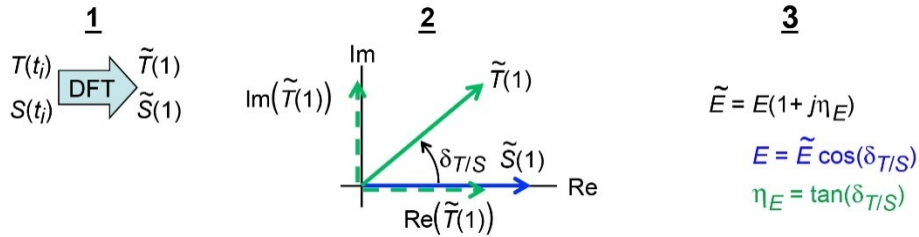
Figure 41.—Frequency-domain method used to calculate dynamic material properties at each forcing frequency (adapted from Ref. 7). Stress signal T and strain signal S are transformed via discrete Fourier transform (DFT) to frequency domain, from which fundamental components $\tilde{T}(1)$ and $\tilde{S}(1)$, respectively, are extracted. $\delta T/S$ is phase angle by which stress leads strain; $\tilde{E}$ is dynamic Young's modulus; E is elastic component of dynamic Young's modulus; $j = \sqrt{-1}$; and η_E is loss factor associated with dynamic Young's modulus.

6.5 Evaluation of Reversibility in the Constitutive Response

According to prior measurements of Galfenol, the material shows a very high degree of kinematic reversibility (i.e., the order of application of stress and magnetic field does not matter) (Refs. 18 and 40). To provide confidence in the experimental setup and reported measurements, kinematic reversibility of the solid Galfenol rod was investigated. To enable this investigation, the actuation response of the solid rod was measured in addition to the sensing response. Reversibility was evaluated by comparing each actuation curve measured at a constant stress to discrete points obtained from all of the sensing curves measured at constant field. Actuation points were separately obtained from the upper and lower branches of the sensing curves, thereby generating a hysteretic set of actuation points to compare with each hysteretic actuation curve. For more details, see Reference 40.

7.0 Procedure

Prior to each set of experiments, all electronics were allowed to warm up for at least 1 h. For all experiments, the applied load was controlled using PI control. Below, the procedure used to obtain the reported measurements is listed separately for each testing group.

Quasi-Static Actuation
1. Set up the experiment as shown in Figure 23(a).
2. Tune the load control gains while magnetically actuating the specimen and attempting to hold the load constant.
3. Zero the strain signal according to Section 5.6, if needed.
4. Reset the fluxmeter integrator as discussed in Section 5.6, if needed.
5. Apply a 0-A current.
6. Apply the bias force.
7. Apply the low-frequency, alternating current (AC).

8. Record the amplitude-scaled signals (Sec. 6.1) for 20 s.
9. Stop the AC current.
10. Repeat steps 3 to 9 for the remaining bias forces.
11. Shift the strain and flux density signals as discussed in Section 5.6 to yield the true strain and flux density.
12. Digitally filter the measured signals according to Section 6.3.
13. Calculate the stress in the rod from the force using Equation (14).
14. Calculate the actuation-based material properties as discussed in Section 6.4.
15. Save the manipulated signals and plot the results.

Quasi-static Sensing
1. Set up the experiment as shown in Figure 23(a).
2. Tune the load control gains to achieve a slightly overdamped response to a 1-Hz square wave command signal.
3. Zero the strain signal according to Section 5.6, if needed.
4. Reset the fluxmeter integrator as discussed in Section 5.6, if needed.
5. Apply the bias current (or field).
6. Apply the bias force. For a given bias current (or field), start with the major loop then proceed to its corresponding minor loops.
7. Apply the low-frequency, dynamic force.
8. Record the amplitude-scaled signals (Sec. 6.1) for 2 s (major-loop responses) or 1 s (minor-loop responses).
9. Stop the dynamic force.
10. Repeat steps 3 to 9 for the next bias force.
11. Repeat steps 3 to 10 for the remaining bias currents (or fields).
12. Shift the strain and flux density signals as discussed in Section 5.6 to yield the true strain and flux density.
13. Digitally filter the measured signals according to Section 6.3.

14. Calculate the stress in the rod from the force using Equation (14).
15. Calculate the sensing-based material properties as discussed in Section 6.4.
16. Save the manipulated signals and plot the results.

Dynamic Sensing
1. Set up the experiment as shown in Figure 23(b).
2. Tune the load-control gains to achieve a fully overdamped response to a 1-Hz square-wave command signal.
3. Zero the strain signal according to Section 5.6, if needed.
4. Reset the fluxmeter integrator as discussed in Section 5.6, if needed.
5. Apply the bias current (or field).
6. Apply the bias force.
7. Apply the high-frequency, dynamic force.
8. Activate an amplitude-phase compensator (APC) for the load control, allow it to stabilize, then pause the APC.
9. Record the amplitude-scaled signals (Sec. 6.1) for 2 s.
10. Stop the dynamic force.
11. Repeat steps 3 to 10 for the next forcing frequency or loading type.
12. Shift the strain and flux density signals as discussed in Section 5.6 to yield the true strain and flux density.
13. Phase align the signals as discussed in Section 6.2.

14. Digitally filter the measured signals according to Section 6.3.
15. Calculate the stress in the rod from the force using Equation (14).
16. Calculate the sensing-based material properties as discussed in Section 6.4.
17. Save the manipulated signals and plot the results.

Table XI is a matrix of the nominal testing conditions for each measurement. Exact bias conditions are stated in Sections 8.0 and 9.0. The stress range in this experiment was approximately –63 to 0 MPa (–9137 to 0 psi). For major loops, it was desired to excite the Galfenol specimen over this entire range while ensuring that compression of the specimen was maintained. Consequently, a stress bias of –31.9 MPa (–4627 psi) and amplitude of 31.4 MPa (4554 psi) were chosen for major loops. For the dynamic minor loops, the bias conditions were those for which the quasi-static magnetomechanical coupling of the solid rod was maximized (i.e., maximum sensitivity and minimum elastic modulus). To allow for a comparison of dynamic major and minor loops, dynamic major loops were measured at the same bias current and field used for dynamic minor loops. An extra group of dynamic major loops was measured at a high constant current to compare with dynamic major loops at a low current; this allowed for the effect of forcing frequency on positive and negative saturation to be determined.

TABLE XI.—MATRIX OF TESTING CONDITIONS FOR ACTUATION, QUASI-STATIC SENSING, AND DYNAMIC SENSING EXPERIMENTS

Testing group	Rod type	Loading type		Load (stress), N (MPa)		Frequency, Hz	Current, A	Field, kA/m
		Magnetic	Mechanical	Static	Dynamic			
Actuation	Solid	Major loop	Constant force	(a)	---	0.1	(b)	---
Quasi-static	Solid	Constant current	Major loop	–985 (–31.9)	970 (31.4)	1	(d)	---
			Minor loop	(c)	89 (2.88)	4		
		Constant field	Major loop	–985 (–31.9)	970 (31.4)	1	---	(e)
			Minor loop	(c)	89 (2.88)	4		
	Laminated	Constant current	Major loop	–985 (–31.9)	970 (31.4)	1	(d)	---
Dynamic	Solid	Constant current	Major loop	–985 (–31.9)	970 (31.4)	4, 10, 20, 30, 40, 50, 60, 70, 80, 90, 100, 200, 300, 400, 500, 600, 700, 800, 900, and 1000	0.3	---
							0.8	
			Minor loop	–307 (–9.93)	89 (2.88)		0.3	
		Constant field	Major loop	–985 (–31.9)	970 (31.4)		---	2.5
			Minor loop	–246 (–7.96)	89 (2.88)			
	Laminated	Constant current	Major loop	–985 (–31.9)	970 (31.4)		0.3	---
			Minor loop	–307 (–9.93)	89 (2.88)			

[a]0, –50, –317, –633, –950, –1267, –1584, and –1900 N (0, –1.62, –10.3, –20.5, –30.7, –40.9, –51.2, and –61.5 MPa).
[b]1.5-A amplitude.
[c]–177, –399, –621, –842, –1064, and –1286 N (–5.73, –12.9, –20.1, –27.2, –34.4, and –41.6 MPa).
[d]0, 0.1, 0.2, 0.3, 0.4, 0.5, 0.6, 0.7, 0.8, 0.9, and 1 A.
[e]0, 0.8, 1.5, 2.5, 4, 5.6, 7.3, 9, 10.7, 12.4, and 14 kA/m (the approximate fields at zero stress for each of the constant current levels).

8.0 Quasi-Static Results

To verify the experimental setup with existing data, quasi-static actuation and sensing responses were first measured. Since the constitutive behavior of Galfenol ($Fe_{100-x}Ga_x$) is highly dependent on gallium concentration, processing conditions, and material texture, measurements are only compared with available data for the same or very similar Galfenol materials (i.e., specimens with x ≈ 18.4 at.% and a strong <100> texture). The quasi-static behavior is also the foundation from which the dynamic behavior deviates because of frequency-dependent effects; consequently, the quasi-static response can also be used to compare with the dynamic response.

8.1 Actuation Response

The filtered actuation responses of the solid Galfenol rod are given in Figure 42. The magnetic-field-versus-current responses in Figure 42(a) show a nearly linear relationship. Figure 42(b) presents the variation in stress about the bias as a function of field. Clearly, the load frame could not hold the compressive force constant; however, stress variation is typically less than 0.13 MPa (19 psi) about the mean stress. The stress variation at the 0.00 MPa bias is significantly smaller than for the other bias stresses because the load frame's piston was disengaged from the specimen for this bias stress. Figure 42(c) depicts the actuation strain (magnetostriction) responses. Because of the magnitude and polarity of the stress variation, the measured magnetostriction at negative saturation is about 2.8×10^{-6} m/m lower than that at positive saturation. The saturation magnetostriction (λ_{sat}) of the solid, polycrystalline $Fe_{81.6}Ga_{18.4}$ rod is 237×10^{-6} m/m (average of the value at positive and negative saturation). Figure 42(d) shows the flux density actuation responses, which exhibit the expected trends. As shown in Table XII, the saturation magnetostriction is similar to published measurements. Table XII also compares the saturation elastic modulus and saturation flux density of the solid and laminated rods, which are derived from sensing measurements that are presented in the following two sections.
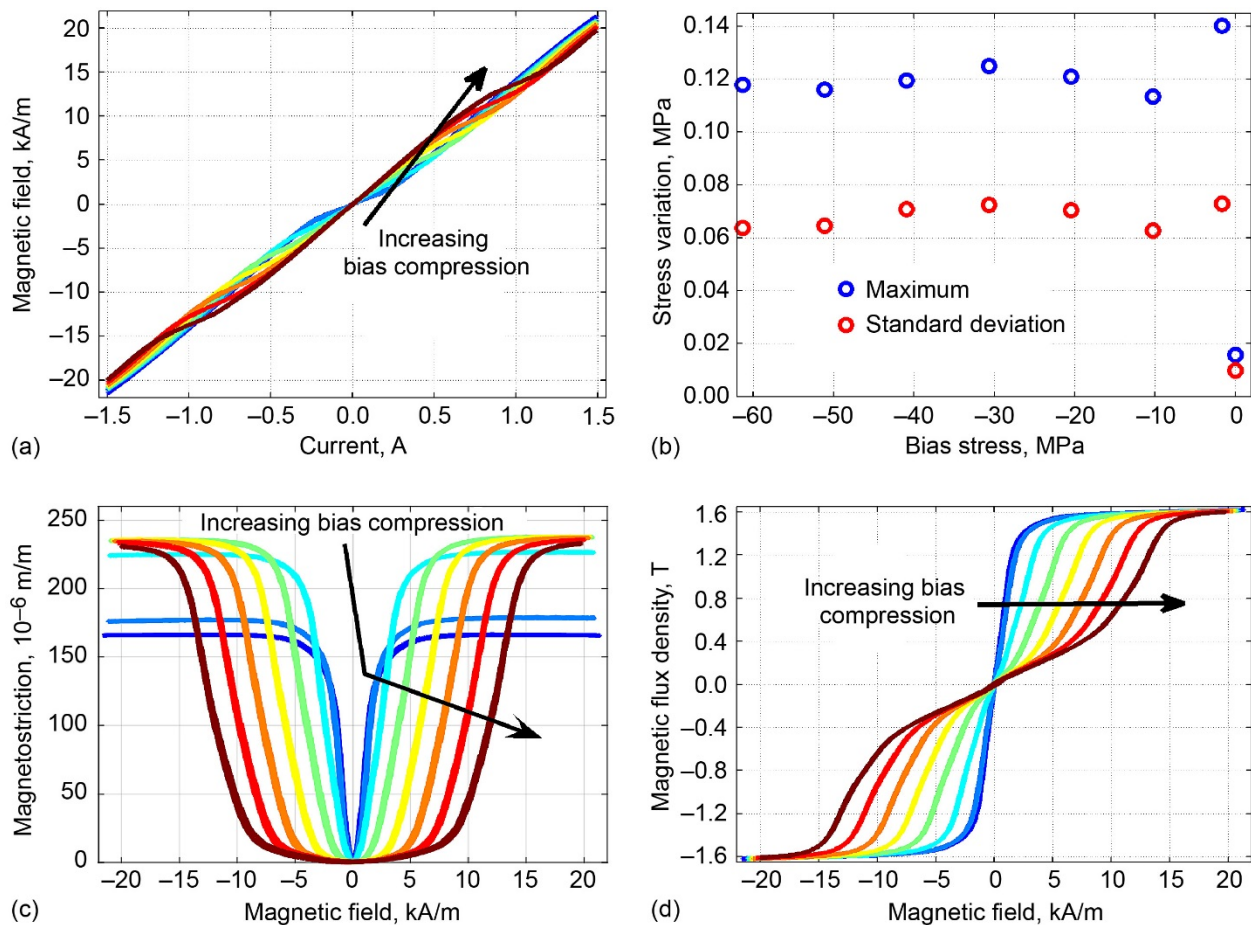

Figure 42.—Actuation response of solid Galfenol rod for mean bias stresses of 0.00, −1.64, −10.23, −20.44, −30.65, −40.88, −51.10, and −61.31 MPa. Color changes from blue to red as bias compression increases. (a) Magnetic field versus drive current. (b) Maximum and standard deviation of variation in stress about bias stress versus bias stress. (c) Actuation strain versus field. (d) Flux density versus field.

TABLE XII.—COMPARISON OF MEASURED CONSTITUTIVE PROPERTIES OF GALFENOL RODS
WITH PUBLISHED RESULTS; GALFENOL SPECIMENS ARE POLYCRYSTALLINE UNLESS SPECIFIED

Reference	Galfenol specimen[a]	Saturation magnetostriction, λ_{sat} ($\times 10^{-6}$ m/m)	Saturation elastic modulus, E_{sat}, GPa	Saturation flux density, B_{sat}, T
This report	$Fe_{81.6}Ga_{18.4}$, research grade, solid	237	72.2	1.60
	$Fe_{81.6}Ga_{18.4}$, research grade, laminated	--------	59.6	1.57
Ref. 41	$Fe_{81.6}Ga_{18.4}$, research grade	220±25	72.4	1.5
	$Fe_{81.6}Ga_{18.4}$, production grade	168±18	86.3	1.5
Ref. 42	$Fe_{81.6}Ga_{18.4}$, research grade	266	76.5	1.55
	$Fe_{81.6}Ga_{18.4}$, production grade	165	98	1.60
Ref. 35	$Fe_{81.6}Ga_{18.4}$, research grade	--------	76±3	-----
Ref. 40	$Fe_{81.5}Ga_{18.5}$, research grade	255	75	1.55
Ref. 43	$Fe_{82}Ga_{18}$, production grade	230	-------	1.6
Ref. 44	$Fe_{81}Ga_{19}$, single crystal	~300	59	1.66

[a]The crystal growth rate for production-grade specimens (~350 mm/h) is about an order of magnitude faster than for research-grade crystals (~25 mm/h), which are grown about an order of magnitude faster than rates used to produce single crystals (~2 to 4 mm/h) (Ref. 42).
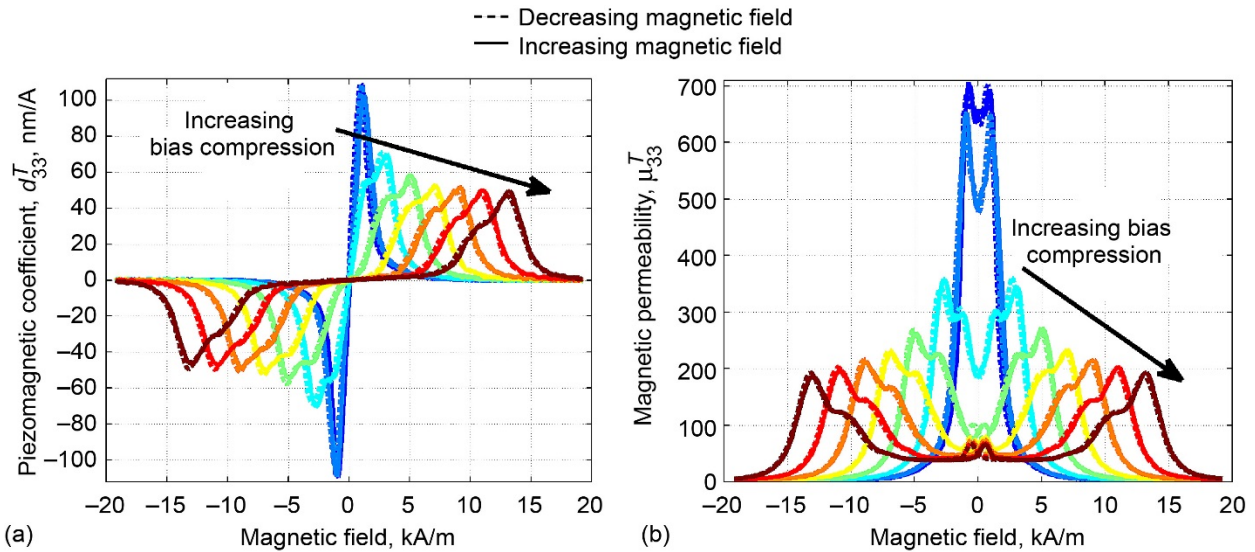

Figure 43.—Actuation-based material properties (from major loops) of solid Galfenol rod for mean bias stresses of 0.00, −1.64, −10.23, −20.44, −30.65, −40.88, −51.10, and −61.31 MPa. Color changes from blue to red as bias compression increases. (a) Piezomagnetic coefficient versus field. (b) Relative magnetic permeability versus field.

Actuation-based material properties μ_{33}^T and d_{33}^T were calculated by fitting fourth-order polynomials to 0.5-kA/m-wide sections of the curves in Figure 42. To account for hysteresis, the half of each curve where magnetic field is increasing was fit separately from the half where the field is decreasing. Consequently, the hysteresis in the material properties was captured. The results are shown in Figure 43.

8.2 Sensing Response

This section presents the quasi-static sensing responses of the solid and laminated Galfenol rods.

8.2.1 Constant Current

Figure 44 and Figure 45 depict the major- and minor-loop sensing responses, respectively, of the solid Galfenol rod for bias currents of 0.00 to 1.00 A. Figure 44(a) and Figure 45(a) illustrate the variation in current about the bias as a function of stress. The performance of the Kepco amplifier's internal current control system is highlighted by the very small variation in the bias current during stress cycling (typically <±20 µA). Despite the successful current control, the magnetic field in the specimen, shown in Figure 44(b) and Figure 45(b), fluctuates because of the material's stress- and magnetic-field-dependent magnetic permeability (Ref. 36). The increase of the magnetic field with compressive stress partially counteracts the effect of

the compression, leading to shallower sensing responses compared to the constant magnetic field responses (see Sec. 8.2.2). This effect motivates the need for measuring the sensing response under constant magnetic field and constant current conditions. The elastic response is depicted in Figure 44(c) and Figure 45(c), where the active (soft) and passive (hard) regimes are separated by an elbow in the responses. From the flux-density-versus-stress responses in

Figure 44(d) and Figure 45(d), the saturation magnetic flux density B_{sat} can be identified as ~1.60 T (~16 kG).

The major-loop behavior bounds the material's response to smaller amplitude stress inputs (i.e., all possible minor-loop responses) for a given magnetic bias and forcing frequency. The comparison of the major and minor sensing loops in Figure 46 shows that the measurements accurately capture this aspect of the constitutive behavior.
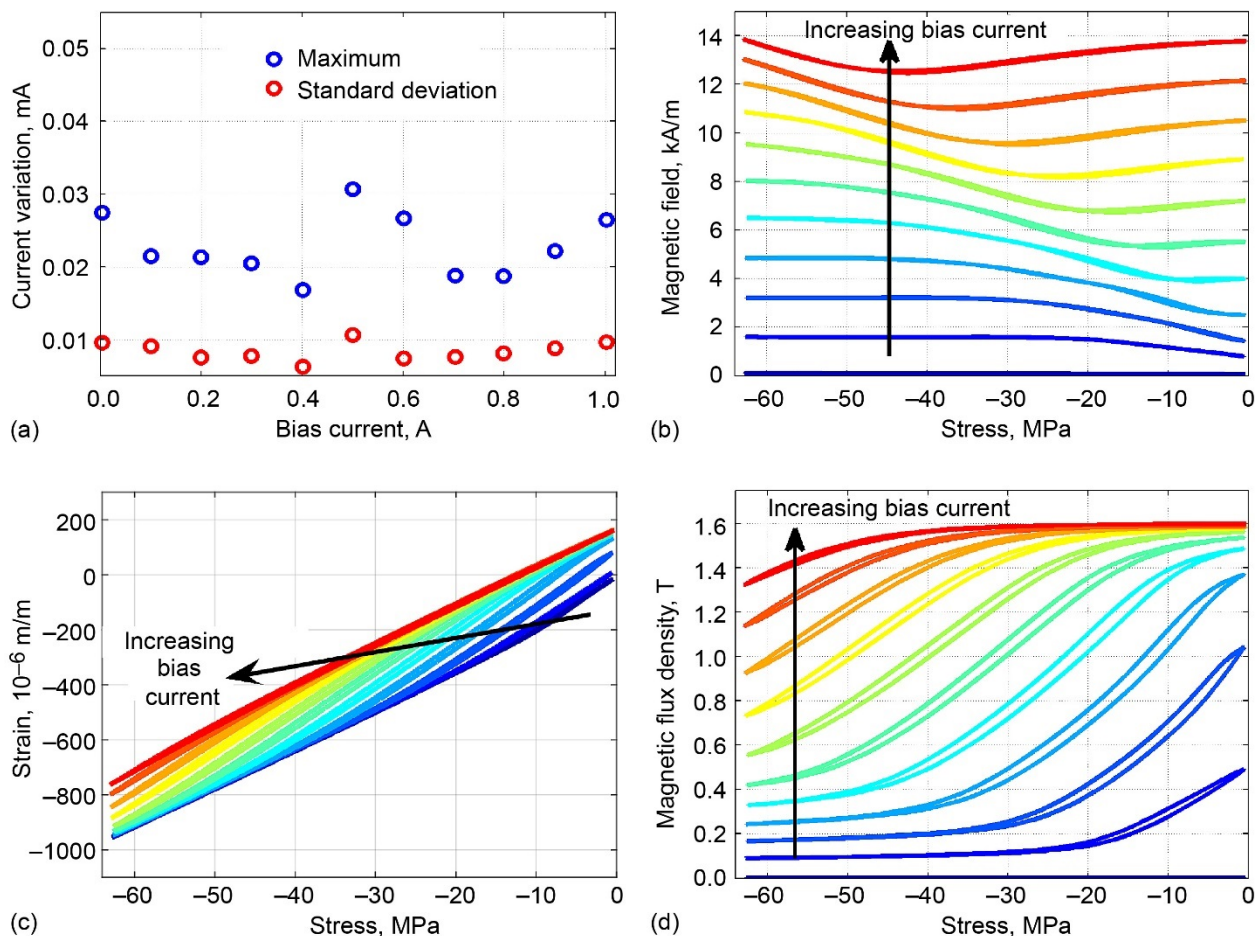

Figure 44.—Major loop sensing response of solid Galfenol rod for bias stress of −31.9 MPa and mean bias currents of 0.00 to 1.00 A in increments of 0.10 A. Color changes from blue to red as bias current increases. (a) Maximum and standard deviation of current variation about bias current versus bias current. (b) Magnetic field versus stress. (c) Strain versus stress. (d) Magnetic flux density versus stress.
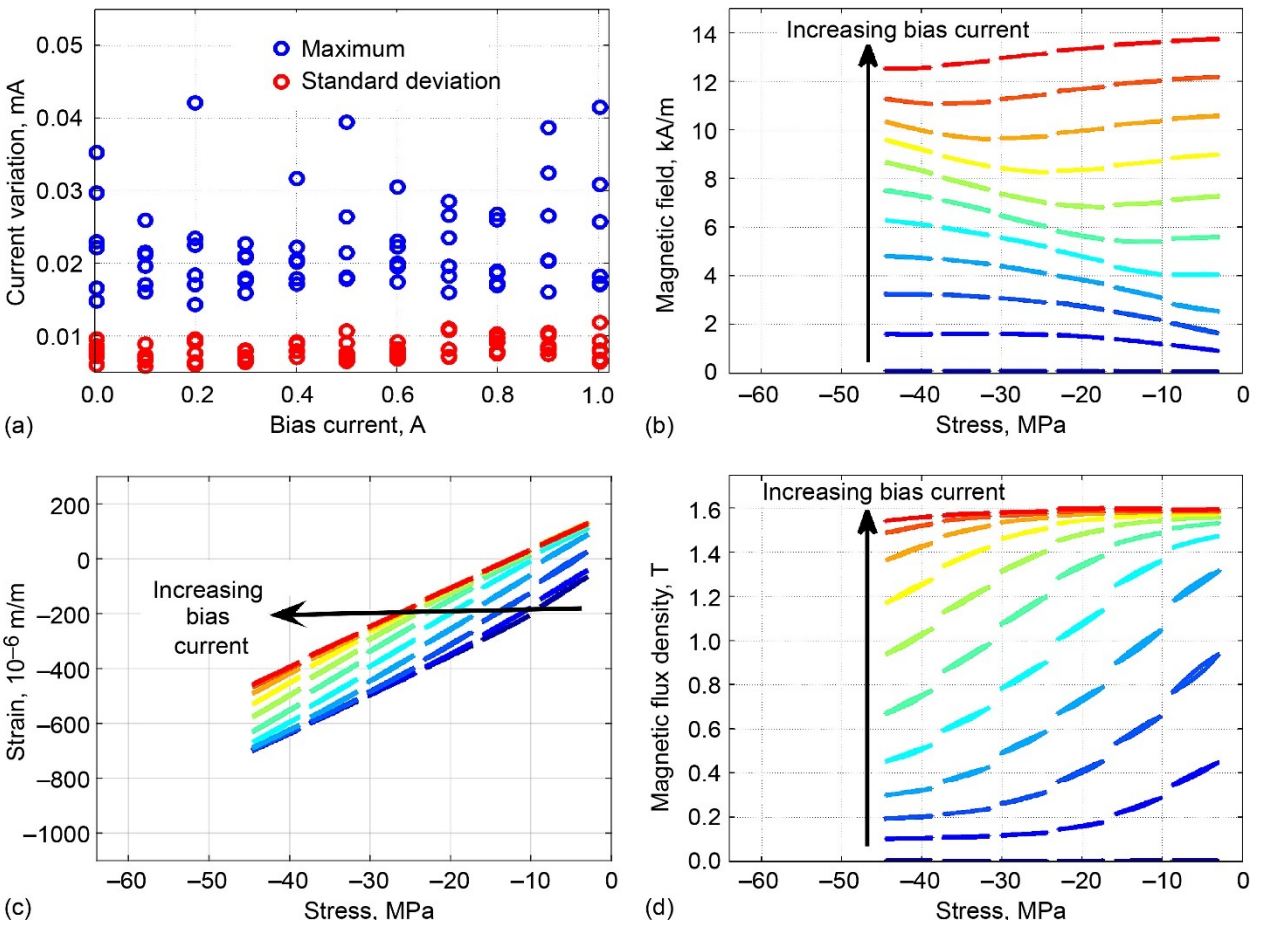
Figure 45.—Minor loop sensing response of solid Galfenol rod for mean bias currents of 0.00 to 1.00 A in increments of 0.10 A and nominal bias stresses of –5.59, –12.6, –19.6, –26.6, –33.6, and –40.6 MPa. Color changes from blue to red as bias current increases. (a) Maximum and standard deviation of current variation about bias current versus bias current. (b) Magnetic field versus stress. (c) Strain versus stress. (d) Magnetic flux density versus stress.
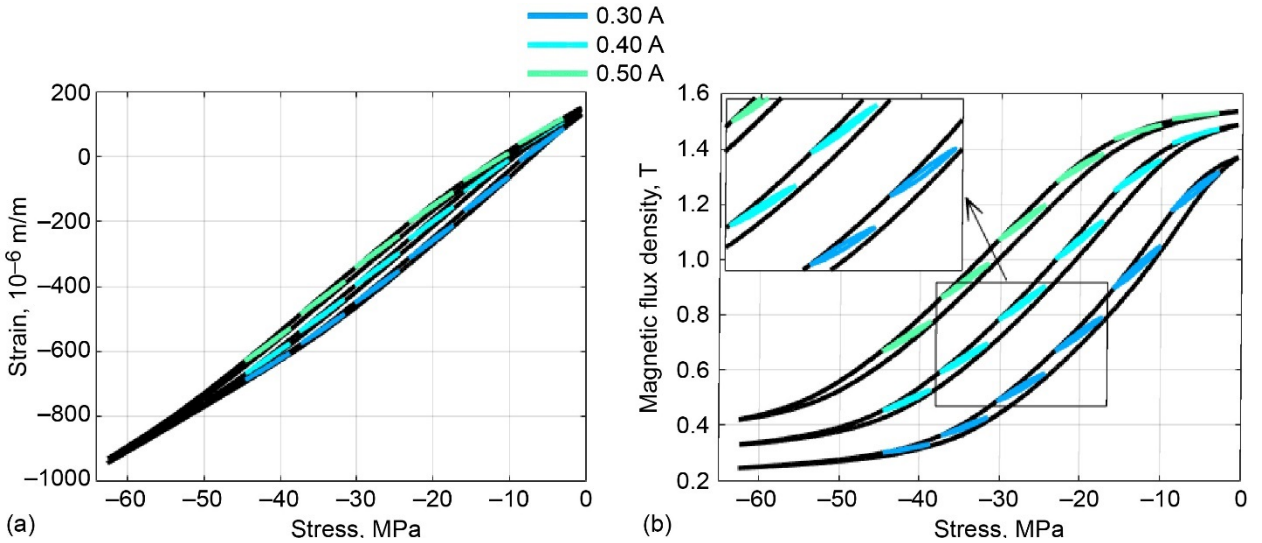

Figure 46.—Comparison of major and minor sensing response of solid Galfenol rod for mean bias currents of 0.30, 0.40, and 0.50 A. (a) Strain versus stress. (b) Magnetic flux density versus stress.

Sensing-based material properties E^I and d^{*I}_{33} were calculated by fitting fourth-order polynomials to 0.75-MPa-wide sections of the major loops in Figure 44. The half of each curve where stress is increasing was fit separately from the half where stress is decreasing. Figure 47 gives the results. The saturation elastic modulus E_{sat} is ~72.2 GPa (10.5×10⁶ psi), which was calculated at high compression when stress was decreasing. Table XII compares the saturation modulus and flux density measurements with those from prior work. The elastic modulus tends to increase above the saturation value after the stress changes direction, particularly near zero stress. The cause was not investigated, although it may be due in part to having a stress reversal point before complete magnetic saturation. Noise prevented the calculation of material properties near reversal points in (Ref. 38). However, noise is not believed to be the cause here.

Material properties were also calculated from minor loops by fitting each loop with a fourth-order polynomial; Figure 48 presents the results. A comparison of Figure 47 and Figure 48 reveals that the major-loop sensing responses are steeper than the minor loops at the same loading state. This suggests that magnetic domain wall bending dominates the magnetization process for low signal operation. Similar findings have been published for Galfenol (Ref. 18) and Terfenol-D (Ref. 45).
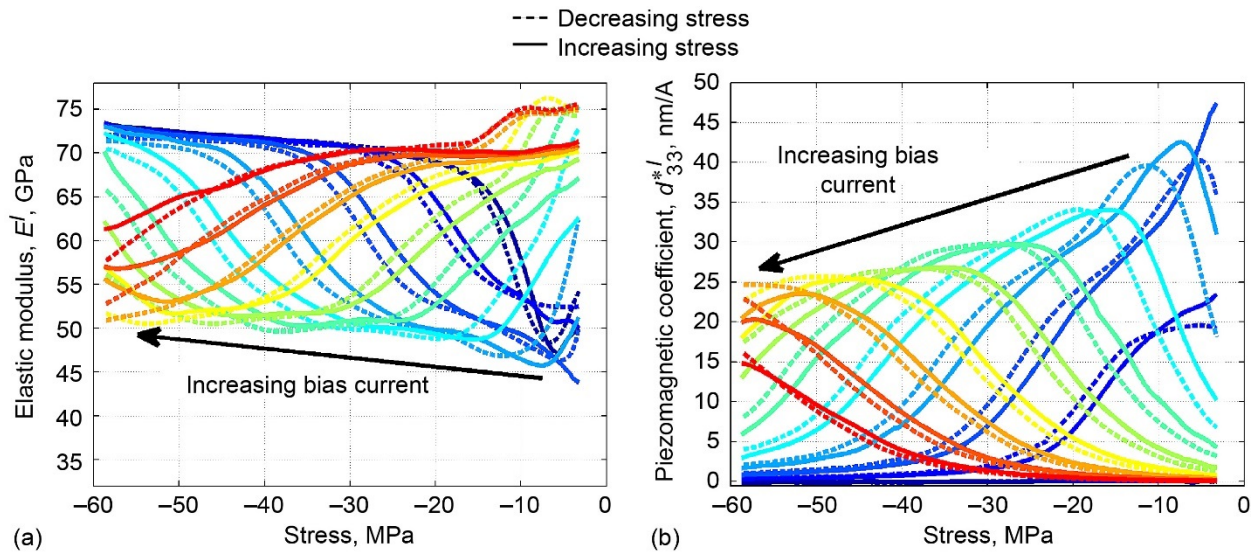

Figure 47.—Sensing-based material properties (from major loops) of solid Galfenol rod for bias stress of –31.9 MPa and mean bias currents of 0.00 to 1.00 A in increments of 0.10 A. Color changes from blue to red as the bias current increases. (a) Elastic modulus versus stress. (b) Piezomagnetic coefficient versus stress.
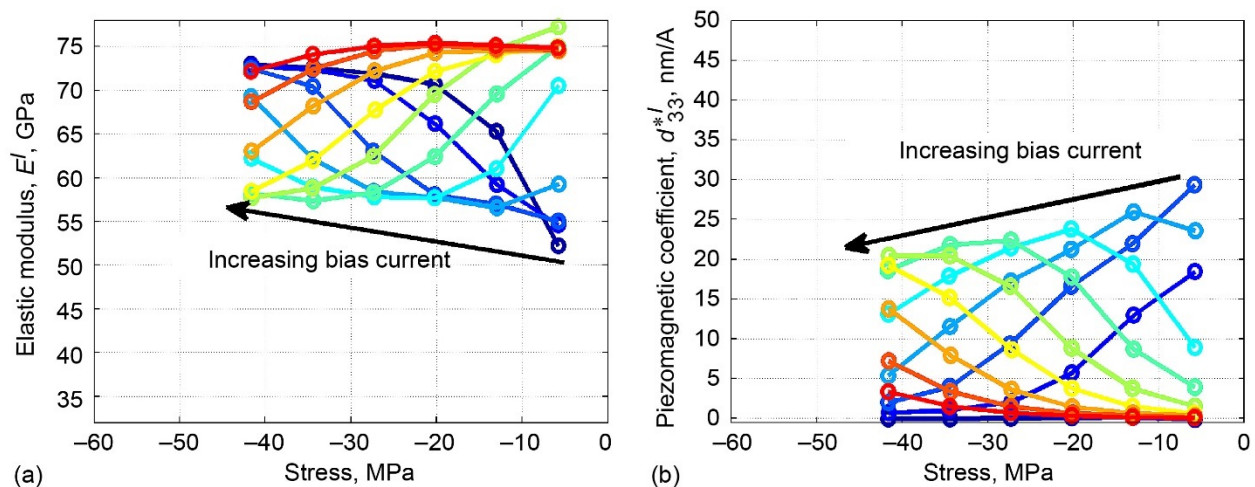

Figure 48.—Sensing-based material properties (from minor loops) of solid Galfenol rod for mean bias currents of 0.00 to 1.00 A in increments of 0.10 A and nominal bias stresses of –5.73, –12.9, –20.1, –27.2, –34.4, and –41.6 MPa. Color changes from blue to red as bias current increases. (a) Elastic modulus versus stress. (b) Piezomagnetic coefficient versus stress.
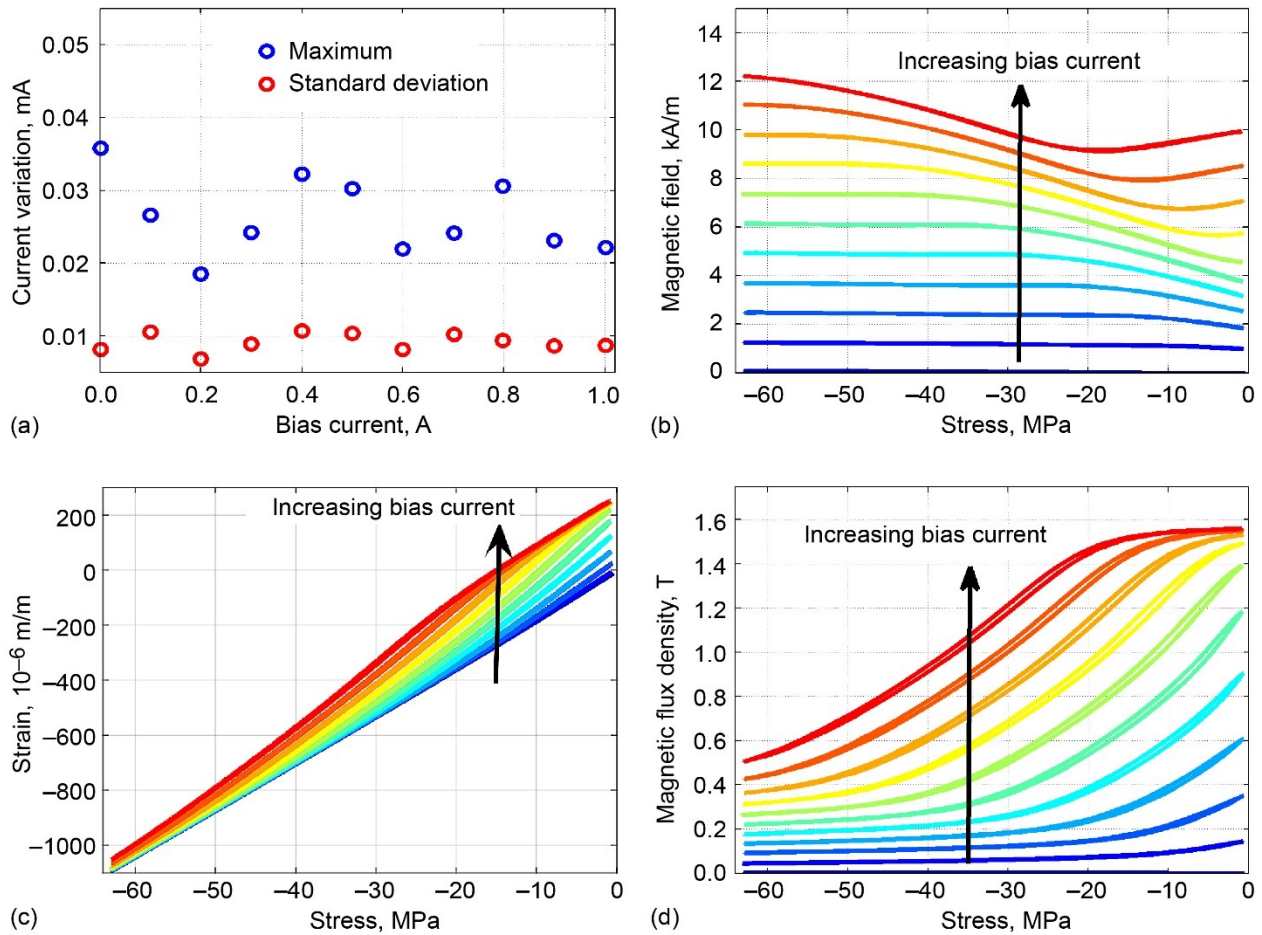
Figure 49.—Major-loop sensing response of laminated Galfenol rod for bias stress of −31.9 MPa and mean bias currents of 0.00 to 1.00 A in increments of 0.10 A. Color changes from blue to red as bias current increases. (a) Maximum and standard deviation of current variation about bias current versus bias current. (b) Magnetic field versus stress. (c) Strain versus stress. (d) Magnetic flux density versus stress.

To help analyze the dynamic responses of the laminated Galfenol rod, its quasi-static, major-loop sensing behavior was measured, as shown in Figure 49, for the same bias currents as used for the solid rod. The variation in current about the bias, depicted in Figure 49(a), is very similar to the variation in the solid rod. Figure 49(b) presents the change in field as a function of stress. The mechanical sensing responses are shown in Figure 49(c), whereas the magnetic sensing responses are given in Figure 49(d). Relative to the solid rod, the laminated rod has a slightly lower saturation flux density (~1.57 T, or ~15.7 kG) and a considerably lower saturation elastic modulus (59.6 GPa, or $8.6{\times}10^6$ psi), which is due in part to the presence of adhesive layers that have a modulus of only 0.862 GPa ($1.25{\times}10^5$ psi). The laminated rod is less responsive to increases in the magnetic field and slightly less responsive to stress changes. This is consistent with the reduction in saturation flux density and suggests that anisotropy is more pronounced in this specimen.

The sensing-based material properties of the laminated rod, given in Figure 50, were calculated using the same fitting parameters as used for the solid rod. Relative to the solid rod, modulus values are clearly smaller, and piezomagnetic coefficient values are similar. Observed trends are consistent with the solid rod's behavior. The elastic modulus increases above the saturation value at the high compression reversal point; this behavior is similar to that seen in the solid rod.

8.2.2 Constant Magnetic Field

The major- and minor-loop behaviors are presented in Figure 51 and Figure 52, respectively. The change in current required to hold the field constant is shown in Figure 51(a) and Figure 52(a). The variation in the field about the bias field is depicted in Figure 51(b) and Figure 52(b). For quasi-static changes in stress, the magnetic field is typically held within ±0.0125 and ±0.004 kA/m (±0.16 and ±0.05 Oe) of the bias field f or major and minor loops, respectively. Comparatively,
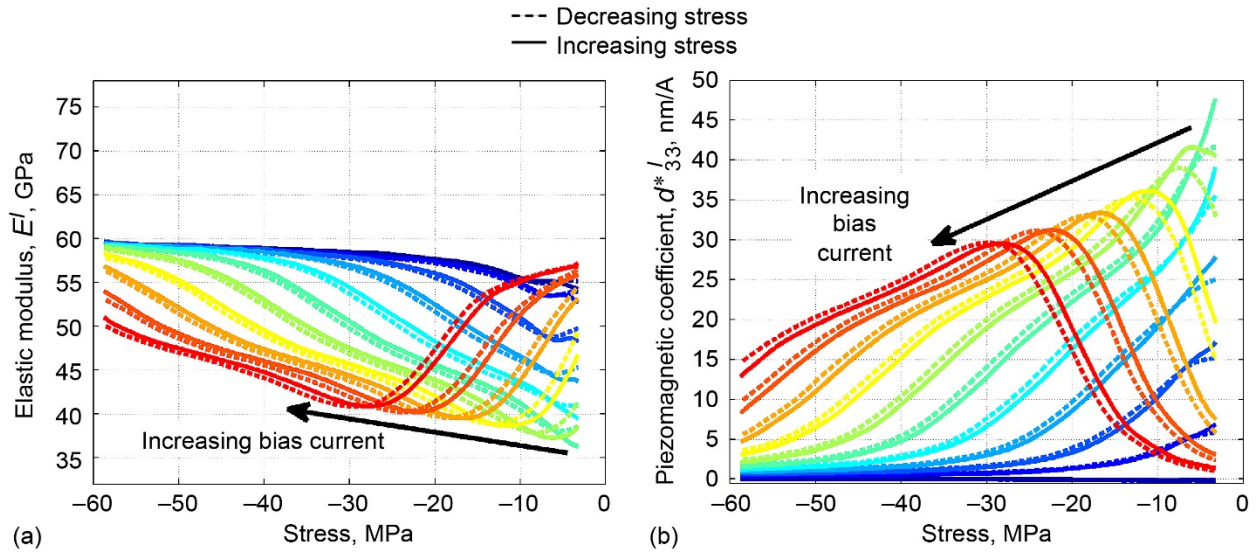
Figure 50.—Sensing-based material properties (from major loops) of laminated Galfenol rod for bias stress of −31.9 MPa and mean bias currents of 0.00 to 1.00 A in increments of 0.10 A. Color changes from blue to red as bias current increases. (a) Elastic modulus versus stress. (b) Piezomagnetic coefficient versus stress.
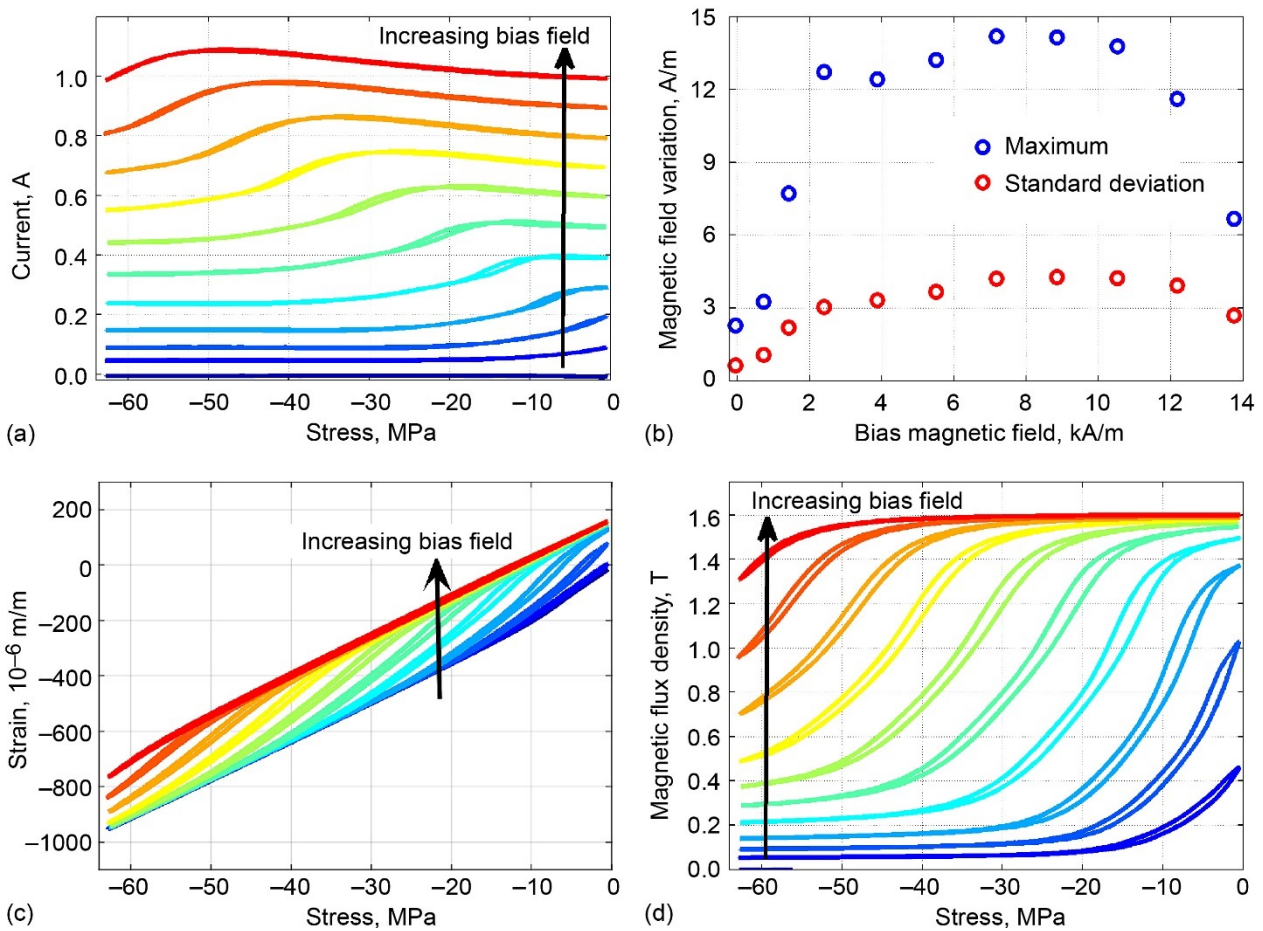
Figure 51.—Major loop sensing response of solid Galfenol rod for bias stress of −31.9 MPa and mean bias fields of −0.05, 0.73, 1.42, 2.41, 3.88, 5.50, 7.17, 8.84, 10.51, 12.19, and 13.76 kA/m. Color changes from blue to red as bias field increases. (a) Current versus stress. (b) Maximum and standard deviation of variation in magnetic field about bias field versus bias field. (c) Strain versus stress. (d) Magnetic flux density versus stress.
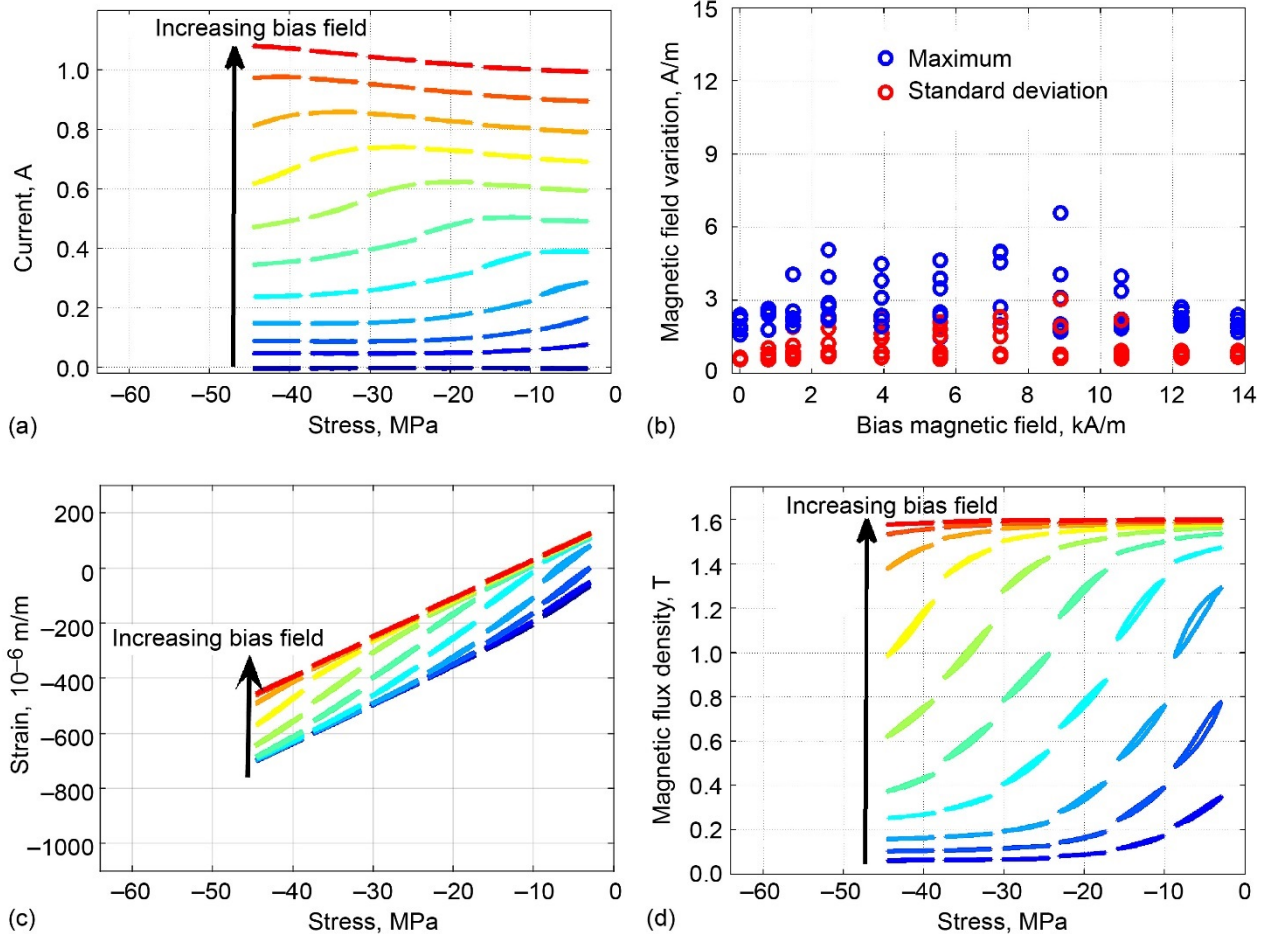
Figure 52.—Minor loop sensing response of solid Galfenol rod for mean bias fields of –0.05, 0.73, 1.42, 2.41, 3.88, 5.50, 7.17, 8.84, 10.51, 12.19, and 13.76 kA/m and nominal bias stresses of –5.73, –12.9, –20.1, –27.2, –34.4, and –41.6 MPa. (a) Current versus stress. (b) Maximum and standard deviation of variation in magnetic field about bias field versus bias field. (c) Strain versus stress. (d) Magnetic flux density versus stress; color changes from blue to red as bias field increases.

quasi-static constant field experiments by (Ref. 33) exhibited magnetic field variation of ±0.079 (typical) to ±0.79 kA/m (maximum) (±0.99 to ±9.9 Oe). The major- and minor-loop strain and flux density responses to stress are given in Figure 51(c) and Figure 52(c) and Figure 51(d) and Figure 52(d), respectively. As expected, the saturation magnetostriction, flux density, and elastic modulus are found to be the same as for the constant-current behavior.

A comparison between constant field minor and major loops is depicted in Figure 53. Minor loops are circumscribed by the major loops, which helps to verify the experimental setup and testing procedure.

Material properties calculated from the constant field, major- and minor-loop sensing responses of the solid rod are presented in Figure 54 and Figure 55, respectively. Minor loops are stiffer and less sensitive to stress than the major loops, but to a lesser extent than seen in the constant current results. This is due to

the increased ratio of the minor-loop stress amplitude to the stress range of the burst region.

8.3   Comparison of Actuation and Sensing Responses

Reversibility in the constitutive response of the solid Galfenol rod was evaluated as discussed in Section 6.5. The results are shown in Figure 56. Overall, the actuation points obtained from the sensing curves almost mirror the directly measured actuation response. This is consistent with prior work, thus providing confidence in the experimental setup and testing procedure. Interestingly, hysteresis appears slightly larger for the stress application than for the field application. This is consistent with the measurements and modeling presented in References 36 and 40, but contrasts with the highly reversible measurements shown in Reference 42.
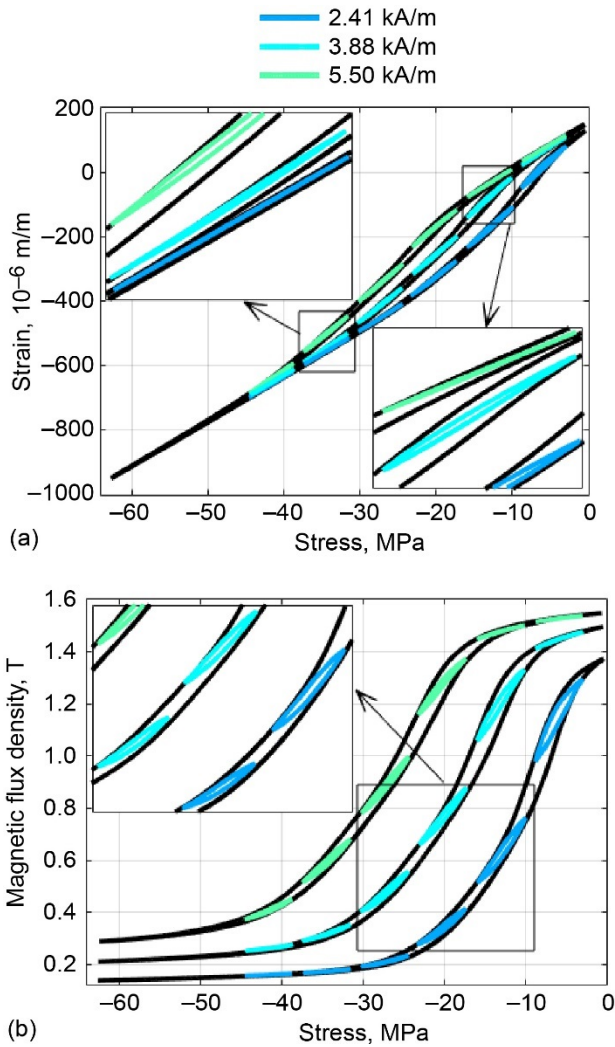
Figure 53.—Comparison of major and minor sensing response of solid Galfenol rod for mean bias fields of 2.41, 3.88, and 5.50 kA/m. (a) Strain versus stress. (b) Magnetic flux density versus stress.
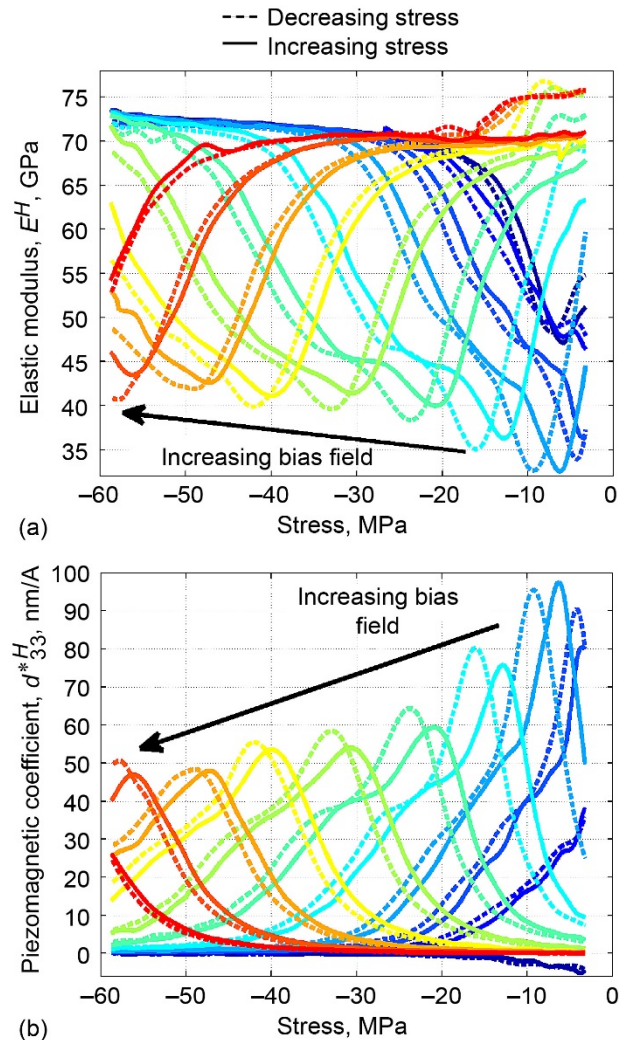
Figure 54.—Sensing-based material properties (from major loops) of solid Galfenol rod for bias stress of −31.9 MPa and mean bias fields of −0.05, 0.73, 1.42, 2.41, 3.88, 5.50, 7.17, 8.84, 10.51, 12.19, and 13.76 kA/m. Color changes from blue to red as bias field increases. (a) Elastic modulus versus stress. (b) Piezomagnetic coefficient versus stress.

(a)

(b)
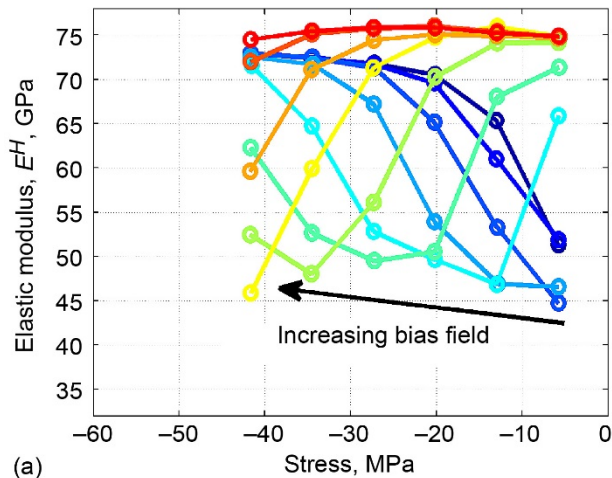
(a)
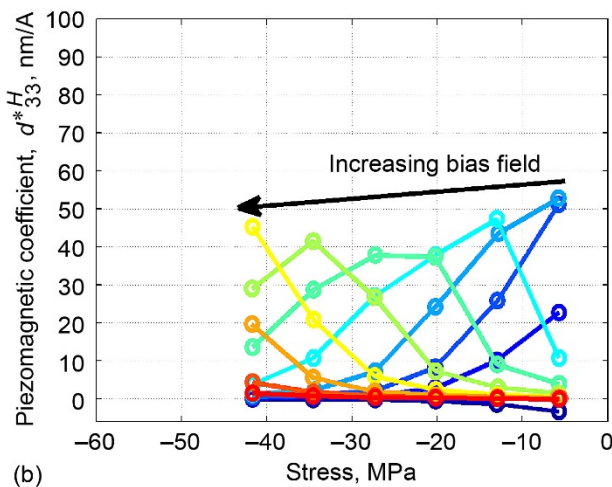
(b)

Figure 55.—Sensing-based material properties (from minor loops) of solid Galfenol rod for mean bias fields of –0.05, 0.73, 1.42, 2.41, 3.88, 5.50, 7.17, 8.84, 10.51, 12.19, and 13.76 kA/m and nominal bias stresses of –5.73, –12.9, –20.1, –27.2, –34.4, and –41.6 MPa. Color changes from blue to red as bias field increases. (a) Elastic modulus versus stress. (b) Piezomagnetic coefficient versus stress.

Figure 56.—Comparison of actuation response of solid Galfenol rod measured directly and obtained from sensing response at constant field. (a) Strain versus magnetic field. (b) Magnetic flux density versus magnetic field.

9.0 Dynamic Sensing Results

The selection of bias conditions for dynamic sensing measurements is discussed in Section 7.0. To improve the clarity of plotted results, only responses for forcing frequencies of 4, 10, 50, 100, 200, 400, 600, 800, and 1000 (or 975) Hz are shown. Data is plotted for the lesser of 50 forcing cycles or 2 s.

9.1 Solid Galfenol Rod

This section presents the dynamic sensing responses of the solid Galfenol rod.

9.1.1 Constant Current

The major-loop sensing responses at constant current are shown in Figure 57 and Figure 58 for bias currents of 0.30 and 0.80 A, respectively. The performance of the current control is shown by the current-versus-stress responses in Figure 57(a) and Figure 58(a). Two performance metrics—the maximum and standard deviation of the variation—were calculated at each forcing frequency and are presented in Figure 57(b) and Figure 58(b). For both bias currents, current variation increases nearly linearly with frequency, but remains below 14 mA for all cases. The strain curves in Figure 57(c) and Figure 58(c) are successively shifted along the strain axis starting with the 10-Hz curve to more clearly visualize the behavior. At 4 Hz, there is an elbow in the strain response where the magnetostriction saturates and the elastic modulus reaches its stiff or saturated value. For compressive stresses less than the

elbow stress, magnetostriction occurs and the effective elastic modulus of the material is reduced. As frequency increases, the elbow disappears and the region of softened behavior stiffens until it coincides with the saturated, purely elastic regime. Evident in the flux density-versus-stress plots in Figure 57(d) and Figure 58(d), hysteresis increases and sensitivity to stress decreases with frequency. These trends imply that at high frequency, magnetic moment rotation is severely inhibited in the solid Galfenol rod. Although the stress amplitude was not large enough to reach both positive and negative saturation in the same test (i.e., to measure full hysteresis loops), these saturation states were separately reached in Figure 57 and Figure 58. The results separately show that the flux density magnitude at positive and negative saturation is frequency independent, which suggests that the limits of full hysteresis loops (i.e., the saturation states) are also frequency independent.
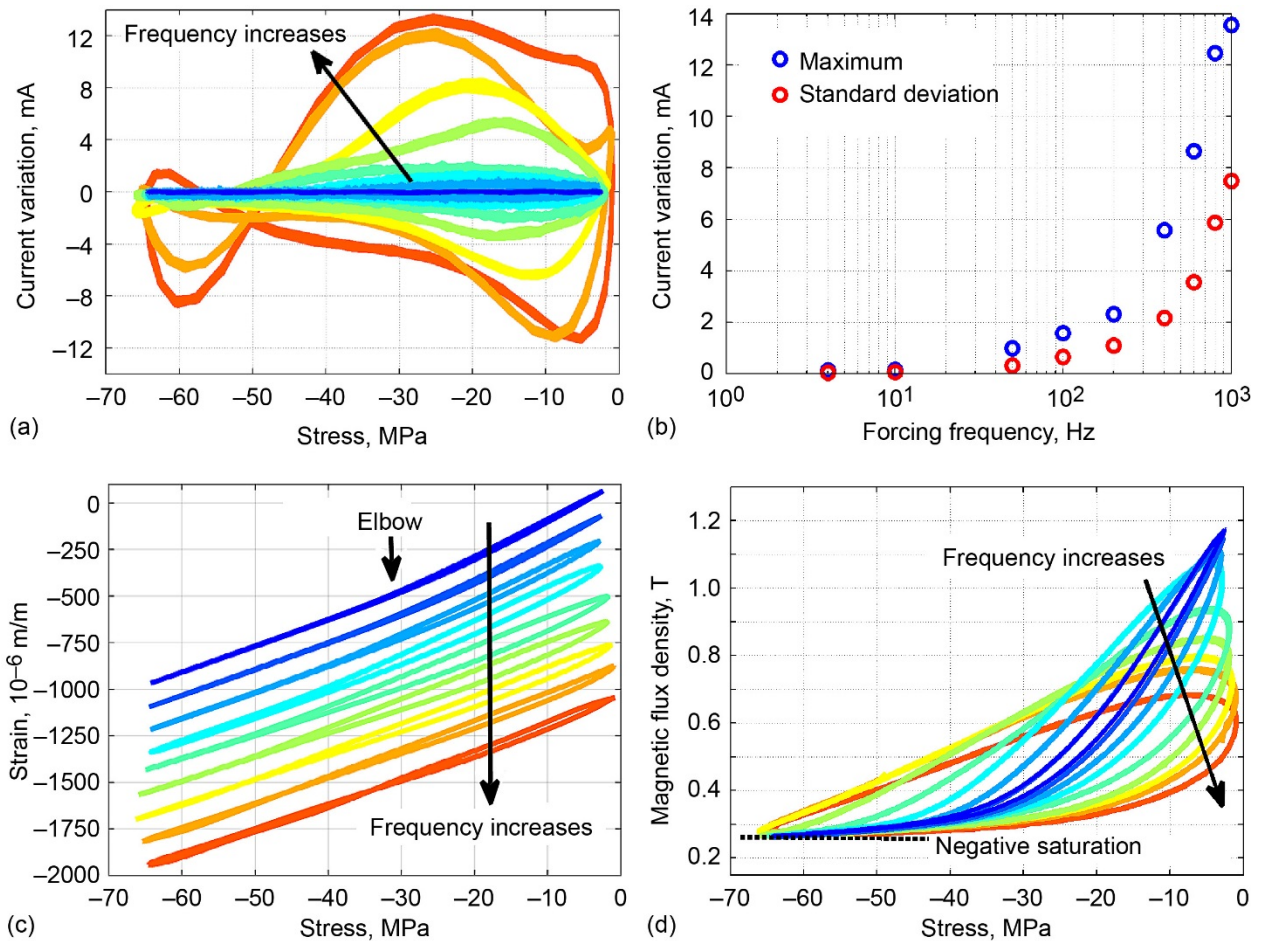
Figure 57.—Major-loop dynamic sensing response of solid Galfenol rod for bias current of 0.30 A, bias stress of −31.9 MPa, stress amplitude of 31.4 MPa, and forcing frequencies of 4, 10, 50, 100, 200, 400, 600, 800, and 1000 Hz. Color changes from blue to red as frequency increases. (a) Variation in current about current bias versus stress. (b) Maximum and standard deviation of variation in current about bias current versus forcing frequency. (c) Strain versus stress (successively shifted by −125×10⁻⁶ m/m for visualization purposes). (d) Magnetic flux density versus stress.
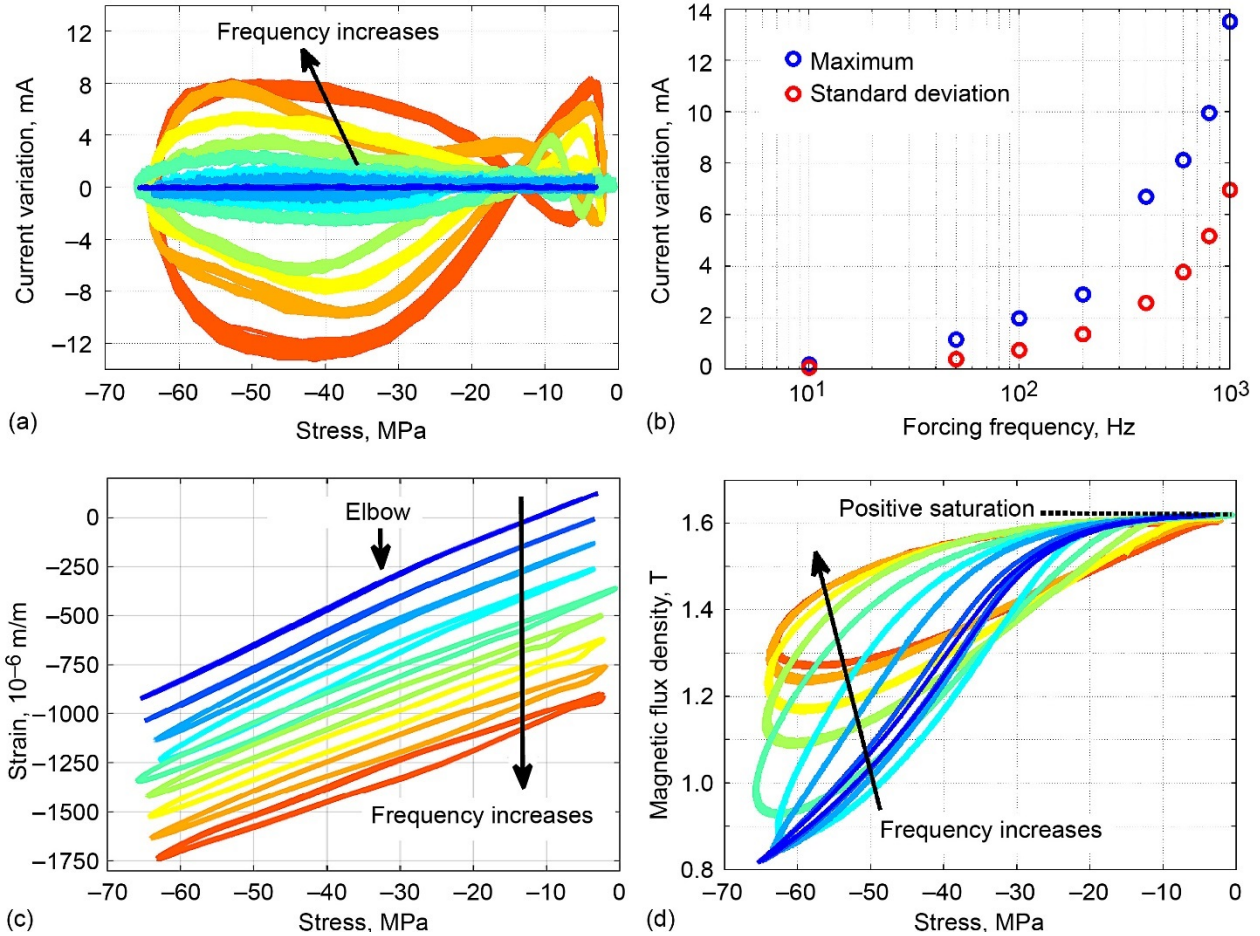
Figure 58.—Major-loop dynamic sensing response of solid Galfenol rod for bias current of 0.80 A, bias stress of −31.9 MPa, stress amplitude of 31.4 MPa, and forcing frequencies of 4, 10, 50, 100, 200, 400, 600, 800, and 1000 Hz. Color changes from blue to red as frequency increases. (a) Maximum and standard deviation of variation in current about bias current versus stress. (b) Current variation metrics versus forcing frequency. (c) Strain versus stress (successively shifted by −125×10⁻⁶ m/m for visualization purposes). (d) Magnetic flux density versus stress.

Minor-loop responses are depicted in Figure 59. The current variation and its metrics are given in Figure 59(a) and (b), respectively. Current variation is very small at all frequencies. The mechanical and magnetic responses are shown in Figure 59(c) and (d), respectively. Because of the low amplitude excitation and the bias condition, the response is nearly linear throughout the frequency range. An increase in hysteresis with frequency is clear in the strain-versus-stress and flux-density-versus-stress plots. Similar to the major-loop responses, but to a much lesser extent, the active behavior (i.e., flux density changes and a softened elastic modulus) is suppressed as frequency increases. Material properties calculated from the minor loops are shown along with those for the laminated rod in Section 9.2.

9.1.2 Constant Magnetic Field

Figure 60 presents the dynamic, major-loop sensing responses of the solid Galfenol rod at constant magnetic field. The variation in field about the bias field and the field control metrics are depicted in Figure 60(a) and (b), respectively; the performance of the field controller significantly degrades as frequency increases. For comparison, the change in magnetic field during major-loop constant-current tests was about 2.4 kA/m (30 Oe) at low frequency and 2.1 kA/m (26 Oe) at high frequency. This suggests that the magnetic field controller has a limited impact above 100 to 200 Hz. For this reason, the dynamic sensing behavior of the laminated rod was only measured at constant current. Figure 60(c) and (d) present the strain and flux density responses, respectively. Trends in these curves mirror those in the constant-current responses.
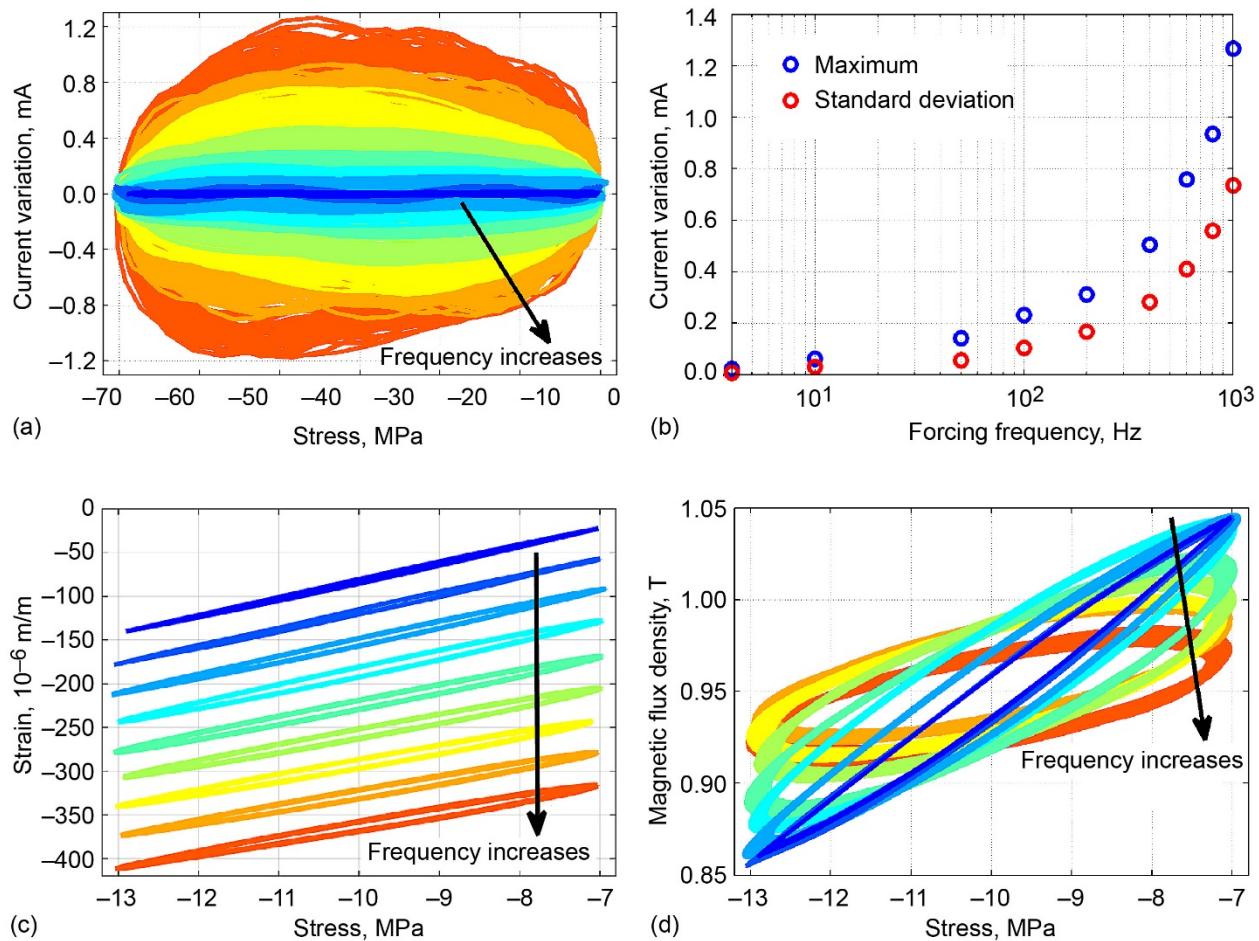
Figure 59.—Minor-loop dynamic sensing response of solid Galfenol rod for bias current of 0.30 A, bias stress of −9.93 MPa, stress amplitude of 2.88 MPa, and forcing frequencies of 4, 10, 50, 100, 200, 400, 600, 800, and 1000 Hz. Color changes from blue to red as frequency increases. (a) Maximum and standard deviation of variation in current about bias current versus stress. (b) Current variation metrics versus forcing frequency. (c) Strain versus stress (successively shifted by −35×10⁻⁶ m/m for visualization purposes). (d) Magnetic flux density versus stress.
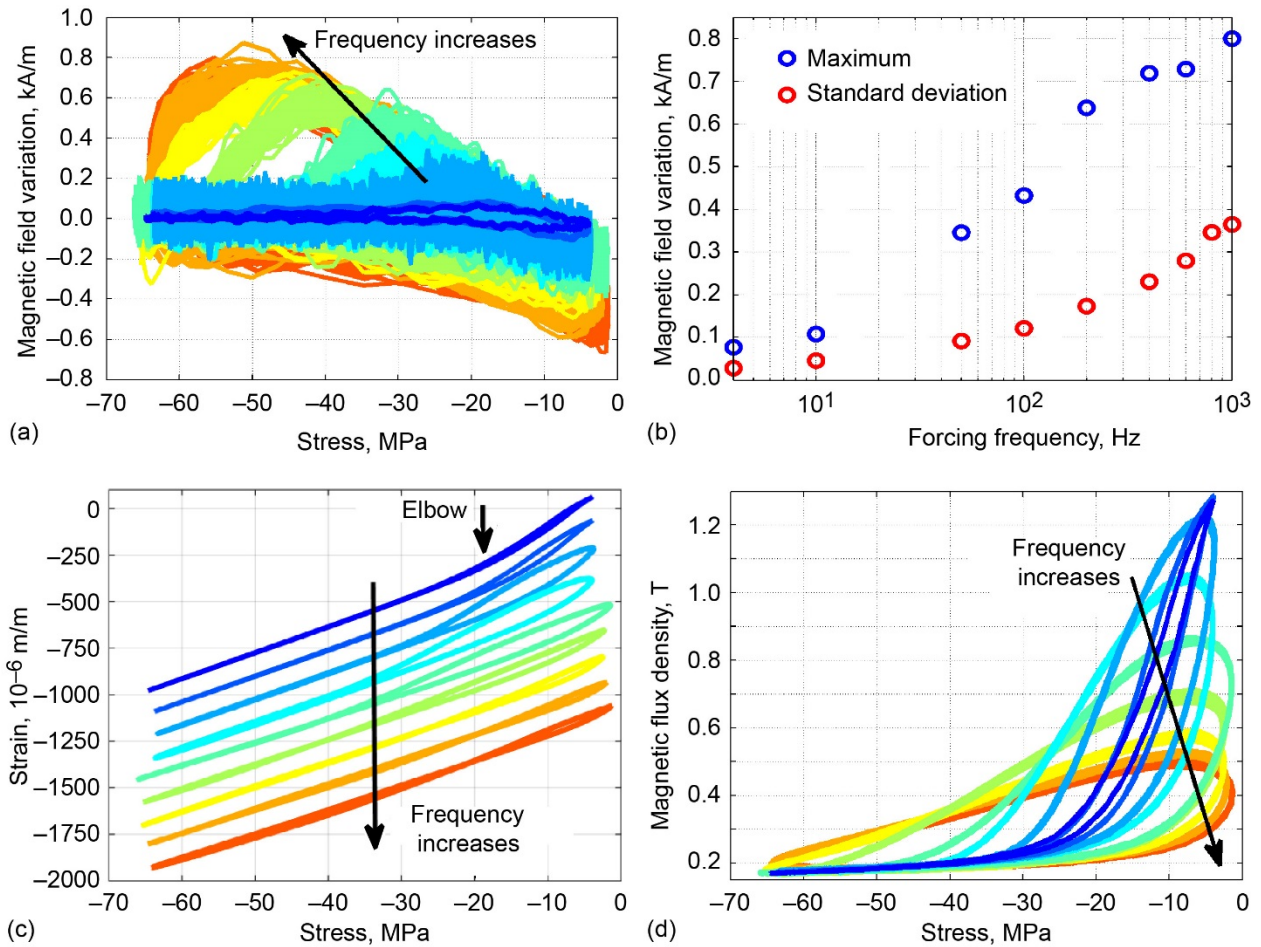
Figure 60.—Major-loop dynamic sensing response of solid Galfenol rod for bias magnetic field of 2.46 kA/m, bias stress of –31.9 MPa, stress amplitude of 31.4 MPa, and forcing frequencies of 4, 10, 50, 100, 200, 400, 600, 800, and 1000 Hz. Color changes from blue to red as frequency increases. (a) Variation in magnetic field about field bias versus stress. (b) Maximum and standard deviation of variation in magnetic field about bias field versus forcing frequency. (c) Strain versus stress (successively shifted by –125×10⁻⁶ m/m for visualization purposes). (d) Magnetic flux density versus stress.

Figure 61 shows the dynamic, minor-loop response at constant field. The effectiveness of the magnetic field controller is shown in parts (a) and (b). The absolute variation in the magnetic field is considerably lower than for dynamic, major-loop tests. However, the change in magnetic field during dynamic, minor-loop constant-current tests was only ~0.9 kA/m (~11 Oe), compared to a change of 2.1 kA/m (26 Oe) for major loops. Thus, the maximum variation in the controlled field is about 50 percent of the variation in the uncontrolled field. Since the minor-loop response is nearly linear at each forcing frequency, the analytical solution of the mechanically induced magnetic diffusion problem (Ref. 22) was used to estimate the effective (average) magnetic field inside the Galfenol rod at each forcing frequency. The results are depicted in Figure 61(c) and (d). The effective magnetic field exhibits more variation than is observed in the surface magnetic field, particularly for

frequencies below 400 Hz. The variation in the mechanical and magnetic responses are given in Figure 61(e) and (f). The slopes of the flux-density-versus-stress and strain-versus-stress responses decrease with frequency faster than at constant current because of the combined effects of suppressed magnetic moment rotation and degraded constant field control.

The dynamic modulus and piezomagnetic coefficient of the solid rod at constant field was calculated as discussed in Section 6.4 and is depicted in Figure 62. As forcing frequency increases, the lossless components of the dynamic material properties tend, nearly monotonically, toward the behavior of the rod in the saturated (passive) regime. To explain this trend, recall that the magnetomechanical coupling is maximized (i.e., maximum sensitivity and minimum elastic modulus) at the selected bias point (see Sec. 7.0). From this bias, changes in the external magnetic field due to imperfect field control and in the internal
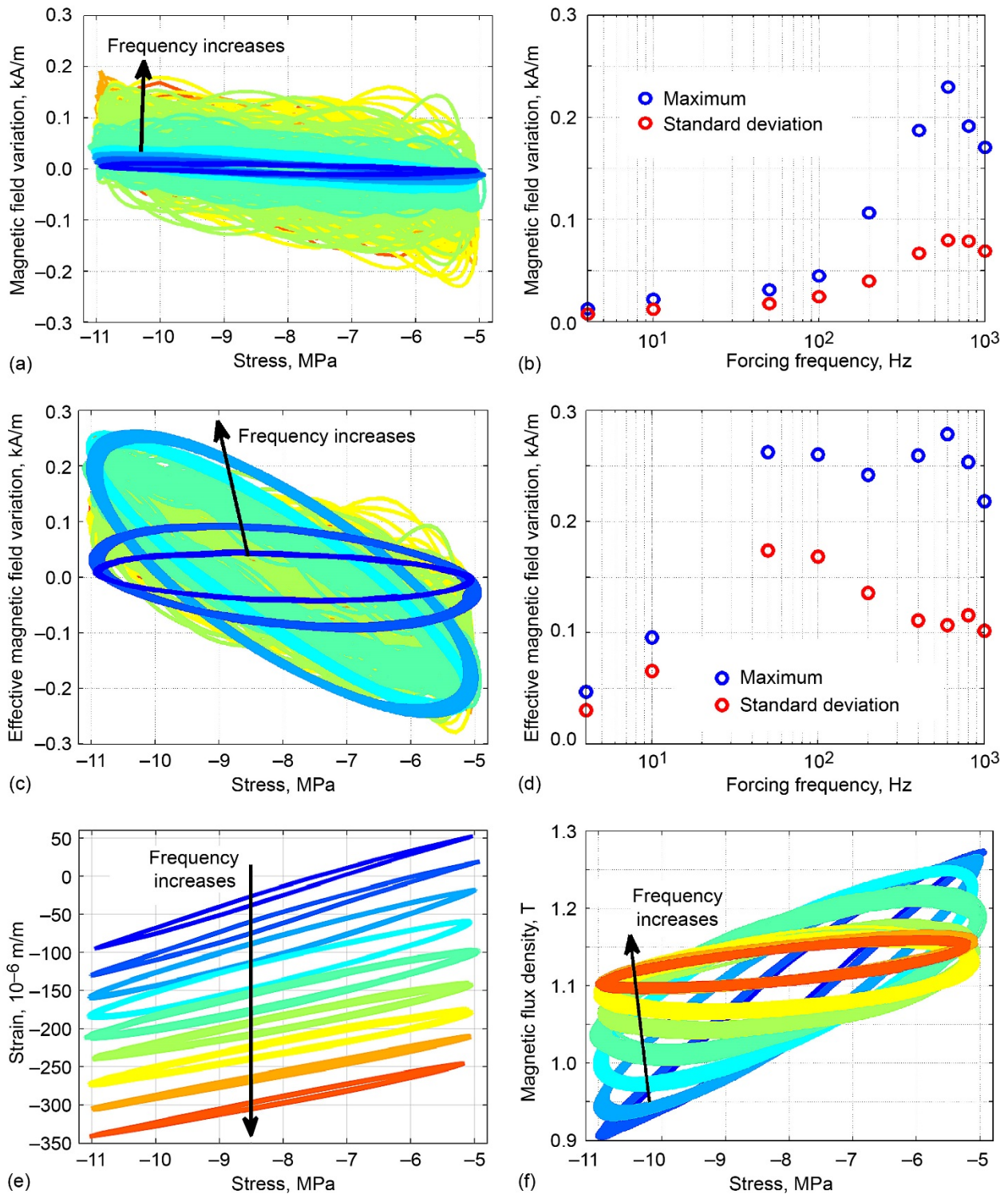
Figure 61.—Minor-loop dynamic sensing response of solid Galfenol rod for bias magnetic field of 2.46 kA/m, bias stress of −7.96 MPa, stress amplitude of 2.88 MPa, and forcing frequencies of 4, 10, 50, 100, 200, 400, 600, 800, and 1000 Hz. Color changes from blue to red as frequency increases. (a) Variation in surface field about surface field bias versus stress. (b) Maximum and standard deviation of variation in surface magnetic field about bias field versus forcing frequency. (c) Variation in effective magnetic field about effective field bias versus stress. (d) Effective field variation metrics versus forcing frequency. (e) Strain versus stress (successively shifted by −35×10^{-6} m/m for visualization purposes). (f) Magnetic flux density versus stress.
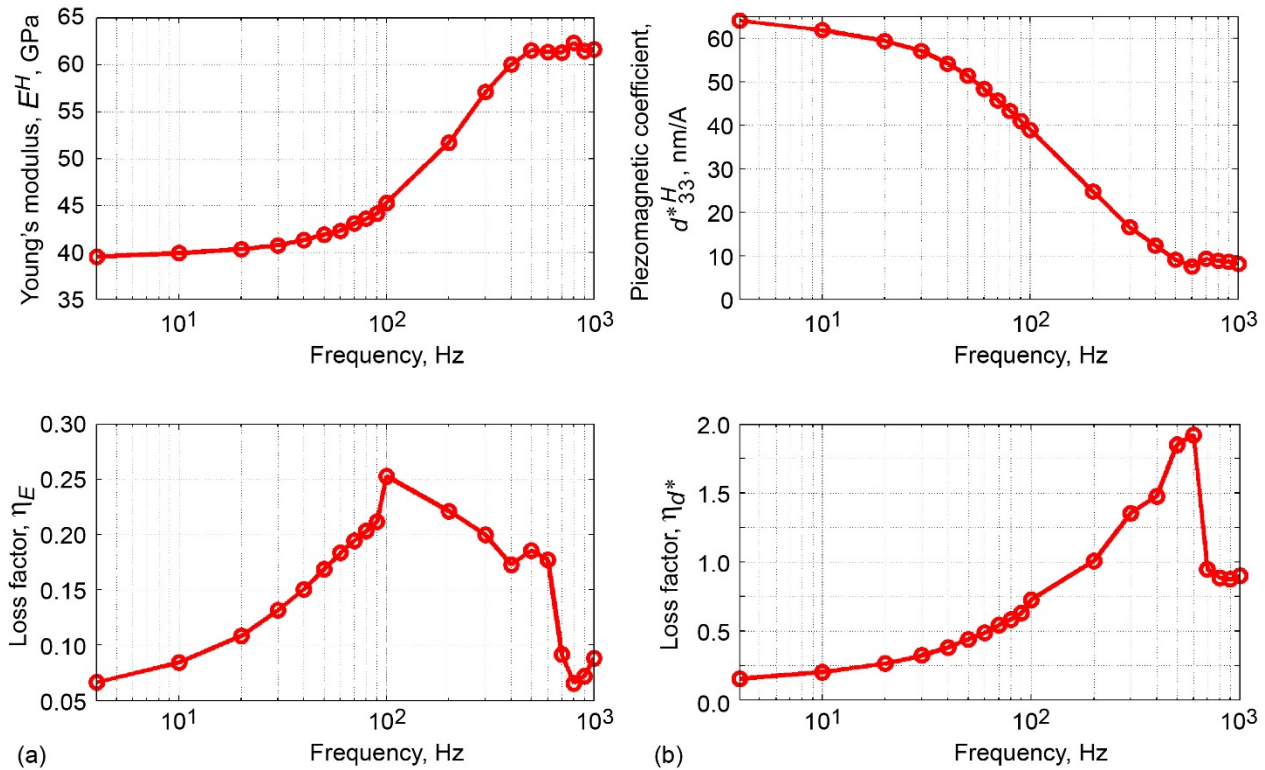
Figure 62.—Sensing-based, frequency-dependent material properties (from minor loops) of solid Galfenol rod for bias magnetic field of 2.46 kA/m, bias stress of 7.96 MPa, and stress amplitude of 2.88 MPa. (a) Elastic component E^H and loss factor η_E of dynamic Young's modulus. (b) Lossless component d^{*H}_{33} and loss factor η_{d^*} of dynamic piezomagnetic coefficient.

magnetic field due to mechanically induced magnetic diffusion both lead to reductions in the coupling. Further, the internal field varies in a manner that constrains magnetic moment rotation, and therefore the active behavior. The loss factors peak between 200 and 600 Hz, then sharply decrease between 600 and 700 Hz. This trend is unexpected, but it mirrors the magnetic field variation in Figure 61(b). Consequently, the relationship between the loss factors and the variation in the external magnetic field (i.e., input magnetic energy changes) will be investigated in future work.

9.2   Laminated Galfenol Rod

The dynamic sensing response of the laminated rod was only measured for constant current, because the measurements of the solid rod in Section 9.1.2 indicate that the magnetic field controller has a limited impact above 100 to 200 Hz. Major and minor dynamic sensing responses of the laminated Galfenol rod are shown in Figure 63 and Figure 64, respectively. The magnetic and mechanical bias conditions were identical to the constant current testing of the solid rod. For visualization purposes, strain-versus-stress responses (Figure 63(c) and Figure 64(c)) and flux-density-versus-stress responses (Figure 63(d) and Figure 64(d)) are successively shifted downward starting with the 10-Hz

response. The variation in the current about the current bias is presented in Figure 63(a) and Figure 64(a), and the current control metrics are depicted in Figure 63(b) and Figure 64(b). Although slightly worse than for the solid rod, current control still performs well. Compared to the solid rod, hysteresis increases much slower with frequency, and the quasi-static behavior extends to higher frequencies. These trends are consistent with an appreciable reduction in eddy currents. Differences in the quasi-static behavior of the solid and laminated rods can account for the remaining disparities in the dynamic responses; particularly, the change in flux density is significantly less for the laminated rod, and the active behavior occurs over a different stress range.

At 400 Hz and above, the major-loop strain-versus-stress responses exhibits repeatable, yet erratic, oscillations within each forcing cycle. The magnitude of these oscillations seems too large to be an artifact of imperfect current control or electromagnetic strain noise. This may be a result of imperfect load control. However, this behavior is nearly absent from the flux-density-versus-stress responses. The root cause is currently unknown, and further investigation is needed.

Dynamic material properties were calculated from the minor-loop responses and are shown in Figure 65 along with the dynamic properties of the solid rod. Differences in the quasi-static response of the two rods are clearly seen in the
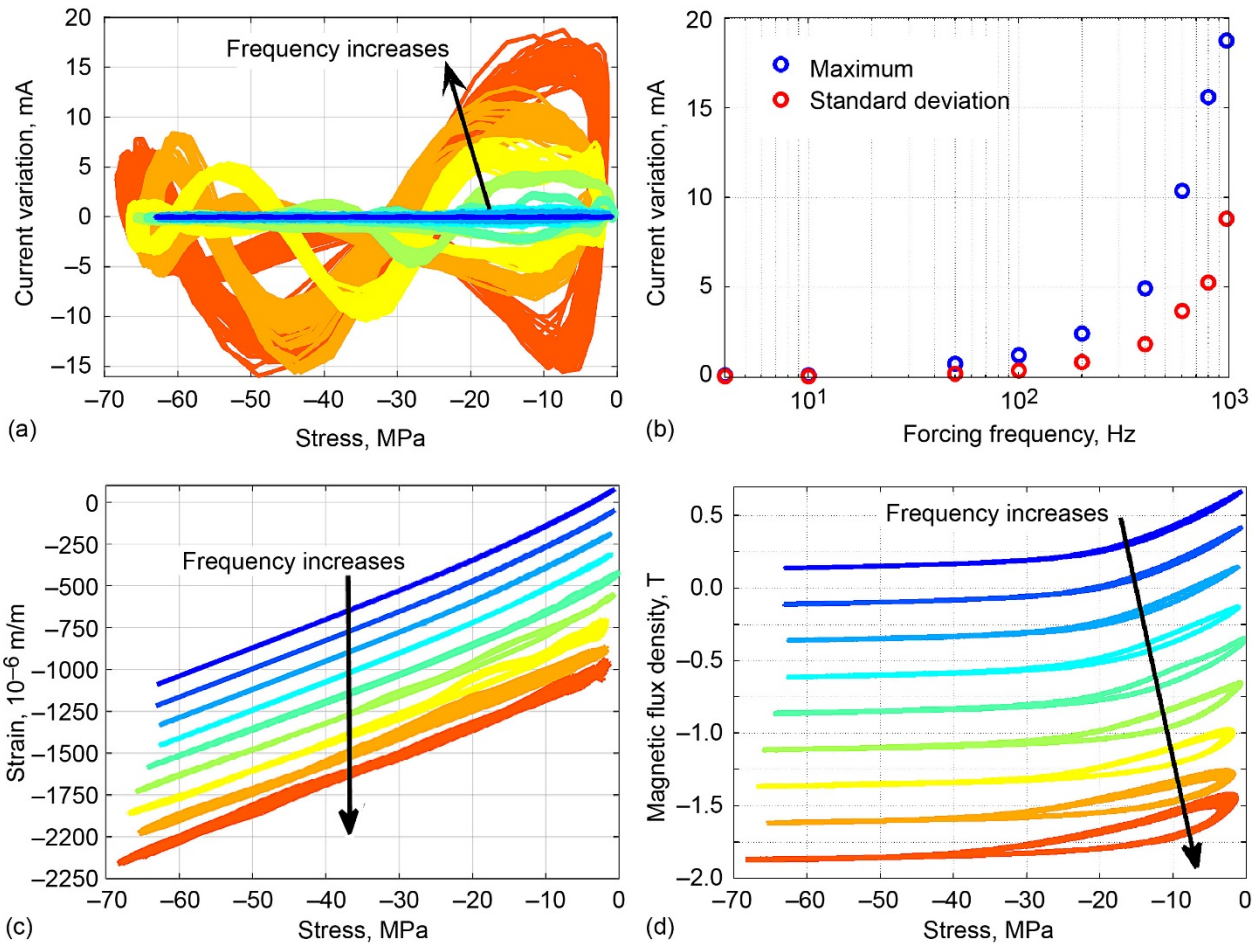
Figure 63.—Major-loop dynamic sensing response of laminated Galfenol rod for bias current of 0.30 A, bias stress of –31.9 MPa, stress amplitude of 31.4 MPa, and forcing frequencies of 4, 10, 50, 100, 200, 400, 600, 800, and 975 Hz. Color changes from blue to red as frequency increases. Strain and flux density responses are successively shifted by –125×10⁻⁶ m/m and –0.25 T, respectively, for visualization purposes. (a) Variation in current about current bias versus stress. (b) Maximum and standard deviation of variation in current about bias current versus forcing frequency. (c) Strain versus stress. (d) Magnetic flux density versus stress.
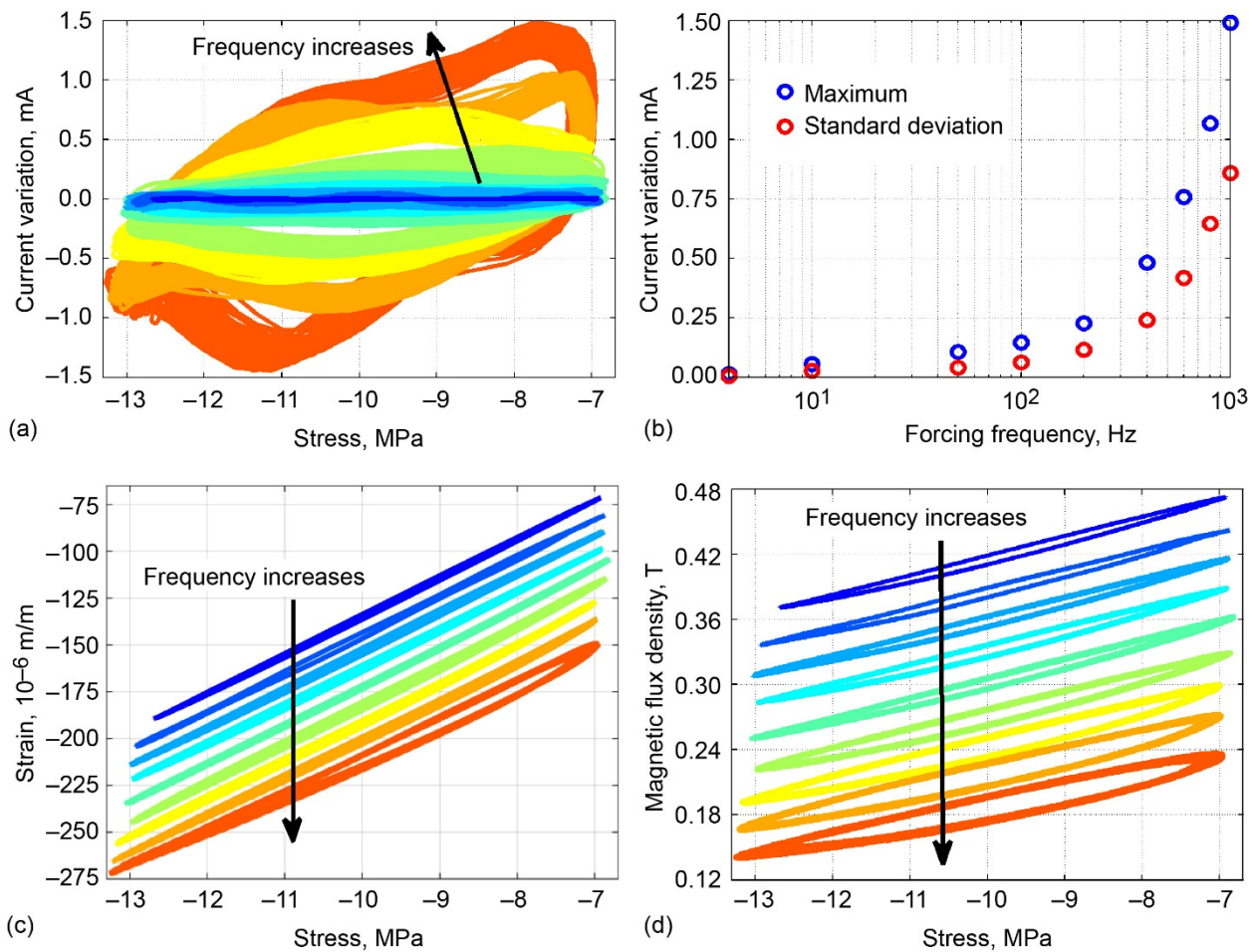
Figure 64.—Minor-loop dynamic sensing response of laminated Galfenol rod for bias current of 0.30 A, bias stress of −9.93 MPa, stress amplitude of 2.88 MPa, and forcing frequencies of 4, 10, 50, 100, 200, 400, 600, 800, and 1000 Hz. Color changes from blue to red as frequency increases. Strain and flux density responses are successively shifted by −10×10^{-6} m/m and −0.03 T, respectively, for visualization purposes. (a) Variation in current about current bias versus stress. (b) Maximum and standard deviation of variation in current about bias current versus forcing frequency. (c) Strain versus stress. (d) Magnetic flux density versus stress.
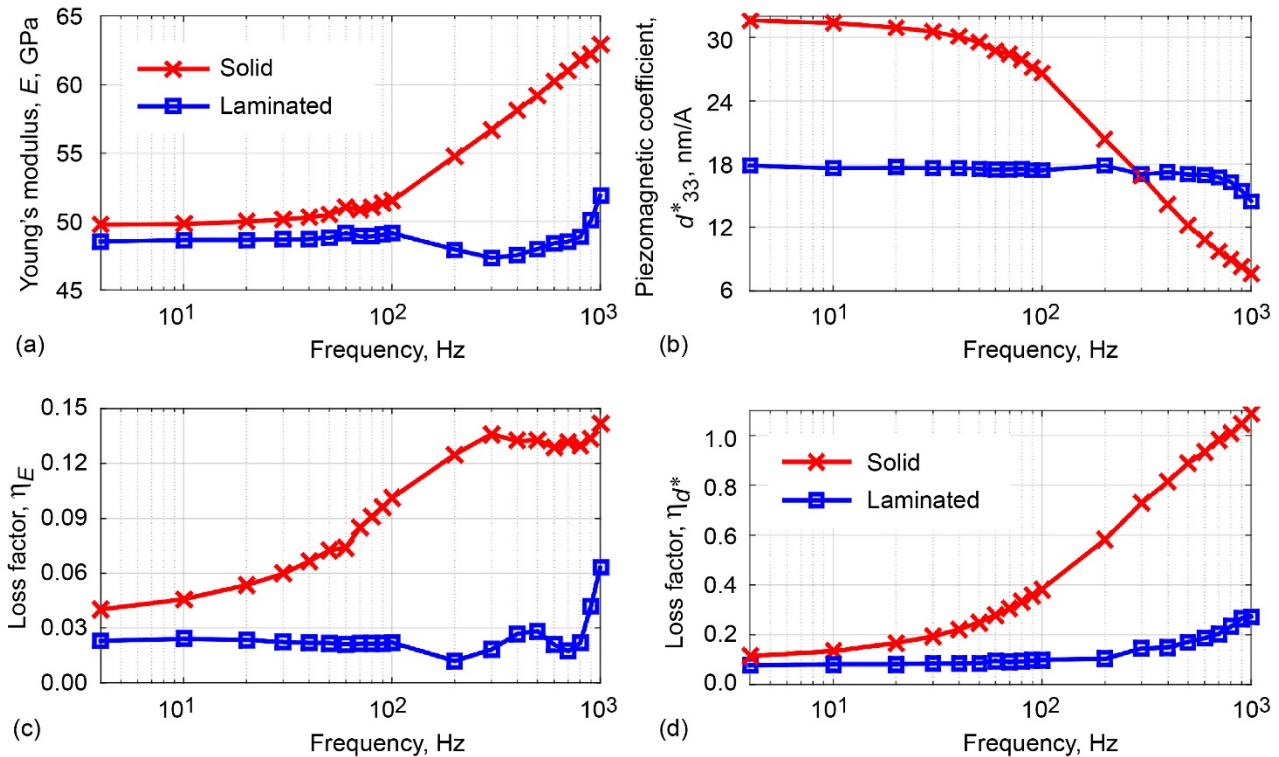
Figure 65.—Sensing-based, frequency-dependent material properties (from minor loops) of the solid and laminated Galfenol rods for bias current of 0.30 A and bias stress of 9.93 MPa. (a) Elastic component E and loss factor η_E of the dynamic Young's modulus. (b) Lossless component d^*_{33} and loss factor $\eta_{d^*_{33}}$ of dynamic piezomagnetic coefficient.

low-frequency behavior. Above ~100 Hz in the solid rod, d^{*I}_{33} decreases and E^I increases nearly exponentially. In the laminated rod, the quasi-static behavior extends to considerably higher frequencies, and losses are significantly reduced. Interestingly, E^I decreases appreciably between 100 and 300 Hz in the laminated rod. Over this frequency range, d^{*I}_{33} is nearly constant, which suggests that the magnetomechanical behavior of Galfenol is not the cause. This trend is currently unexplained.

10.0 Conclusions

Galfenol is a unique and useful magnetostrictive material that combines a moderate active response with low magnetomechanical hysteresis and high strength. This material is promising for a wide range of applications, including energy harvesters; vibration dampers; stiffness tuning components; and noncontact, robust sensors. However, a lack of experimental data on its dynamic constitutive behavior has hindered the design and optimization of such devices. This report fulfills this need by presenting a precise and complete dynamic characterization of a popular Galfenol alloy, $Fe_{81.6}Ga_{18.4}$. The objective was to measure the one-dimensional (1D), dynamic sensing response of the material and then from the response,

quantify the frequency dependence of the material properties for 1D sensing. This was accomplished by controlling the axial, dynamic stress and the static magnetic field over a specific region of a Galfenol rod and measuring the axial strain and magnetic flux density. Auxiliary variables—drive voltage, drive current, and temperature—were also measured for reference. At each forcing frequency, sensing-based material properties were calculated using a frequency-domain method adapted from an ASTM standard.

Design of the experiment was separated into six sections: (1) specimen design, (2) sensor selection and uncertainty analysis, (3) calibration methods, (4) experimental setup and methods, (5) data processing methods, and (6) procedure. The specimens were designed by considering recommendations from ASTM standards, the magnetic circuit constraints, and guidelines to avoid buckling. Solid and laminated cylindrical rod specimens of nominal dimension 7.62 by 0.627 cm (3 by 0.25 in.), length by diameter, were used. Mechanical, magnetic, and thermal sensors were selected based on a trade study of the available technologies. For each sensor, calibration methods were developed and explained. In addition, the uncertainty for each measurement was calculated at the system level using error propagation equations. In most cases, the estimated uncertainty met ASTM standards. However, the magnetic flux

density signal is expected to have 0.4 to 0.9 percent more error than the recommended ±1 percent.

The experimental setup and methods were explained in detail using photographs and schematic drawings. The system was refined to minimize the three key sources of error: (1) electromagnetic noise in strain signals due to Galfenol's magnetic response, (2) error in load signals due to the inertial force of fixturing, and (3) phase misalignment between signals due to conditioning electronics. For dynamic characterization, strain error was kept below 1.2 percent of full scale by wiring two collocated gauges in series (noise cancellation) and through leadwire weaving. Inertial force error was kept below 0.41 percent by measuring the dynamic force in the specimen using a nearly collocated piezoelectric load washer. The phase response of all conditioning electronics was explicitly measured and corrected for in postprocessing. Control of the magnetic field was briefly discussed; proportional-integral control was used for constant field testing.

To verify the experimental setup, the quasi-static actuation response of the solid Galfenol rod was measured at different constant stresses between 0 and –61.3 MPa (–8891 psi), and the sensing response was measured at different constant electromagnet currents (0 to 1 A) and constant magnetic fields (0 to 13.8 kA/m, or 173 Oe). The saturation magnetostriction 237×10^{-6} m/m, elastic modulus 72.2 GPa (10.5×10^6 psi), and flux density 1.60 T (16 kG) closely match published values for similar Galfenol materials. As expected, responses to small amplitude loading (i.e., minor loops) are circumscribed by the responses to large amplitude loading (i.e., major loops). The sensing response of the solid rod was directly compared to its actuation response by overlaying actuation points extracted from the sensing response onto actuation curves. A very close agreement between the points and curves is found, which is consistent with prior work. Interestingly, hysteresis appears slightly larger for stress cycling than for magnetic field cycling.

The sensing response of the solid and laminated rods was measured for dynamic stresses up to 31 MPa (4496 psi) and 1 kHz. For the solid rod, both constant current and constant field biases were investigated. Current control performed well, but the performance of the field controller significantly degraded above 100 to 200 Hz. In general, as frequency is increased, the sensing response becomes more linear due to an increase in eddy currents, which tend to suppress the active behavior of the material. Hysteresis significantly increases and sensitivity to stress decreases with frequency. As frequency increases above ~100 Hz, the elbow in the strain-versus-stress response disappears and the region of softened behavior stiffens until it coincides with the saturated, purely elastic regime. These trends imply that at high frequency, magnetic moment rotation is severely inhibited in the solid Galfenol rod. Under constant field conditions, the loss factors of the solid rod do not monotonically increase. Instead, they peak between 200 and 600 Hz. This unexpected behavior was not seen in constant current measurements and may result from imperfect field control. Compared to the solid rod, the laminated rod exhibits much slower increases in hysteresis with frequency, and its quasi-static behavior extends to higher frequencies. Both trends suggest an appreciable reduction in eddy currents. The elastic modulus of the laminated rod decreases between 100 and 300 Hz, then increases above 300 Hz. This trend is currently unexplained.

This novel dynamic characterization provides a detailed set of data that allows for the validation of recently developed Galfenol constitutive models that incorporate rate-dependent effects. The presented frequency-dependent material properties also permit accurate modeling of Galfenol-based systems that experience time-varying forces.

Glenn Research Center
National Aeronautics and Space Administration
Cleveland, Ohio
June 8, 2016

Appendix A.—Nomenclature

The following symbols, acronyms, and abbreviations are found in the body of this report and are defined here.

Symbols

A	cross-sectional area of test specimen
$A_{\text{lam}}^{\text{FeGa}}$	cross-sectional area of Galfenol in laminated rod
$A_{\text{solid}}^{\text{FeGa}}$	cross-sectional area of Galfenol in solid rod
a	number of measured points in Appendix B
B	magnetic flux density
B_{sat}	saturation magnetic flux density
B_3	axial magnetic flux density
$\bar{\text{B}}$	magnetic flux density vector
$\tilde{B}$	magnetic flux density signal transformed to frequency domain
$\tilde{B}(1)$	fundamental component of transformed magnetic flux density signal
b	intercept in Equation (B1)
$C_{\text{e-f}}$	end-fixity coefficient
c_{lam}^B	magnetic flux density calibration factor for laminated rod
c_{solid}^B	magnetic flux density calibration factor for solid rod
D	diameter of test specimen from ASTM standards
d_{33}^T	33 component of $[d^T]$; piezomagnetic coefficient at constant stress relating axial magnetic field to axial strain
$d^*{}_{33}$	lossless (real) component of 33 component of dynamic piezomagnetic coefficient matrix relating axial stress to axial magnetic flux density
$d^*{}_{33}^H$	33 component of $\left[d^{*H}\right]$; piezomagnetic coefficient at constant magnetic field relating axial stress to axial magnetic flux density
$d^*{}_{33}^I$	33 component of $\left[d^{*I}\right]$; piezomagnetic coefficient at constant current relating axial stress to axial magnetic flux density
$\tilde{d}^*{}_{33}$	33 component of dynamic piezomagnetic coefficient matrix relating axial stress to axial magnetic flux density

$[d^T]$	piezomagnetic coefficient matrix at constant stress
$\left[d^{*H}\right]$	piezomagnetic coefficient matrix at constant magnetic field
$\left[d^{*I}\right]$	piezomagnetic coefficient matrix at constant current
$denom$	parameter defined in Equation (C7)
E	elastic component of dynamic Young's modulus
E_{max}	maximum value of Young's modulus for specimen buckling calculations
E_{min}	minimum value of Young's modulus for specimen buckling calculations
E_{sat}	saturation elastic modulus
E^H	Young's modulus at constant magnetic field
E^I	Young's modulus at constant current
$\tilde{E}$	dynamic Young's modulus
e_d	error due to inertial force for dynamic test)
e_{k_g}	elemental errors comprising instrument error in uncertainty
e_q	error due to inertial force for quasi-static test
e_S	normalized strain error due to electromagnetic noise
F	applied axial force
F_{dynamic}	dynamic force expression for calculation of uncertainty
$F_{\text{load cell}}$	force measured by load cell
$F_{\text{load washer}}(t)$	force measured by load washer
$F_{\text{load frame}}(t)$	force applied by load frame
F_0	magnitude of harmonic force applied to load path in Appendix C
$F_{1,2,3}$	forces in load path in Equations (24) and (25) and Appendix C
f	frequency of generated signal
f_G	gauge factor of strain gauge
f_1	first transverse bending natural frequency
Δf_G	variation in gauge factor with temperature
$G_g(s)$	transfer function of signal conditioning and data acquisition equipment used for phase calibration
H	magnetic field (kA/m)

H_ref	the magnetic field (H_ref) measured by gaussmeter and Hall probe for reference during calibration	R_C	resistance of shunt calibration resistor
H_min	minimum magnetic field	R_G	resistance of strain gauge
H_surface	magnetic field at surface	R_load	resistance of electrical load
H_3	axial magnetic field	R_source	source impedance of amplifier's output
$\vec{H}$	magnetic field vector	R_Wh1	resistance of active arm of Wheatstone quarter-bridge circuit
h_ad	thickness of the adhesive used to bond strain gauges	R_Wh2	resistance of adjacent arm of Wheatstone quarter-bridge circuit; bridge completion resistor
h_bk	thickness of strain gauge's backing	R_Wh3	bridge completion resistor
I	area moment of inertia about the centroid of the cross section of test specimen	R_Wh4	bridge completion resistor
i	known input affecting sensor sensitivity in Appendix B	r	radius of curvature of test specimen
J	parameter in Equation (7), defined in Equation (8)	S	measured strain
j	$\sqrt{-1}$	S_3	axial strain
K	gain applied by the signal scaling circuitry during phase calibration	$S_{3,\text{sim}}$	axial strain simulated by shunting the effective gauge with shunt resistor at its terminals
K_P, K_I, K_D	proportional, integral, and derivative control gains	S_span	strain span (1350×10^{-6} for this experiment)
$k_{1,2,3}$	springs representing sample and force transducers in determination of inertial force error by lumped-parameters model	$S_{\Theta/0}$	thermal strain output of strain gauge relative to thermal output at temperature for which strain indicator is zeroed
L	length of test specimen from ASTM standards	$\Delta S_{\Theta/0}$	correction to thermal strain output due to surface curvature of installation location
$M_g(\omega)$	magnitude of transfer function of signal conditioning equipment	S_true	true strain
m	sensor sensitivity in Appendix B	S'	uncorrected measured strain
$m_{2,3}$	masses representing fixtures in determination of inertial force error by lumped parameters model	S''	measured strain corrected for Wheatstone quarter-bridge circuit nonlinearity and resistance imbalance
m_l	mass of loaded load washer	S'''	measured strain corrected for Wheatstone quarter-bridge nonlinearity, resistance imbalance, and thermal effects
m_u	mass of unloaded load washer		
N	number of variables on which the result Q depends	$\vec{S}$	strain vector
n	mode number of transverse bending mode shape	$\tilde{S}$	strain signal transformed to frequency domain
o	voltage output in Appendix B	$\tilde{S}(1)$	fundamental component of transformed strain signal
P	applied axial force		
P_crit	critical buckling load at which frequency of transverse bending becomes zero	s_{33}^H	33 component of $\left[s^H\right]$; compliance at constant magnetic field relating axial stress to axial strain
p	range setting (in newtons per volts) of load washer's charge amplifier	$\left[s^H\right]$	compliance matrix at constant magnetic field
Q	quantity calculated from measured variables	$Sens_\text{charge amp}$	sensitivity of charge amplifier (volts per picocoulomb)
$q_\text{load washer}$	charge generated by load washer (picocoulombs)	$Sens_\text{Hall}$	sensitivity of Hall chip
δR	resistance imbalance between active arm and its adjacent arm of Wheatstone quarter-bridge circuit	SS_{ii}, SS_{io}	sum of squares used for linear, least-squares regression
		T	measured stress

$\bar{\mathrm{T}}$	stress vector	V_{noise}	electromagnetic noise
$\tilde{T}$	stress signal transformed to frequency domain	V_{out}	total Wheatstone quarter-bridge circuit output
$\tilde{T}(1)$	fundamental component of transformed stress signal	$V_{\text{out,1}}$	Wheatstone quarter-bridge circuit output due to excitation voltage
T_{crit}	critical buckling stress at which the natural frequency of transverse bending becomes zero	$V_{\text{out,2}}$	Wheatstone quarter-bridge circuit output due to noise voltage
$\Delta\Theta_{\text{ref}}$	difference between testing temperature and temperature at which strain indicator is zeroed	V_r	normalized noise voltage
		$V_{\text{Type K}}$	simulated voltage of Type K thermocouple
$\Delta\Theta_{\text{room}}$	is the difference between the testing temperature and room temperature	V_0	output voltage of Wheatstone quarter-bridge circuit relative to zero strain state
T_3	axial stress	W_{B-T}	hysteresis loss per cycle in B_3-versus-T_3 response
t	time	W_{S-T}	hysteresis loss per cycle in S_3-versus-T_3 response
t_d	time delay of signal conditioning equipment	w_n	mode shape (eigenfunction) of transverse vibration of beam subjected to axial force
$t_d{}^B$	time delay of flux density measurement channel		
$t_d{}^{B/H}$	time delay of flux density measurement channel relative to time delay of magnetic field measurement channel	X_i	magnitude of motion (x_i) of each mass m_i
		x	location along test specimen's length
		x_g	harmonic motion
$t_d{}^H$	time delay of magnetic field measurement channel	Y	parameter in Equation (7), defined in Equation (8)
$u(t)$	Heaviside step function	Z_g	constants in Equation (2) that depend on boundary conditions
U_{C_g}	instrument error within uncertainty of z_g		
		z_g	measured variable
U_{field}	uncertainty in calculated magnetic field	α_{ad}	coefficient of thermal expansion of adhesive used to bond strain gauges
U_{flux}	uncertainty in magnetic flux density		
U_{force}	uncertainty in force calculation	α_{bk}	coefficient of thermal expansion of strain gauge's backing
U_m	uncertainty in calculated sensitivity		
U_Q	uncertainty in calculated quantity Q	α_S	coefficient of thermal expansion of test specimen
U_{sens}	uncertainty in Hall chip sensitivity	β	parameter in Equation (6)
$U_{SS_{ii}}$, $U_{SS_{io}}$	uncertainties in sum of squares used for linear, least-squares regression	γ_1, γ_2	roots of auxiliary equation from which eigenfunctions and eigenvalues of transverse bending vibration are derived; defined in Equation (3)
U_{strain}	uncertainty in strain calculation		
U_{stress}	uncertainty in stress calculation		
U_{z_g}	uncertainty in z_g	$\delta_{T/B}$	phase angle by which stress leads magnetic flux density
U_{i_g} , U_i	uncertainty in voltage input		
		$\delta_{T/S}$	phase angle by which stress leads strain
U_{o_g} , U_o	uncertainty in voltage output	η_{d*}	loss factor associated with piezomagnetic coefficient
U_{0_g}	interpolation error within uncertainty of z_g		
		η_E	loss factor associated with Young's modulus
V	voltage signal	Θ	measured temperature
V_{coil}	voltage induced in magnetic flux density sensing coil	$\Delta\Theta$	temperature difference used to calculate uncertainty in strain
V_{control}	static control voltage	λ_{sat}	saturation magnetostriction
V_{ex}	excitation voltage	μ_{33}^T	33 component of $\left[\mu^T\right]$
V_{Hall}	Hall chip voltage		
V_{load}	voltage across resistive load	$\left[\mu^T\right]$	magnetic permeability matrix at constant stress

$\nu_{ad\text{-}bk}$	average Poisson's ratio of strain gauge's adhesive and backing	$\omega_{1,u}$	natural frequency of unloaded load washer
ρ	mass density of test specimen	$\omega_{1,l}$	natural frequency of loaded load washer
σ	axial stress	**Acronyms**	
$\phi_g(\omega)$	phase of transfer function of signal conditioning equipment	1D	one-dimensional
$\phi^B(\omega)$	phase response of magnetic flux density measurement channel	A/D	analog-to-digital
		AC	alternating current
$\phi^H(\omega)$	phase response of magnetic field measurement channel	ADC	analog-to-digital converter
		APC	amplitude-phase compensator
$\phi^{B/H}(\omega)$	phase response of magnetic flux density channel relative to magnetic field channel	DAC	digital-to-analog converter
		DFT	discrete Fourier transform
ω	circular frequency of excitation force	GMR	giant magnetoresistive
ω_n	circular natural frequency of transverse vibration (eigenvalues)	PID	proportional-integral-derivative

Appendix B.—Uncertainty in the Calibration of a Sensor's Sensitivity

A sensor's sensitivity m is calibrated through a linear, least-squares regression of its voltage output o relative to a known input i,

$$o = mi + b \tag{B1}$$

where b is the zero offset and

$$m = \frac{SS_{io}}{SS_{ii}} \tag{B2}$$

The sum of squares, SS_{io} and SS_{ii}, are defined in terms of the a measured points (i_g, o_g) and their means, $\bar{i}$ and $\bar{o}$:

$$SS_{io} = \left(\sum_{g=1}^{a} i_g o_g \right) - a\bar{i}\bar{o} \tag{B3}$$

$$SS_{ii} = \left(\sum_{g=1}^{a} i_g^2 \right) - a\bar{i}^2 \tag{B4}$$

Insertion of Equation (B2) into Equation (9) gives the uncertainty in the calculated sensitivity,

$$U_m = \pm \left[\left(\frac{1}{SS_{ii}} U_{SS_{io}} \right)^2 + \left(\frac{-SS_{io}}{SS_{ii}^2} U_{SS_{ii}} \right)^2 \right]^{1/2} \tag{B5}$$

where

$$U_{SS_{io}} = \left[\sum_{g=1}^{a} \left[\left(\frac{\partial SS_{io}}{\partial i_g} U_{i_g} \right)^2 \right] + \sum_{g=1}^{a} \left[\left(\frac{\partial SS_{io}}{\partial o_g} U_{o_g} \right)^2 \right] \right]^{1/2} \tag{B6}$$

and

$$U_{SS_{ii}} = \left[\sum_{g=1}^{a} \left[\left(\frac{\partial SS_{ii}}{\partial i_g} U_{i_g} \right)^2 \right] \right]^{1/2} \tag{B7}$$

and where $U_{i_g} = U_i$ and $U_{o_g} = U_o$ are the uncertainty in i and o, respectively. The partial derivatives of Equations (B3) and (B4) are

$$\frac{\partial SS_{io}}{\partial i_g} = o_g - \frac{1}{a} \sum_{g=1}^{a} o_g \tag{B8}$$

$$\frac{\partial SS_{io}}{\partial o_g} = i_g - \frac{1}{a} \sum_{g=1}^{a} i_g \tag{B9}$$

and

$$\frac{\partial SS_{ii}}{\partial i_g} = 2(i_g - \bar{i}) \tag{B10}$$

Simplification of Equations (B6) and (B7) using Equations (B8) to (B10) gives

$$U_{SS_{io}} = \left[U_i^2 \sum_{g=1}^{a} \left[(o_g - \bar{o})^2 \right] + U_o^2 \sum_{g=1}^{a} \left[(i_g - \bar{i})^2 \right] \right]^{1/2} \tag{B11}$$

and

$$U_{SS_{ii}} = 2U_i \left[\sum_{g=1}^{a} \left[(i_g - \bar{i})^2 \right] \right]^{1/2} \tag{B12}$$

For a given set of a calibration points (i_g, o_g), U_m is evaluated by inserting Equations (B3), (B4), (B11), and (B12) into Equation (B5).

Appendix C.—Error in Force Measurements Due to Inertial Forces

Figure 24, the mechanical models for each inertial force error case, is repeated here for reference.

For the quasi-static case, m_2 and k_1 are zero. Thus, the response of the interface fixture m_3 to a harmonic force $F_0 \exp(j\omega t)$ applied to the sample k_2 is derived by assuming a harmonic motion of the fixture, x_3:

$$x_3 = \frac{F_0}{k_3 - m_3\omega^2} \exp(j\omega t) \tag{C1}$$

where ω is the circular frequency of the forcing. To be consistent with ASTM E467 (Ref. 12), the error in the load cell measurement of the force in the specimen is defined as the absolute error normalized by the loading span (peak-to-peak dynamic force):

$$e_q = \frac{F_3 - F_2}{2|F_2|} = \frac{m_3\omega^2}{2(k_3 - m_3\omega^2)} \exp(j\omega t) \tag{C2}$$

The magnitude of the error is thus

$$|e_q| = \frac{m_3\omega^2}{2|k_3 - m_3\omega^2|} \tag{C3}$$

For the dynamic case, the governing ordinary differential equation for the 2-degree-of-freedom model is

$$\begin{bmatrix} m_2 & 0 \\ 0 & m_3 \end{bmatrix} \begin{Bmatrix} \ddot{x}_2 \\ \ddot{x}_3 \end{Bmatrix} + \begin{bmatrix} k_2 & -k_2 \\ -k_2 & k_2 + k_3 \end{bmatrix} \begin{Bmatrix} x_2 \\ x_3 \end{Bmatrix} = \begin{Bmatrix} F_1 \\ 0 \end{Bmatrix} \tag{C4}$$

For a harmonic force ($F_1 = F_0 \exp(j\omega t)$), the responses are also harmonic,

$$\begin{Bmatrix} x_2 \\ x_3 \end{Bmatrix} = \begin{Bmatrix} X_2 \\ X_3 \end{Bmatrix} \exp(j\omega t) \tag{C5}$$

where Xi is the magnitude of each response.

Inserting Equation (C4) into Equation (C3) and solving the system, one gets

$$\begin{Bmatrix} x_2 \\ x_3 \end{Bmatrix} = \begin{Bmatrix} \dfrac{k_2 + k_3 - m_3\omega^2}{denom} \\ \dfrac{k_2}{denom} \end{Bmatrix} F_0 \exp(j\omega t) \tag{C6}$$

where

$$denom = m_2 m_3 \omega^4 + \left(-k_2 m_3 - (k_2 + k_3) m_2\right)\omega^2 + k_2 k_3 \tag{C7}$$

The error in the load cell measurement of the force in the specimen is

$$e_d = \frac{F_2 - F_1}{2|F_1|} = \frac{k_2(x_2 - x_3) - F_1}{2|F_1|} \tag{C8}$$

Simplification of Equation (C7) using Equations (C5) and (C6) gives

$$e_d = \frac{F_2 - F_1}{2|F_1|}$$
$$= -\frac{1}{2}\left(1 + \frac{k_2(k_3 - m_3\omega^2)}{m_2\omega^2(m_3\omega^2 - (k_2 + k_3))}\right)^{-1} \exp(j\omega t) \tag{C9}$$

and

$$|e_d| = \frac{1}{2}\left(1 + \left|\frac{k_2(k_3 - m_3\omega^2)}{m_2\omega^2(m_3\omega^2 - (k_2 + k_3))}\right|\right)^{-1} \tag{C10}$$
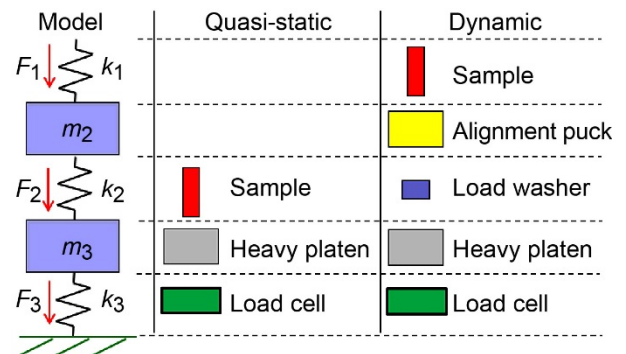

Figure 24.—Load path and mechanical model for inertial force error estimation in quasi-static and dynamic test setups, where $m_{2,3}$ are fixtures modeled as masses, $k_{1,2,3}$ are sample and force transducers modeled as springs, and $F_{1,2,3}$ are the forces they experience.

Appendix D.—Effect of Electromagnetic Noise on Strain Measurement

Figure 27, a Wheatstone quarter-bridge circuit subjected to electromagnetic noise, is repeated here for reference.

The total output V_{out} of this circuit is a superposition of the outputs due to the excitation voltage and noise voltage, $V_{out,1}$ and $V_{out,2}$, respectively,

$$\frac{V_{out,1}}{V_{ex}} = \frac{\dfrac{2\overline{R}_G}{R_2}}{\dfrac{2\overline{R}_G}{R_2}+1} - \frac{\dfrac{R_3}{R_4}}{\dfrac{R_3}{R_4}+1} = \frac{f_G S_{true}}{4+2f_G S_{true}} \tag{D1}$$

and

$$V_{out,2} = V_{noise}\frac{R_2}{2\overline{R}_G+R_2} = \frac{V_{noise}}{2+f_G S_{true}} \tag{D2}$$

where S_{true} is the true strain, f_G is the gauge factor, R_G is the resistance of the strain gauge (i.e., one of the two strain gauges that are wired in series to form a single effective strain gauge of resistance $2R_G$), V_{noise} is the electromagnetic noise, and simplifications were made using $R_2 = 2R_G$, $R_3 = R_4$, and $\overline{R}_G = R_G(1+f_G S_{true})$. The total output can be written as

$$V_{out} = \frac{2V_{noise}+f_G S_{true}V_{ex}}{4+2f_G S_{true}} \tag{D3}$$

where V_{ex} is the excitation voltage. The measured strain S is calculated from the bridge output voltage using

$$S = \frac{4}{f_G\left(\dfrac{V_{ex}}{V_{out}}-2\right)} \tag{D4}$$

Insertion of Equation (D3) into Equation (D4) followed by simplification gives

$$S = \frac{f_G S_{true}+2V_r}{f_G(1-V_r)} \tag{D5}$$

where V_r is the normalized noise voltage:

$$V_r = \frac{V_{noise}}{V_{ex}} \tag{D6}$$

If the noise voltage is zero, the measured strain becomes the true strain. The error in the strain measurement due to the electromagnetic noise, normalized by the strain span S_{span} is

$$e_S = \frac{S-S_{true}}{S_{span}} = \frac{V_r(f_G S_{true}+2)}{f_G S_{span}(1-V_r)} \tag{D7}$$
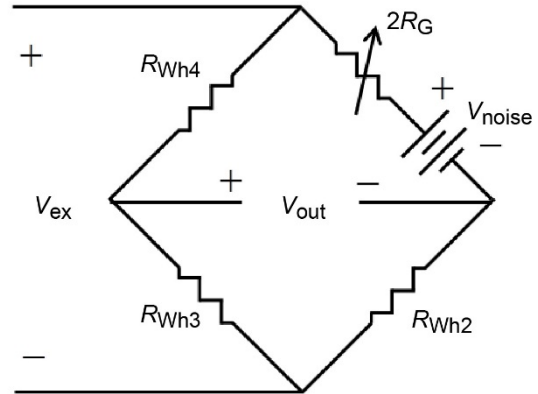

Figure 27.—Wheatstone quarter-bridge strain measurement circuit considering electromagnetic noise V_{noise} (leadwire resistance neglected). Here, R_G is resistance of strain gauge; R_{Wh2}, R_{Wh3}, and R_{Wh4} are bridge completion resistors; V_{ex} is excitation voltage; and V_{out} is total Wheatstone quarter-bridge circuit output.

References

1. Prajpati, K., et al.: Effect of Cyclic Stress on Terfenol-D. IEEE Trans. Magn., vol. 32, no. 5, 1996, pp. 4761–4763.

2. Prajapti, K.; Greenough, R.D.; and Wharton, A.: Magnetic and Magnetoelastic Response of Stress Cycled Terfenol-D. J. Appl. Phys., vol. 81, 1997, pp. 5719–5721.

3. Atulasimha, Jayasimha; and Flatau, Alison B.: A Review of Magnetostrictive Iron-Gallium Alloys. Smart Mater. Struct., vol. 20, 2011, p. 043001.

4. Walker, Travis W.: Experimental Characterization and Modeling of Galfenol (FeGa) Alloys for Sensing. M.S. Thesis, The Ohio State University, 2012.

5. Weng, Ling, et al.: Relationships Between Magnetization and Dynamic Stress for Galfenol Rod Alloy and Its Application in Force Sensor. J. Appl. Phys., vol. 113, 17A917, 2013.

6. ASTM E4–14: Standard Practices for Force Verification of Testing Machines. ASTM International, West Conshohocken, PA, 2014.

7. ASTM D5992–96(2011): Standard Guide for Dynamic Testing of Vulcanized Rubber and Rubber-Like Materials Using Vibratory Methods. ASTM International, West Conshohocken, PA, 2011.

8. ASTM E111–04(2010): Standard Test Method for Young's Modulus, Tangent Modulus, and Chord Modulus. ASTM International, West Conshohocken, PA, 2010.

9. ASTM E209–00(2010): Standard Practice for Compression Tests of Metallic Materials at Elevated Temperatures with Conventional or Rapid Heating Rates and Strain Rates. ASTM International, West Conshohocken, PA, 2010.

10. ASTM E9–09: Standard Test Methods of Compression Testing of Metallic Materials at Room Temperature. ASTM International, West Conshohocken, PA, 2009.

11. ASTM E251–92(2009): Standard Test Methods for Performance Characteristics of Metallic Bonded Resistance Strain Gages. ASTM International, West Conshohocken, PA, 2014.

12. ASTM E467–08: Standard Practice for Verification of Constant Amplitude Dynamic Forces in an Axial Fatigue Testing System. ASTM International, West Conshohocken, PA, 2014.

13. ASTM E1875–13: Standard Test Method for Dynamic Young's Modulus, Shear Modulus, and Poisson's Ratio by Sonic Resonance. ASTM International, West Conshohocken, PA, 2013.

14. ASTM E1876–09: Standard Test Method for Dynamic Young's Modulus, Shear Modulus, and Poisson's Ratio by Impulse Excitation of Vibration. ASTM International, West Conshohocken, PA, 2009.

15. ASTM E466–07: Standard Practice for Conducting Force Controlled Constant Amplitude Axial Fatigue Tests of Metallic Materials. ASTM International, West Conshohocken, PA, 2007.

16. ASTM A341/A341M–00(2011)e1: Standard Test Method for Direct Current Magnetic Properties of Materials Using D-C Permeameters and the Ballistic Test Methods. ASTM International, West Conshohocken, PA, 2011.

17. COMSOL, Inc.: COMSOL Multiphysics. Burlington, MA, 2015. http://www.comsol.com/comsol-multiphysics Accessed Sept. 9, 2015.

18. Weng, Ling, et al.: Major and Minor Stress-Magnetization Loops in Textured Polycrystalline $Fe_{81.6}Ga_{18.4}$ Galfenol. J. Appl. Phys., vol. 113, 024508, 2013.

19. Deng, Zhangxian; and Dapino, Marcelo J.: Characterization and Finite Element Modeling of Galfenol Minor Flux Density Loops. J. Intell. Mater. Syst. Struct., vol. 26, no. 1, 2015, pp. 47–55.

20. Rao, Singiresu S.: Mechanical Vibrations. Fourth ed., Pearson Prentice Hall, Upper Saddle River, NJ, 2003.

21. Yoo, J.H.; Murray, A.; and Flatau, A.B.: Evaluation of Magnetostrictive Shunt Damper Performance Using Iron (Fe)-Gallium (Ga) Alloy. Proceedings of SPIE, vol. 9057, paper no. 9057 31, 2014.

22. Scheidler, Justin J.; and Dapino, Marcelo J.: Mechanically Induced Magnetic Diffusion in Cylindrical Magnetoelastic Materials. J. Magn. Magn. Mater., vol. 397, 2016, pp. 233–239.

23. Figliola, Richard S.; and Beasley, Donald E.: Theory and Design for Mechanical Measurements. Fourth ed., John Wiley & Sons, Inc., Hoboken, NJ, 2006.

24. Japanese Industrial Standard: General Rules for Fatigue Testing of Metals. JIS Z 2273–1978, Translated and Published by Japanese Standards Association, Tokyo, Japan, 1978.

25. International Organization for Standardization: Rubber, Vulcanized or Thermoplastic— Determination of Dynamic Properties—Part 1: General Guidance. ISO 4664–1:2011, 2011.

26. ASTM E83: Standard Practice for Verification and Classification of Extensometer Systems. ASTM International, West Conshohocken, PA, 2010.

27. Vishay Precision Group: Strain Gage Selection: Criteria, Procedures, Recommendations. Technical Note TN−505−4, Document No. 11055, 2014.

28. Datta, S., et al.: Effect of Thermal History and Gallium Content on Magneto-Mechanical Properties of Iron Gallium Alloys. Mater. Sci. Eng., A, vols. 435–436, 2006, pp. 221–227.

29. Vishay Precision Group: Optimizing Strain Gage Excitation Levels. Technical Note TN−502, Document No. 11052, 2010.

30. Vishay Precision Group: Shunt Calibration of Strain Gage Instrumentation. Technical Note TN−514, Document No. 11064, 2013.

31. Vishay Precision Group: Strain Gage Thermal Output and Gage Factor Variation with Temperature. Technical Note TN−504−1, Document No. 11054, 2014.

32. Hines, F.F.: Effect of Mounting Surface Curvature on the Temperature Coefficient of Bonded Resistance Strain Gages. Proceedings, Western Regional Strain Gage Committee, The Society for Experimental Mechanics, Bethel, 1960, pp. 39–44.

33. Maplesoft: High-Performance Software Tools for Engineering, Science, and Mathematics. Waterloo, Ontario, 2015. http://www.maplesoft.com/products/Maple/ Accessed June 1, 2015.

34. Smith, Ralph C., et al.: A Homogenized Energy Framework for Ferromagnetic Hysteresis. IEEE Trans. Magn., vol. 42, no. 7, 2006, pp. 1747−1769.

35. Wun-Fogle, M.; Restorff, J.B.; and Clark, A.E.: Soft and Hard Elastic Moduli of Galfenol Transduction Elements. J. Appl. Phys., vol. 105, 07A923, 2009.

36. Atulasimha, Jayasimha; Flatau, Alison B.; and Kellogg, Rick A.: Sensing Behavior of Varied Stoichiometry Single Crystal Fe-Ga. J. Intell. Mater. Syst. Struct., vol. 17, no. 2, 2006, pp. 97–105.

37. Vishay Precision Group: Noise Control in Strain Gage Measurements. Technical Note TN−501−2, Document No. 11051, 2013.

38. Restorff, J.B.; Wun-Fogle, M.; and Summers, Eric: Hysteresis, $d*_{33}$ and d_{33} of $Fe_{81.6}Ga_{18.4}$ Textured Polycrystals. J. Appl. Phys., vol. 109, 07A922, 2011.

39. Datta, S., et al.: Stress and Magnetic Field-Dependent Young's Modulus in Single Crystal Iron-Gallium Alloys. J. Magn. Magn. Mater., vol. 322, no. 15, 2010, pp. 2135–2144.

40. Evans, P.G.; and Dapino, M.J.: Efficient Magnetic Hysteresis Model for Field and Stress Application in Magnetostrictive Galfenol. J. Appl. Phys., vol. 107, 063906, 2010.

41. Summers, Eric M., et al.: Magnetic and Mechanical Properties of Polycrystalline Galfenol. Proc. SPIE 5387, vol. 448, 2004.

42. Evans, Phillip G.; and Dapino, Marcelo, J.: Measurement and Modeling of Magnetic Hysteresis Under Field and Stress Application in Iron-Gallium Alloys. J. Magn. Magn. Mater., vol. 330, 2013, pp. 37–48.

43. Yoo, Jin-Hyeong, et al.: An Examination of Galfenol Mechanical–Magnetic Coupling Coefficients. Smart Mater. Struct., vol. 20, no. 7, 2011.

44. Atulasimha, Jayasimha; and Flatau, Alison B.: Experimental Actuation and Sensing Behavior of Single-Crystal Iron-Gallium Alloys. J. Intell. Mater. Syst. Struct., vol. 19, no. 12, 2008, pp. 1371–1381.

45. Kellogg, Rick; and Flatau, Alison: Experimental Investigation of Terfenol-D's Elastic Modulus. J. Intell. Mater. Syst. Struct., vol. 19, no. 5, 2008, pp. 583–595.